Macroscopic Manifestations and Coherent Manipulations of Quantum Mesoscopic Systems

A Thesis

Submitted to the Faculty

in partial fulfillment of the requirements for the

degree of

Doctor of Philosophy

In

Physics and Astronomy

by

Joel Stettenheim

Dartmouth College

Hanover, NH

August, 2012

Examining Committee:

Chairman: _____
Alexander J. Rimberg

Member: _____
Lorenza Viola

Member: _____
Miles P. Blencowe

Member: _____
Robert H. Blick

_____
Brian W. Pogue, PhD
Dean of Graduate Studies

Abstract

Mesoscopic physics is a fascinating realm in which classical descriptions are usefully applied but wherein quantum behavior is strongly manifest. As such, it is an ideal arena for exploring the interplay between the classical and quantum worlds and the ways in which we can effectively control and coherently manipulate quantum systems with macroscopic inputs. Focusing on coupling between macroscopic and quantum systems, the first area of research presented in this thesis is our discovery and exploration of a naturally occurring feedback loop in which the mechanical motion of a macroscopic semiconductor crystal is controlled by the statistical fluctuations of tunneling electrons [1]. The second area of research presented in this thesis is a description of our implementation of a system for the coherent manipulation of electronic spins using electron spin resonance.

Consisting of a one-dimensional conduction channel and a tunable tunnel barrier, (quantum point contacts) QPCs are canonical quantum systems that display a rich array of physics [2–6]. In our GaAs system through piezoelectric coupling, the QPC current I probes the deformation of the host crystal and generates a naturally occurring feedback loop. Such systems with coupled mechanical and optical or electrical degrees of freedom [7], [8] have fascinating dynamics that, through macroscopic manifestations of quantum behavior [9], provide new insights into the transition between the classical and quantum worlds. The feedback, which is naturally associated with backaction, has been predicted to have significant consequences for the noise of a detector coupled to a mechanical oscillator [10], [11]. In our case the source of the backaction is shot noise, an intrinsic

noise source due to the stochastic partitioning of discrete charge flow by the QPC tunnel barrier.

While ESR is conceptually relatively straight-forward, it is technically challenging to generate an ac magnetic field B_{ac} large enough to manipulate spins fast enough to perform meaningful quantum computation operations. In addition it is important to minimize the ac electric field E_{ac} which can cause sample heating and induce unwanted photon assisted transitions. As described in Chapter 3 in our ESR system, we address these issues by create a standing wave in a stripline and place the sample at a peak in B_{ac} and a node in E_{ac}.

Acknowledgements

I am deeply indebted to my family, advisors and colleagues for their support, guidance, and inspiration in the completion of my PhD. First, I would like to thank my wife, Signe Taylor, and children, Lyla and Soren, for the many hours they tolerated my absence and dealt with a highly variable schedule that often involved late night sessions in the lab or in the bowels of the medical school fabricating devices with the SEM. In addition, I appreciate Signe's strong encouragement to pursue my passion for the rigors and fun of experimental physics in following a highly unusual career path from patent lawyer to graduate student. It has been a fantastic journey that I have enjoyed immensely. The subject matter, at times strange and mysterious, has been wonderfully stimulating and the hands-on experimental work has been immensely satisfying. I also extend special thanks to my parents, Peter and Sandy Stettenheim, who by example and advice, taught me to follow my instincts and to take advantage of all the opportunities that life has to offer.

I have been extremely fortunate in having Alex Rimberg as my advisor, guiding my development as an experimental physicist. He has a very keen theoretical command of the subject matter and an impressive ability to work through challenging experimental problems. It has been highly instructive to have participated in this process with him. Over the past several years, I have developed a belief that one's ultimate success as an experimental physicists derives from an interest and an enjoyment in solving problems on a day-to-day basis. In this context, Alex has the remarkable ability to provide appropriate

guidance when a student is in need, but also to provide freedom and autonomy when a student is making good independent progress.

I am also appreciative of the excellent guidance and input that I have received from the other members of my thesis committee, Prof. Miles Blencowe, Prof. Lorenza Viola, and, most recently, Prof. Robert Blick. Prof. Blencowe has been an invaluable collaborator, not only generating excellent theoretical work, but also providing wise advice into how we could best conceptualize and frame our backaction research so as to make it mostly widely accessible to the physics community. Prof. Viola has provided wonderful support and insightful questions. I have also benefitted tremendously from her exceptional instruction, including her excellent course on quantum computation. Having come highly recommended by Alex, I very much appreciate Prof. Blick's willingness in taking time to help me complete the final stage in my doctoral journey.

Last, but my no means least, are the debts that I owe to my numerous lab mates. When I joined the Rimberg Group, Madhu Thalakulum, Zhongqing Ji, and Tim Gilheart were already well established. Each willing offered his time in teaching me essential research skills. Under Madhu I began my study in the art of measurement. I still remember his description of efforts to remove noise as like a process of cleansings one's experiment of sins. Zhongqing had the remarkable ability to disassemble the most complicated laboratory equipment, diagnose the fault, and then reassemble it in working order. It was enjoyable to have witnessed and to have been involved in some of these efforts. He taught me that things often break for obvious reasons that can be identified and corrected with careful common sense exploration. From Tim, I learned a wealth of relevant laboratory chemistry as well as practical mechanical and electrical aspects of our

work. I also enjoyed working with Weiwei Xue, Feng Pan and Mustafa Bal. I appreciated Weiwei's interest in solving problems and his openness to input from any lab member. Fen taught me the value of developing efficient techniques that increase the likelihood of experimental success. Mustafa was my compatriot on the ESR project, and as we diligently worked through and resolved a host of experimental challenges, we developed a strong solidarity and an enjoyable working relationship. I have also very much enjoyed working with Mingyun Yuan, Fei Chen, and Julian Li. The new results that these individuals are generating are impressive and exciting and bode very well for the future success of the group. As the group's newest members, I look forward to getting to know better Zhen Yang and Chunyang Tang.

Table of Contents

List of Figures

1 Overview of Quantum Point Contacts and Quantum Dots

1.1 Introduction

Two of the most fundamental quantum nanostructures are quantum point contacts (QPCs) and quantum dots (QDs). This chapter begins with a review of the basic theory and properties of QPCs and quantum dots including a discussion of fundamental parameters, GaAs/AlGaAs two-dimensional electron gases (2DEG) – the system in which these devices are often formed, one dimensional transport, and some characteristics of single and double quantum dots (DQDs). As both QPCs and quantum dots are well suited for use as fast ultra-sensitive charge detectors, they have found wide scale application as measurement devices in numerous quantum information processing systems. The chapter concludes with a discussion of the radio frequency application of these devices, including the low dissipation operation of a superconducting aluminum metallic island quantum dot, referred to as a radio frequency superconducting single electron transistor (RF-SSET).

1.2 Fundamental Parameters

Ohm's law $I = GV$ is a macroscopic classical description of electronic transport in conducting media. For individual electron quantum effects to be observed in a device, its dimensions must be smaller than or comparable to one or more of three important

characteristic lengths: the Fermi wavelength λ_f, the mean free path L_m, and the phase coherence length L_φ [12–16].

The Femi wavelength is the de Broglie wavelength of an electron with kinetic energy E_f and is given in two dimensions by $\lambda_f = 2\pi/k_f = (2\pi/n_s)^{1/2}$ where k_f is the Fermi wavevector and n_s is the electron density. The mean free path is the length between scattering events for an electron, and is given by $L_m = v_f \tau$ where v_f is the Fermi velocity and τ is the scattering time. The phase coherence length L_φ is the distance over which an electron retains a definite phase during transport and is related to the coupling of an electron to the environment [15],[16].

A submicron device patterned on the surface of a GaAs/AlGaAs heterostructure is an ideal system for studying quantum phenomena. The properties of the high quality two-dimensional electron gas (2DEG) that can be formed at the heterostructure interface are why the system has been so widely utilized. A typical density value of $n_s = 2 \times 10^{11}$ cm^{-2} yields a Fermi wavelength of $\lambda_f = 50$ nm which means that individual electrons can be trapped and probed in submicron devices. The high mobility values achieved by crystal growers are on the order of $\mu = |\boldsymbol{E}|/|\boldsymbol{v_f}| = 10^6$ cm^2/Vs, where $\boldsymbol{E}$ is the electric field. This mobility value corresponds to a scattering time of $\tau = m^* \mu/e = 40$ ps which yields a mean free path $L_m = 10$ μm. This means that transport in micron or submicron devices is ballistic. Lastly, the phase coherence length L_φ increases with decreasing temperature and at temperatures below 100mk can stretch to 10's of microns allowing coherent processes such as interference effects to be observed [16].

By depleting the 2DEG with negative voltages applied to metallic surface gates, one-dimensional (1D) and zero-dimensional (0D) systems can be created. Quantum point

contacts (QPCs) are used to form constrictions in the 2DEG and when properly designed yield clear signatures of 1D transport. Multiple QPC constrictions can be combined to form OD dimensional pools of electrons. Known as artificial atoms or quantum dots (QDs) these systems display a rich array of physics and have been extensively studied [18], [19].

1.3 GaAs/AlGaAs Two-dimensional Electron Gas

The high mobility μ and long mean free path L_m discussed above are largely the result of few scattering defects in the region of the 2DEG. Grown with atomic layer precision using molecular-beam-epitaxy (MBE), the close lattice spacing of GaAs and AlGaAs makes an almost perfect crystalline interface possible. Modulation doping in which the carrier dopants are spaced from the 2DEG interface is an additional important factor in achieving a clean low scattering interface [20].

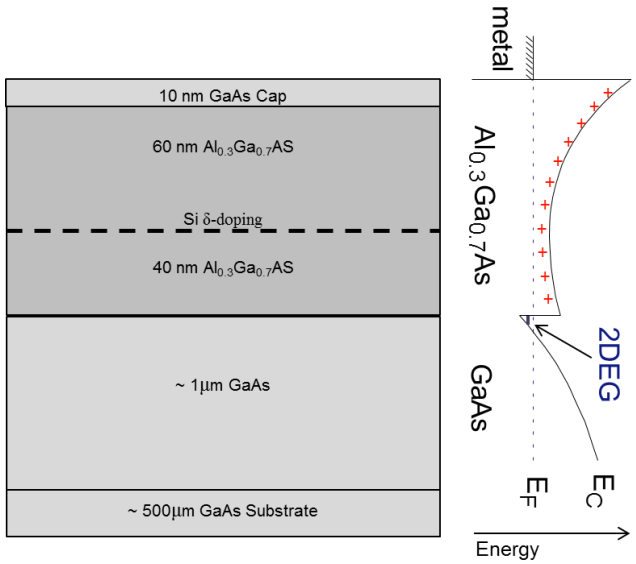

Figure 1.1 A representative GaAs/AlGaAs heterostructure profile and corresponding conduction band edge. The 2DEG forms at the GaAs/AlGaAs interface where a triangular potential drops below the Fermi level. (Figure adapted from reference [21]).

Figure 1.1 shows a typical wafer profile with the corresponding conduction band energy diagram. The III-V GaAs/AlGaAs heterostructure architecture starts with a bulk GaAs substrate and then a very high quality block of GaAs of approximately a micron in thickness. This is followed by 40 nm of AlGaAs, a thin Si dopant layer, 60 nm more of AlGaAs, and finally a 10 nm cap of GaAs to prevent oxidation. Frequently termed a δ-dopant layer, the Si layer has typical densities of 4×10^{12} cm^{-2}. In addition to removing the dopant defects from the interface, placing the dopants 10's of nanometers from the 2DEG helps smooth potential fluctuation introduced by the random nature of the lateral distribution of dopant [21].

The formation of the 2DEG is a result of the conduction band offset and an initial mismatch in the bulk chemical potentials of the GaAs and AlGaAs layers. At thermal equilibrium, electrons from the Si and AlGaAs layers fall into the GaAs substrate layer. The resulting space charge bends the conduction band energy forming a triangular potential at the heterostructure interface [16], [20]. At typical electron densities and temperatures, only the first subband in the growth direction is occupied. This confines the electrons to ~ 10 nm of the interface. The second subband is separated from the first by ~ 150 meV [16]. This energy is larger than the typical Fermi energy (7 meV), the ambient temperature (T < 1K = 86 μeV), and typical source-drain biases (V_{SD} < 1 meV).

1.4 Quantum Point Contacts and 1D Quantum Transport

A remarkable fact regarding QPCs is that while the constriction that they form may only be a few Fermi wavelengths long, they function as a 1D quantum conduction channel between the continuum of states in the open 2DEG [12], [22]. A principle

signature of 1D quantum transport is quantization in the conductance G with plateaus corresponding to integer number of conduction channels.

A simple model for the energy of an electron in a QPC is given by the Hamiltonian

$$H = \frac{p_x^2}{2m^*} + \frac{p_y^2}{2m^*} + eV(y) \qquad 1.1$$

where $V(y)$ is the transverse confining potential and $m^* = 0.067\ m_e$ is the effective mass of an electron in GaAs. The effective mass m^* accounts for the periodic potential of the lattice. Following the approaches in Berggren [23], Laux [24], and Cronenwett [16] and taking the potential to be parabolic $V(y) = \frac{1}{2}\, m^* \omega_o^2 y^2$, the solution to Schrodinger's equation yields a dispersion relation that includes a harmonic oscillator term for the quantized y energy values

$$E_n = (n - \tfrac{1}{2})\hbar\omega_o + \frac{\hbar^2 k_x^2}{2m^*}, \quad (n = 1, 2, 3...)\,. \qquad 1.2$$

These energy values are plotted in Figure 1.2. Each parabolic subband corresponds to one of the transverse modes and includes a continuum of k_x plane wave states. The separation between the subbands is given by $\hbar\omega_o \sim$ 1-5 meV [24].

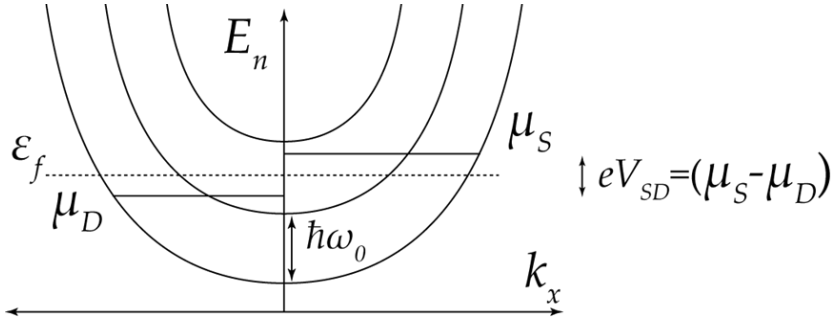

Figure 1.2 Energy dispersion curves for the first three 1D conduction channels (subbands) of a QPC. The subbands are separated in energy by $\hbar\omega_o$. An applied bias between the source and drain μ_S- μ_D results in uncompensated right moving electron states which constitute a net current.

Interestingly the signatures of 1D transport for a QPC can be calculated independent of this dispersion relation and is general to transport in all 1D quantum systems. The key to this remarkable fact is that in 1D the group velocity $v(E)=1/\hbar\ dE/dk$ is a scalar and its energy dependence cancels that of the spin degenerate density of states $g(E) = 2/\pi\ (dE/dk)^{-1}$. Intuition into this cancellation can be had by recognizing that the velocity $v(E)$ has an increasing energy dependence while for the density of states $g(E)$ the dependence is decreasing.

In calculating the current, only the bias window $eV_{SD} = (\mu_S - \mu_D)$ between the source μ_S and drain μ_D chemical potentials needs to be considered. For energies less than μ_D, the net current is zero as each k^+ state is cancelled by a corresponding k^- state. In calculating the current, each subband is indexed by n with its own group velocity $v_n(E)$ and density of states $g_n(E)$ [12], [16], [22]

$$I = \sum_{n=1}^{N} e\int_{\mu_D}^{\mu_S} v_n(E)g_n(E)T_n(E)dE = \sum_{n=1}^{N} e\int_{\mu_D}^{\mu_S} \frac{1}{\hbar}\left(\frac{dE}{dk}\right)\frac{1}{2}\frac{2}{\pi}\left(\frac{dE}{dk}\right)^{-1} T_n(E)dE$$
$$= \frac{2e}{h}\left(\mu_S - \mu_D\right)\sum_{n=1}^{N} T_n(E_f). \qquad (1.3)$$

The factor $T_n(E)$ is the transmission probability for the n^{th} subband and for small source-drain biases V_{SD} can be approximated with its Fermi energy value $T_n(E_f)$. The factor of ½ accounts for the discrepancy between the density of states $g_n(E)$ which includes positive and negative values of k and the current integral which is based only on the non-cancelled k^+ states [25]. Calculating the conductance $G = I/V_{SD}$ yields the famous 2-terminal Landauer formula which for ballistic transport $\sum T_n(E_f) = N$ reads

$$G = \frac{2e^2}{h} N. \qquad 1.4$$

Given its remarkable generality and dependence only on fundamental constants, the value G_o is called the *quantum conductance* and has a value of $G_o \approx 2e^2/h = 77.4\ \mu$S which is the inverse of the *quantum resistance* $R_Q = 1/G_o \approx 12.9$ kΩ. This is the inherent conductance (or resistance) associated with a 1D channel.

The steps in conductance of a QPC can be observed when the gate voltage V_g forming the constriction is varied. By analogy, the QPC functions like an electron waveguide where each plateau corresponds to an integer number of quantum conduction channels. As V_g is ramped to zero, successively higher transverse channels become occupied as their energies are brought below the chemical potential. As seen in Fig. 1.3 the plateaus occur at integral numbers of G_o.7

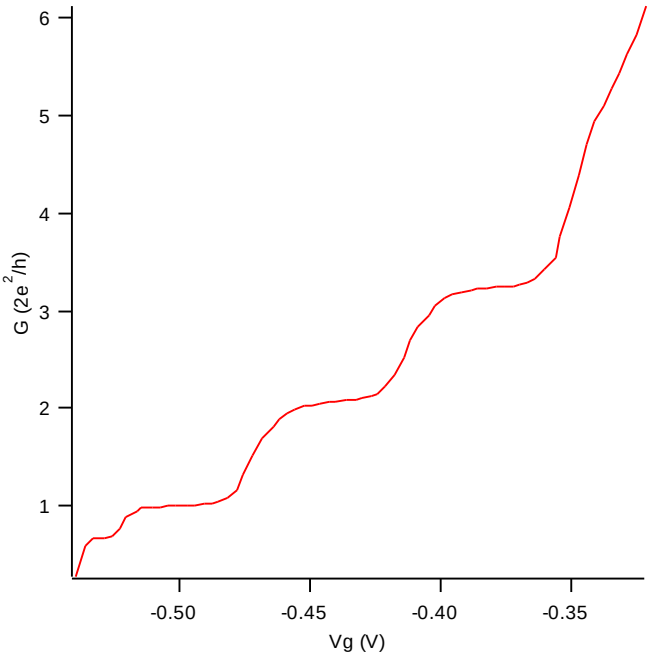

Figure 1.3 Data from a DQD sample showing quantized conductance plateaus for the 1D constriction of a QPC as a function of the gate voltage V_g. The first half plateau corresponds to the 0.7 structure whose origin is an area of active research.

1.5 Single Quantum Dots and Coulomb Blockade

In semiconductor implementations, a quantum dot is an isolated pool of electrons separated from the continuum states of the 2DEG by QPC tunnel barriers. In a closed dot, the tunnel barriers are sufficiently opaque that confined electrons fill zero-dimensional states analogous to those of an atom, and the number of electrons N on the dot is well defined [18], [26]. The energy required to add an electron to the system includes not only the single particle energy E_N of an electron in the dot but also the charging energy E_C associated with the electrostatic repulsion of the confined electrons. Due to a required degeneracy in the thermodynamic potential Ω, Van Houton, Beenakker, and Staring,show [27] that with a small bias across a dot, conduction occurs whenever the difference in free energy of the system with N and N-*1*electrons is equal to the Fermi

energy E_f of electrons in the leads. That is, $F(N) - F(N\text{-}1) = E_f$. As $\mu(N) \equiv F(N) - F(N\text{-}1)$, the question of transport through a QD is therefore shown to map onto determining the free energy $F(N)$ of the system.

An analysis of the free energy $F(N)$ of a QD is traditionally done in the context of the constant interaction (CI) model. The CI model makes two primary assumptions. First, the Coulomb interactions between electrons on a dot can be described by a single capacitance C that is the sum of individual capacitances. That is, $C = C_s + C_d + C_g$ where C_s, C_d, and C_g are, respectively, the capacitance between the dot and the source, drain, and gates. Second, the discrete energy spectrum for the dot is not affected by the number of electrons in the dot.

As shown in Figure 1.4, the dot is modeled as an island capacitively coupled a gate with voltage V_g. The tunnel junctions of the source and drain are represented as leaky capacitors where the capacitances C_s, C_d are each in parallel with a corresponding resistor R_s, R_d. As in the case of the QPC discussion above, the difference in chemical potential between the source and drain corresponds to the applied bias across the dot, $eV_{SD} = (\mu_S - \mu_D)$.

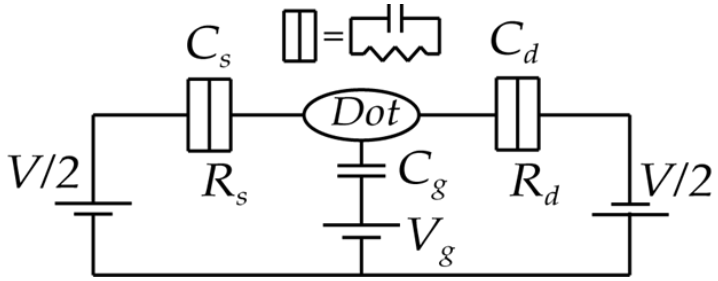

Figure 1.4 Schematic model of a QD capacitively coupled to a gate voltage V_g. The tunnel junctions to the source and drain leads are represented as leaky capacitors.

Under the CI model, the free energy $F(N)$ of the dot with N excess electrons is

$$F(N) = \frac{[eN - C_g V_g]^2}{2C} + \sum_{n=1}^{N} E_n(B) \qquad 1.5$$

where the first term is due to the coulombic interactions between confined charges and the second term is the sum over the energies of the individual electronic states E_n [26], [28], [29]. The coulombic interaction term includes a discrete component eN and a continuous component $C_g V_g$. The discrete component $N = N'-N_0$ accounts for trapped excess conduction electrons where N' is the total number of electrons on the dot and N_0 is the number of electrons on the dot with zero gate voltage. The charge N_0 balances the background positive donor charge so that at $V_g = 0$ the system is neutral. The continuous term $C_g V_g$ accounts for the polarization charge of the dot induced by the gate voltage V_g. For any value of V_g, the number of excess electrons N on the dot is the value which minimizes the free energy $F(N)$ expression 1.5. This means that the number of excess electrons N can be varied externally by adjusting the gate voltage V_g.

Transport through the dot is most easily understood from the perspective of the chemical potential of the dot μ_d which with the definition above yields the expression

$$\mu_d(N) \equiv F(N) - F(N-1) = (N - 1/2)E_C - e(C_g / C)V_g + E_{N'} \qquad 1.6$$

where $E_C = e^2/C$ is the charging energy of the dot. The spacing between the discrete chemical potential levels is given by

$$E_{add} = \Delta\mu_d = \mu_d(N+1) - \mu_d(N) = E_C + \Delta E \qquad 1.7$$

This difference in chemical potential includes the charging energy E_C and the energy difference ΔE (if any) associated with the N +1 electron being in a higher energy shell than the N electron [29],[26]. For submicron dots, the charging energies E_C are in the range of ½ to a few meV's [26], [30]. As shown in Figure 1.5(a), this charging energy E_C creates a barrier to transport referred to as Coulomb blockade. If the energy of electrons in the source μ_S is not greater than the energy required to add another electron to the dot μ_d or the energy of the last filled dot state μ_d is not greater than the energy required to add an electron to the drain μ_D then current in blocked and the charge state of the dot is fixed.

In general Coulomb blockade can be lifted by two primary mechanisms both of which satisfy the general condition that the dot's chemical potential μ_d falls in the bias window, $\mu_S > \mu_d > \mu_D$. First, the gate voltage can be tuned (Figure 1.5(b)) to draw μ_d between μ_S and μ_D. When current flows, individual electrons sequentially tunnel on and off the dot, and in this manner, a current consisting of individual electrons flows through the dot. A further mechanism for lifting Coulomb blockage is that the bias window, can be increased to meet the condition $\mu_S > \mu_d > \mu_D$. If $\mu_S - \mu_D$ is large enough (Figure 1.5(c)), additional states on the dot are available. This results in an increase in current. If the bias window is increased still further, then both the N and the $N + 1$ state of the dot are energetically accessible (Figure 1.5(d)) [26], [29].

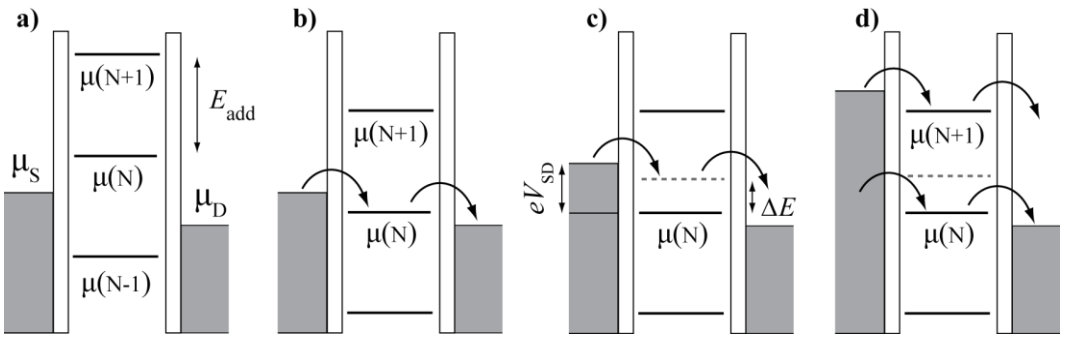

Figure 1.5 (a) The energetic cost of adding an N^{th} electron to the dot exceeds that available to the source electrons. Therefore, due to Coulomb blockage, the number of electrons on the dot remains fixed at N-1 and no current flows. (b) When $\mu_d(N)$ falls between μ_S and μ_D, single electron conduction through the dot occurs. (c) The source-drain window (i.e., $\mu_S - \mu_D$) can be increased so that transport through the dot can be via an excited dot state. With two transport channels available to an electron, the current increases relative to (b). (d) The source-drain window can be increased further so that energetically both an N and an N+1 electron can be on the dot at the same time. This corresponds to a still larger current than in (c). (Figure adapted from reference [29].)

A direct demonstration of the discrete nature of the conductance of a QD is achieved by sweeping the gate voltage and observing the peaks in conductance each time the transport condition $F(N) - F(N\text{-}1) = E_f$ is met (Figure 1.6). The conductance peaks are equally spaced in V_g at intervals of $\Delta V_g = e/C_g$. This separation can be calculated from the equivalence of $\mu_d(N,V_g) = \mu_d(N+1,V_g + \Delta V_g)$ [26], [29]. Between these peaks, coulomb blockage exists and the number of excess electrons N on the dot is fixed. The charging energy E_C is computing from ΔV_g by the ratio $\eta = C_g/C \sim 0.1$, $E_C = e\eta\,\Delta V_g = (e^2/C_g)(C_g/C)$. For the dot in Figure 1.6 with a typical value of η, $E_C \approx 2.5$meV corresponding to a dot diameter $d \sim 150$ nm.

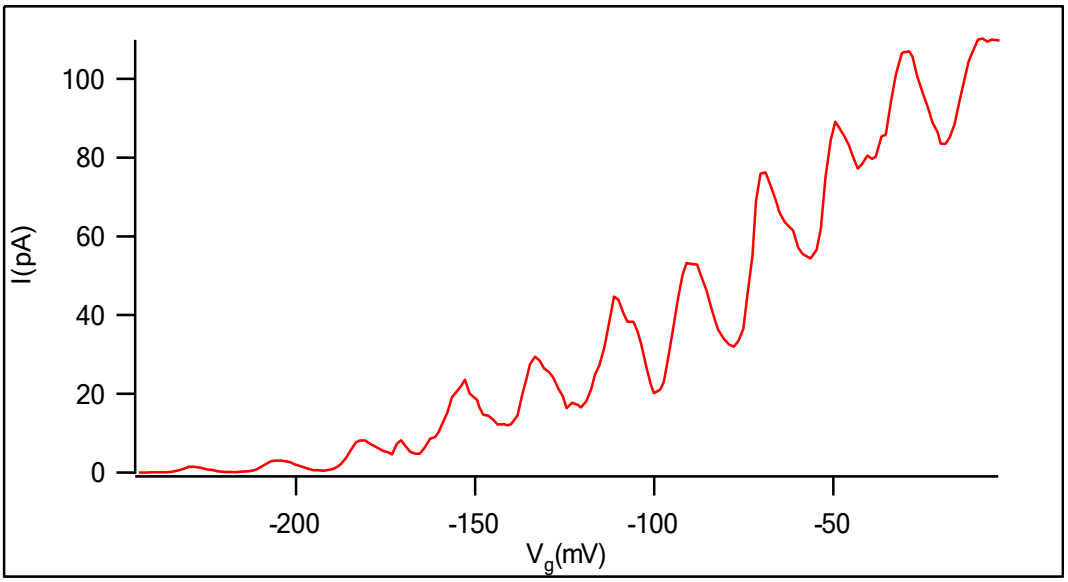

Figure 1.6 Current peaks as a function of gate voltage for a QD. Between the peaks due to Coulomb blockade, the preferred charge state of the dot corresponds to an integer N number of electrons. At the peaks, $\mu_S > \mu_d > \mu_D$ leading to an increase in current as the dot can freely oscillate between the N and N+1 charge states. The separation in the peaks $\Delta V_g \approx 25$mV corresponds to a dot diameter $d \approx 150$nm. The upward slope of the plot is caused by the increasing current associated with the lower tunnel barriers as $V_g \rightarrow 0$.

A further signature of transport in QDs is manifest when the differential conductance (dI/dV_{SD}) is plotted as a function of both the gate V_g and the source-drain voltages V_{SD} (Figure 1.7). The classic signature of Coulomb blockade is a diamond shaped region where conductance is blocked. The expanding black region in the left of Figure 1.7 strongly suggests that the central diamond corresponds to a single electron on the dot. The diamond is tilted due to an asymmetry between the left and right tunnel barriers. The qualitative shape of a coulomb blockade diamond can be understood by noting that: 1) the maximum necessary change in gate voltage between conductance peaks will occur when $V_{SD} \sim 0$, 2) as V_{SD} is increased from zero, there exists an increasing conductance region corresponding to $\mu_S > \mu_d > \mu_D$ (Figure 1.5(c)), and 3) when the source drain bias is greater than the charging energy, i.e. $\mu_S - \mu_D > E_C + \Delta E$, then a current flows

for any value of V_g (Figure 1.5(d)). The color contour lines correspond to changes in conductance associated with a change in the number of available transport channels through the dot [26], [29].

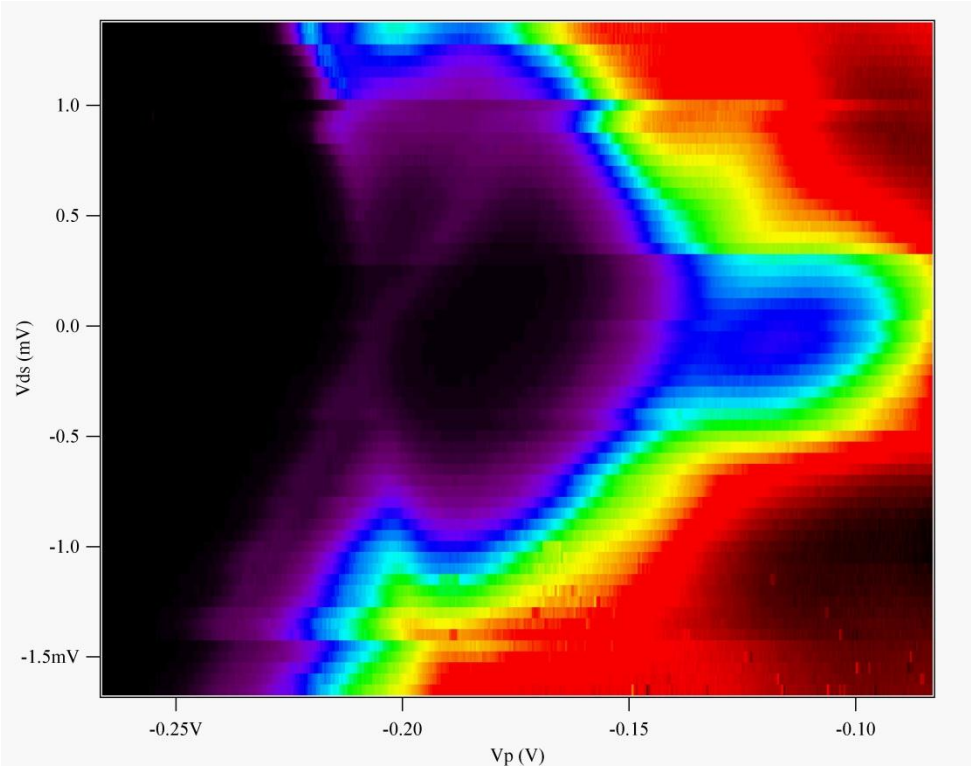

Figure 1.7 A plot of the differential conductance dI/dV_{ds} plotted as a function of the plunger gate (V_g) and source-drain (V_{SD}) voltages. The expanding left region of no conductance strongly suggests that the central diamond corresponds to a single electron on the dot. The color contour lines represent changes in differential conductance that occur when transport channels through excited states in the dot become accessible.

1.6 Double Quantum Dots

A DQD system can be formed by coupling two single QDs. The system is modeled in Figure 1.8 where an important new feature is the interaction between the dots represented by the mutual capacitance C_m and the tunneling resistance R_m.

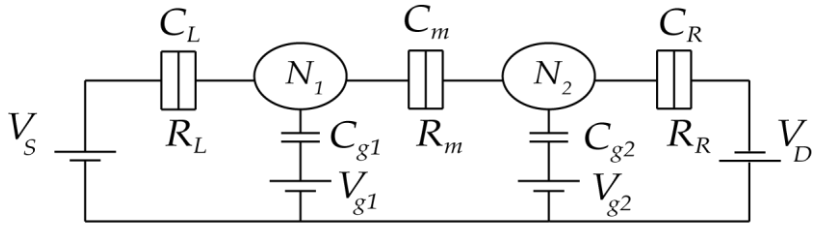

Figure 1.8 A schematic model for two QDs coupled in series. The interaction between the dots is parameterized by a coupling capacitance C_m and a tunneling resistance R_m. (Figure adapted from reference [31])

Transport through the dots can be analyzed classically in the linear regime where the bias voltage $V_{SD} \approx 0$. Following the approach in van der Wiel [31], the chemical potentials for the left μ_1 and right μ_2 dots are

$$\begin{aligned}\mu_1(N_1,N_2) &\equiv U(N_1,N_2) - U(N_1-1,N_2) \\ &= \left(N_1 - \tfrac{1}{2}\right)E_{C1} + N_2 E_{Cm} - \tfrac{1}{|e|}\left(C_{g1}V_{g1}E_{C1} + C_{g2}V_{g2}E_{Cm}\right)\end{aligned} \quad 1.8$$

$$\begin{aligned}\mu_2(N_1,N_2) &\equiv U(N_1,N_2) - U(N_1,N_2-1) \\ &= \left(N_1 - \tfrac{1}{2}\right)E_{C1} + N_2 E_{Cm} - \tfrac{1}{|e|}\left(C_{g1}V_{g1}E_{C1} + C_{g2}V_{g2}E_{Cm}\right)\end{aligned} \quad 1.9$$

where $E_{C1(2)}$ is the charging energy of dot 1(2) and E_{Cm} is the electrostatic coupling energy that accounts for the change in energy of one dot when an electron is added to the other. The charging energies $E_{C1(2)}$ resemble the charging energy of an unpaired dot with a correction factor dependent on the coupling C_m.

$$E_{C1(2)} = \frac{e^2}{C_{1(2)}}\left(\frac{1}{1-\dfrac{C_m^2}{C_1 C_2}}\right) \quad 1.10$$

From the chemical potentials μ_1 and μ_2, a charge stability diagram can be constructed that gives the occupation numbers (N_1,N_2) of the two dots as a function of the gate voltages $V_{g1(2)}$. With $\mu_S = \mu_D \equiv 0$, the occupation numbers (N_1,N_2) are the largest integer values for which μ_1 and $\mu_2 < 0$. Varying the gate voltages $V_{g1(2)}$ produces the honeycomb pattern shown in Figure 1.9. Transport occurs through the dots at electron ● and hole ○ triple points. At these points an energy degeneracy exists between three charge configurations. At electron triple points ●, the dots cycle through the sequence $(N_1, N_2) \rightarrow (N_1+1, N_2) \rightarrow (N_1, N_2+1) \rightarrow (N_1, N_2)$ corresponding to a counter-clockwise rotation. The hole sequence is $(N_1+1, N_2+1) \rightarrow (N_1+1, N_2) \rightarrow (N_1, N_2+1) \rightarrow (N_1+1, N_2+1)$ corresponding to a clockwise rotation. The separation in the triple point energies is given by E_{Cm} which, as mentioned, is the additional energy required to add an electron to dot 1(2) when an extra electron is on dot 2(1). This additional energy allows the transport cycle to proceed $(N_1, N_2+1) \rightarrow (N_1+1, N_2+1)$ as opposed to $(N_1, N_2+1) \rightarrow (N_1, N_2)$.

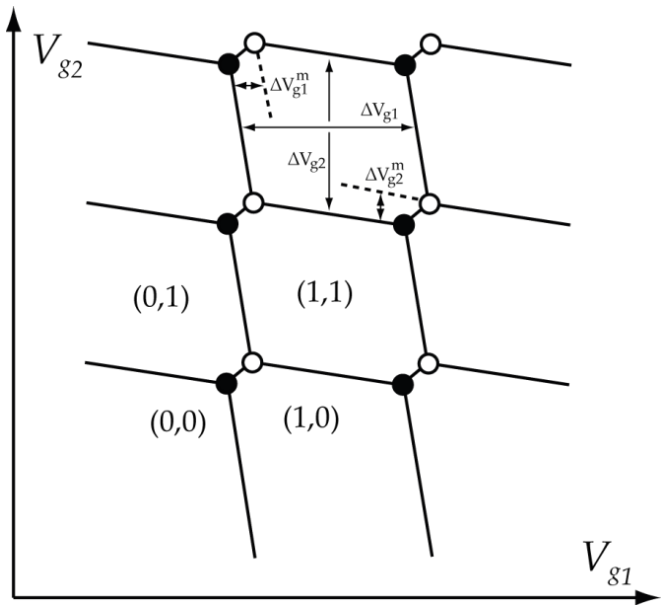

Figure 1.9 A charge stability diagram for a double dot system showing the occupation numbers (N_1,N_2) as a function of the gate voltages V_{g1} and V_{g2}. First order transport through the system occurs around the electron ● and hole ○ triple points. (Figure adapted from reference [31].)

The other dimensions of the stability diagram can be computed from the chemical potential expressions 1.8 and 1.9. The gate voltages required to add an electron to one of dots can be computed from the identities

$$\mu_1(N_1, N_2; V_{g1}, V_{g2}) = \mu_1(N_1 + 1, N_2; V_{g1} + \Delta V_{g1}, V_{g2}) \qquad 1.11$$

$$\mu_2(N_1, N_2; V_{g1}, V_{g2}) = \mu_2(N_1, N_2 + 1; V_{g1}, V_{g2} + \Delta V_{g2}) \qquad 1.12$$

which yield

$$\Delta V_{g1} = \frac{|e|}{C_{g1}}. \qquad 1.13$$

$$\Delta V_{g2} = \frac{|e|}{C_{g2}} \tag{1.14}$$

Interestingly these values are equivalent to the single dot case. The offsets in the honeycomb structure can be calculated from

$$\mu_1(N_1, N_2; V_{g1}, V_{g2}) = \mu_1(N_1, N+1_2; V_{g1} + \Delta V_{g1}^m, V_{g2}). \tag{1.15}$$

$$\mu_2(N_1, N_2; V_{g1}, V_{g2}) = \mu_2(N_1+1, N_2; V_{g1}, V_{g2} + \Delta V_{g2}^m). \tag{1.16}$$

which yield

$$\Delta V_{g1}^m = \frac{|e|C_m}{C_{g1}C_2} = \Delta V_{g1}\frac{C_m}{C_2} \tag{1.17}$$

$$\Delta V_{g2}^m = \frac{|e|C_m}{C_{g2}C_1} = \Delta V_{g2}\frac{C_m}{C_1}. \tag{1.18}$$

These are the voltages that must be applied to the gates $V_{g1(2)}$ to change the occupancy of the other dot 2 (1) by a single electron.

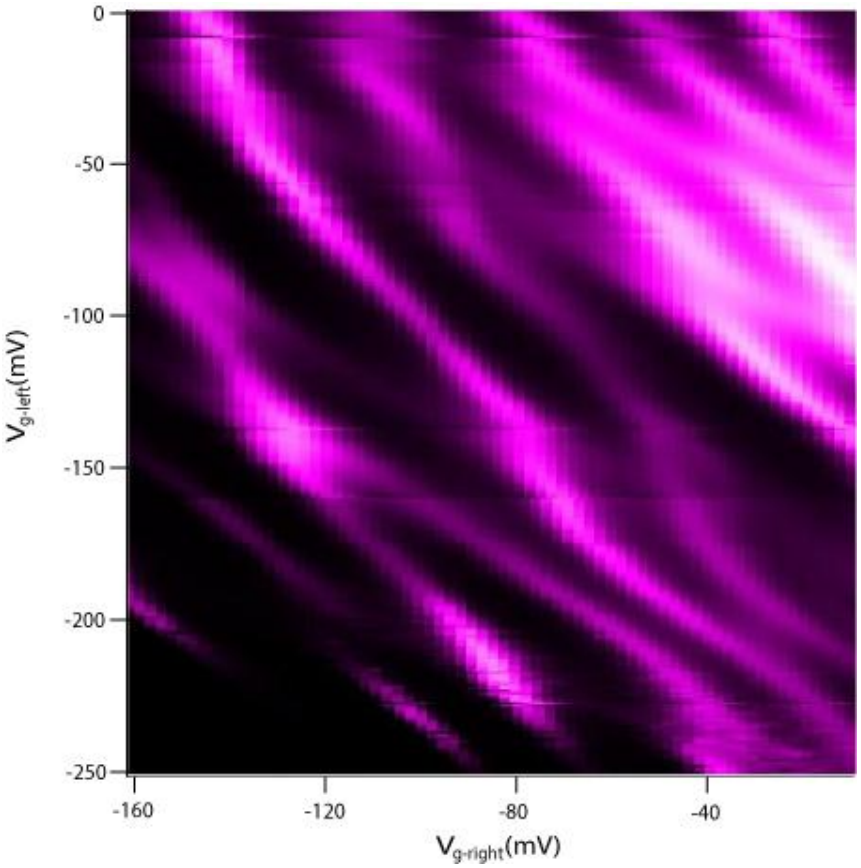

Figure 1.10 A charge stability diagram for a DQD-SSET as recorded by variations in dot current where the horizontal and vertical axes corresponding to variations in plunger gate voltages. The horizontal striations correspond to random background charge changes that manifest themselves as offsets in gate voltages. To compensate for these changes and to make the honeycomb structure apparent, the offsets were removed by aligning stability diagram features, such as the enhanced conductivity along a cell edge.

1.7 Radio-Frequency Quantum Point Contact and Superconducting Single Electron Transistor

When operated at radio-frequencies both QPCs and SETs can function as ultra sensitive extremely fast charge detectors [32–35]. Such measurement times are an important component in numerous solid state implementations of quantum information processing systems. Currently rf-SET charge sensitivities on the order of $\approx 10^{-5}\ e/\sqrt{Hz}$ are routinely achieved, and optimized performance is approaching the theoretical shot noise quantum limit of $1.6 \times 10^{-6}\ e/\sqrt{Hz}$ [36], [37].

The basic principle involved in using a QPC or a SET as an electrometer is that through capacitive coupling the QPC's tunnel barrier or the chemical potential μ_d of the SET island is sensitive to changes, such as charge fluctuations, in the electromagnetic environment. In normal operation, environmental charge fluctuations are recorded as changes in current through the QPC or SET as the barrier or chemical potential shifts. In optimized RF operation, the QPC or SET is embedded in an *LCR* tank circuit and the reflected power is measured. In this set-up, the differential resistance R_d of the QPC or SET, which can be tuned to be a sensitive function of the gate voltage or offset charge Q_0 of the island, forms the resistance of the tank circuit. Significant improvement in the operation of the SET can be achieved by making it superconducting. This minimizes dissipative losses in the system thereby dramatically improving the signal modulation [35], [38], [39].

Figure 1.11 and the following analysis is in terms of an SET and its differential resistance. The analysis applies equally to the differential resistance of a QPC operated in RF mode. Figure 1.11 shows (a) a schematic of a SET embedded in a tank circuit and (b) the corresponding circuit diagram. The impedance of the system looking into the tank circuit is given by [40]

$$Z = i\omega L + \left(i\omega C + 1/R_d \right)^{-1} = \frac{R_d}{1+\omega^2 C^2 R_d^2} + i\,\frac{\omega L - \omega C R_d (1-\omega^2 CL) R_d}{1+\omega^2 C^2 R_d^2}. \qquad 1.19$$

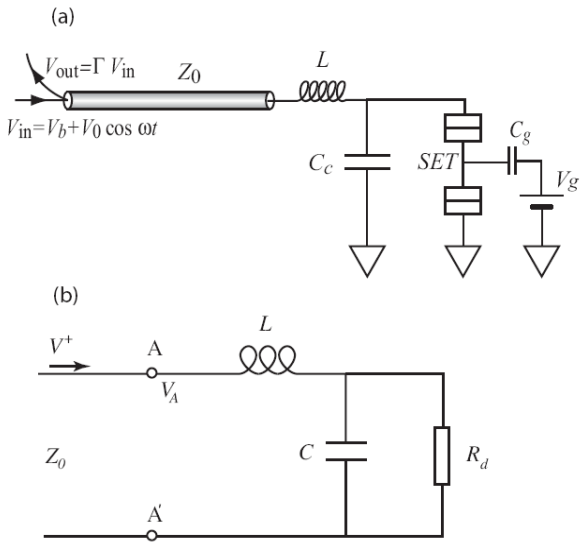

Figure 1.11 (a) A diagram of A SET imbedded in a LCR tank circuit showing the input V_{in} and reflected V_{out} voltage waves. (b) The circuit diagram corresponding to the system in (a).

By definition at resonance, the imaginary terms in Z cancel, minimizing the impedance and maximizing the current. Applying this condition yields

$$\frac{\omega L - \omega C R_d (1-\omega^2 CL) R_d}{1+\omega^2 C^2 R_d^2} = 0 \qquad 1.20$$

from which the resonant frequency can be calculated

$$\omega_0 = \sqrt{\frac{1}{LC}} \sqrt{1 - \frac{L/C}{R_d^2}} \,. \qquad 1.21$$

Plugging this expression for ω_0 back into equation 1.19, yields a remarkably simple result for the impedance of the tank circuit at resonance:

$$Z = \frac{L}{CR_d}. \qquad 1.22$$

The reflection coefficient Γ is defined in terms of the ratio of the incoming V_{in} and reflected V_{out} voltage waves and can be calculated as

$$\Gamma \equiv \frac{V_{out}}{V_{in}} = \frac{Z - Z_0}{Z + Z_0} = -1 + \frac{2Z}{Z + Z_0} \qquad 1.23$$

where $Z_0 = 50\ \Omega$ is the characteristic impedance of the RF coaxial transmission line. Plugging Eq. 1.22 into Eq. 1.23, yields an expression for Γ with the dependence on the differential resistance R_d of the SET made explicit

$$\Gamma = -1 + \frac{2}{1 + Q_0^2 \frac{Z_0}{R_d}} Q_0^2 \frac{Z_0}{R_d} \qquad 1.24$$

where $Q_0 \equiv \sqrt{\frac{L}{C}} \frac{1}{Z_0}$ is the unloaded quality factor. When $R_d = Z_0/Q_0^2$, perfect matching exists and $\Gamma = 0$. For $R_d \rightarrow \infty$, $\Gamma \rightarrow$ -1 corresponding to the expected total reflection from a circuit with an infinite input impedance. The unloaded quality factor is so defined as it determines two important parameters of the circuit: the RF signal applied to the SET $V_{SET} = 2QV_{in}$ and the resonance bandwidth $B = f_0/Q$ [40].

Figure 1.12 in combination with Eg. 1.24 shows the essential features of the RF operation of a SET. Figure 1.12(a) shows the *I*-*V* curves of a SET in (red) and outside

(blue) of coulomb blockade where the shift between these curves can be a function of a gate voltage V_g or changes in the charge state of a device capacitively coupled to the SET.

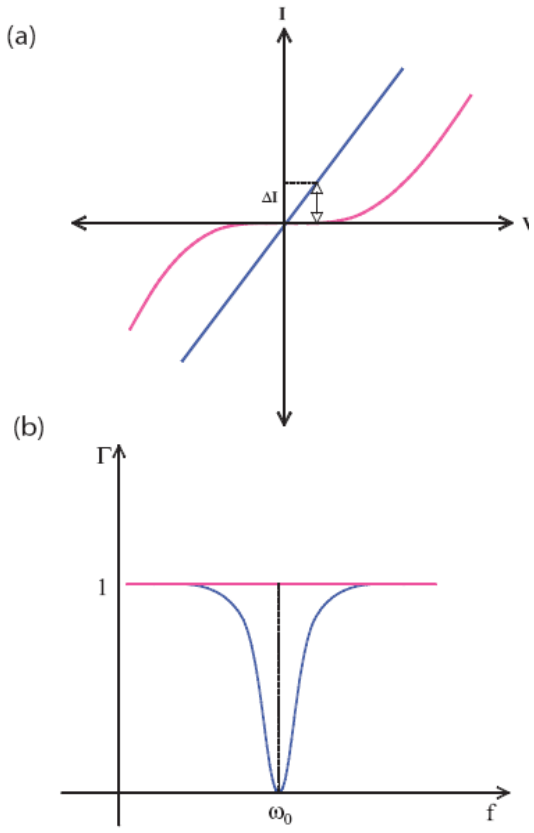

Figure 1.12 (a) An illustrative drawing of the *I-V* curve for a SET in (red) and outside of Coulomb blockade. (b) An illustrative drawing of the reflected power of an SET embedded in an LCR tank circuit when the SET is in (red) and outside (blue) of Coulomb blockade. (Figure from M. Thalakulam Thesis [41].)

The inverse of the slopes of the *I-V* curves is the differential resistance R_d. As shown by Eq. 1.24 and Figure 1.12 when the SET is in coulomb blockade (red line) and biased near $V_{SD} \approx 0$, the differential resistance R_d is infinite, and, as expected, Γ = -1 corresponding to total reflected power. When the SET is outside of Coulomb blockade (blue line) and

perfect impedance matching exists (given a particular combination of R_d, L, and C), then $\Gamma = 0$ and all the power is absorbed by the system. Changes in the values of the reflection coefficient Γ corresponding to charge fluctuations modulate the amplitude of the reflected signal thereby encoding charge detection information.

For real systems with unavoidable additional dissipative elements and in which perfect impedance matching is difficult to achieve, $|\Gamma|$ normally fluctuates between values less than 1 and greater than 0. However related work in our lab shows that when significant efforts are made to remove as much dissipation as possible with the introduction of superconducting elements, the real behavior in terms of the modulation of Γ can closely approximates the ideal case [42].

1.8 High Frequency Noise Properties of a Quantum Point Contact

Arising from the quantization of the electronic charge and the stochastic nature of electrons tunneling though a QPC tunnel barrier, shot noise is an intrinsic unavoidable source of fluctuations in any current measurement. The low frequency or dc value is given by [43]

$$S_{II} = 2\frac{e^2}{2\pi\hbar}\int \mathrm{d}E\, T f \left(1 - T f\right) \tag{1.25}$$

where T is the transmission probability and f the Fermi distribution function specifying the probability that an electronic conduction state is filled. When either T or f is small, this reduces to the familiar Schottky result

$$S_{II} = 2e\langle I \rangle. \tag{1.26}$$

When the QPC is driven by an ac bias at a frequency ω_0, the expression for the resulting photon-assisted shot noise (PASN) $S_I(\omega,\omega_0)$ at a frequency ω is given by

$$S_I(\omega,\omega_0)=\frac{4e^2}{h}\sum_n T_n(1-T_n)\sum_{l=-\infty}^{\infty}(\hbar\omega+l\hbar\omega_0)J_l^2(\alpha)\coth\left[\frac{\hbar\omega+l\hbar\omega_0}{2k_BT}\right] \qquad 1.27$$

where $\alpha=\sqrt{2}eV_{\mathrm{rf}}^{\mathrm{QPC}}/\hbar\omega_0$, $V_{\mathrm{rf}}^{\mathrm{QPC}}$ is the rms amplitude of the ac bias voltage across the QPC, and $J_l(x)$ is a Bessel function of the first kind. This expression can be derived from a more general expression for the shot noise given by Pedersen and Büttiker [44] under the assumption that the transmission coefficients T_n are independent of energy and assuming zero dc bias across the QPC. This form is equivalent to that for the zero frequency photon-assisted shot noise at non-zero dc bias V_{dc} given elsewhere [45] with the substitution of $\hbar\omega$ for eV_{dc}. As shown in Figure 1.13, the expression 1.27 for the PASN shot has a step-wise linear frequency dependence.

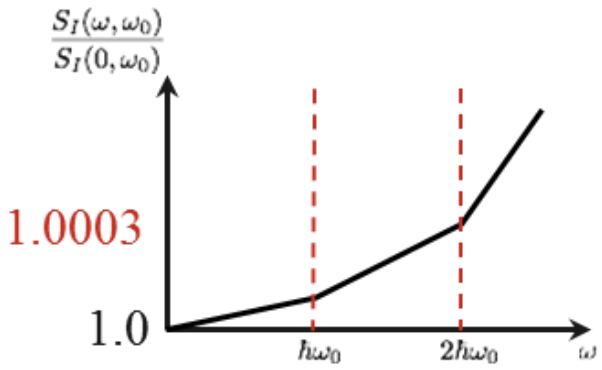

Figure 1.13 Theoretical frequency dependence of photon assisted shot noise (PASN), calculated from the expression 1.27, showing a weak and monotonic relationship, in sharp contrast to the frequency features described in Sections 2.5 and 6.1.

This frequency dependence is relatively weak, corresponding to a variation of only 0.1% over our measurement bandwidth. As discussed below in Section 2.5 and in the appendix

Section 6.1, the expression 1.27 for PASN corresponds numerically to our overall noise measurements. However it does not explain the sharp frequency dependence that we observe.

2 Macroscopic Mechanical Resonance Driven by Shot Noise Backaction of Mesoscopic Quantum Point Contact

2.1 Introduction

This chapter describes the work, with additional details and background information, published in reference [1]. The chapter first discusses our coupled electro-mechanical system in which the backaction of electrons tunnelling through a QPC drive resonant modes of the host crystal through a naturally occurring feedback loop. The second section describes the system's piezoelectric coupling between the mechanical and electrical degrees of freedom. The resulting Hamiltonian and the system's master equation are presented in the third section. As the reflected power spectrum shows unexpected and marked frequency dependence, the power and partition dependence of the data is then presented in the fourth section to demonstrate the signal's origin as shot noise. The fifth section describes the feedback loop that couples the electrical and mechanical degrees of freedom of the system, including a presentation of the experiment used to verify the existence of the feedback loop. The sixth section covers details on the structure of the resonant modes including both the mechanical displacement and the induced electric polarization field. The details of the mathematical methods used for calculating the resonant modes are covered in the Appendix section Resonant Mode Calculation 6.2. In the seventh section, an analysis of the displacement sensitivity of our system is presented. As the feedback loop creates correlations in the tunnelling of electrons, the final eighth section deals with our frequency dependent Fano factor data.

The rf-QPC work described in this chapter was the result of a collaborative effort with essential contributions coming from several members of the lab including Madhu Thalakulum, Feng Pan, Mustafa Bal, Zhongqin Ji, Weiwei Xue as well as Alex Rimberg and myself [1]. The project was initiated by Alex Rimberg. Madhu Thalakulum fabricated the first device, sample A, and took and analysed the first sets of data. These measurements were extremely clean and were used to show the shot noise quantitative power dependence and qualitative partition dependence. Mahdu Thalakulum also performed temperature and magnetic field measurements on sample A. I fabricated five samples, including samples B and C. Fen Pan, Mustafa Bal, Zhongqing Ji and Weiwei Xue fabricated and measured two additional samples. Alex Rimberg and Miles Blencowe, with later help from Latchezar Benatov, developed the theoretical model used to describe the system. Alex Rimberg and I analysed data from all of the sample and co-wrote the published record of the work with input from Miles Blencowe [1]. This effort focused on identifying the source of the shot noise frequency dependence and the development of the piezoelectric feedback loop description and its consequences. This work included analysis of the resonant modes and the transduction coupling factors as well as the macroscopic displacement of the crystal and the associated electron-electron correlations.

2.2 Shot Noise Backaction Feedback Loop Driving Resonant Oscillations

We begin by describing how a QPC naturally couples to a certain three-dimensional vibrational mode of the host crystal and hence can be used to measure displacement. Assume as in Figure 2.1 that each end face of a GaAs crystal containing a

two-dimensional electron gas (2DEG) is displaced laterally a distance *dy*. Such a flexure will cause the center of the crystal to be pinched vertically a distance *dz* on one side and expanded the same amount on the other. The resulting strain $S_{yz} = 2dz / w$, where *w* is the width of the crystal, gives rise through the piezoelectric coupling constant e_{x4} of GaAs to a bulk polarization $P_x = e_{x4} S_{yz}$ that we assume lies along the direction of transport through the QPC.

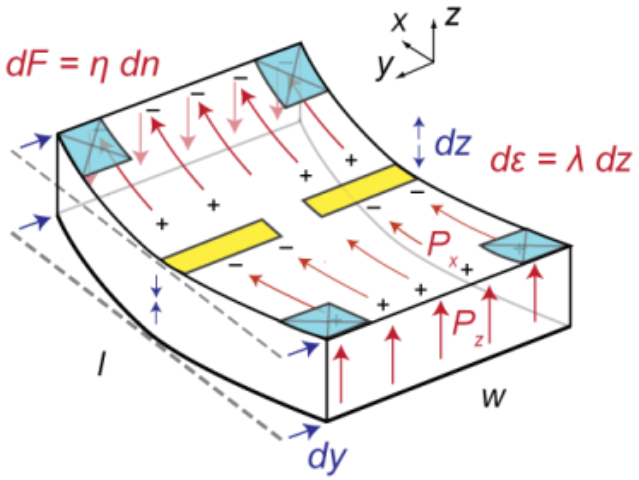

Figure 2.1 A drawing illustrative of the piezoelectric nature of GaAs in which electric polarization fields are associated with deformations of the crystal. A lateral displacement *dy* (blue arrows) with an associated *dz* contraction and expansion in a GaAs crystal generates a shear strain $S_{yz} = 2dz / w$ at the upper surface that causes a corresponding P_z and $P_x = e_{x4} S_{yz}$ polarization. Yellow rectangles are QPC surface gates for which an applied negative voltage depletes conduction electrons in the corresponding 2DEG underneath. Blue squares are ohmic contacts that provide an electrical path between the crystal's surface and the 2DEG.

Electrons in the 2DEG will screen the polarization charge. Under the gates and in the QPC where the 2DEG is depleted, however, a net electric field and corresponding electrochemical potential difference $d\varepsilon$ will exist, resulting in a current *I* between the electron reservoirs, which are labelled *L* (left) and *R* (right), as shown in Figure 2.3. A

simple screening argument, discussed in more detail in Section 2.6, shows that $d\varepsilon = \lambda\, dz$ where λ has units of force. For typical parameters, $\lambda \approx 2.4\,\mathrm{fN}$. The screening of the polarization charge leads to a dipolar accumulation of free charge *dn* in the 2DEG at the location of the ohmic contacts as in Figure 2.1.

Next we describe the naturally occurring backaction induced feedback loop. In particular as the drive $d\varepsilon$ for the current *I* depends on *dz,* the current *I* flowing through the QPC provides information regarding the displacement of the crystal. Unavoidable shot noise arising from the partitioning of electron-hole pairs at the QPC gives rise to a backaction force noise on the oscillator, as shown in Figure 2.2. The associated dipolar charge fluctuations dn in the reservoirs *L* and *R* cause a fluctuating three-dimensional polarization of the GaAs crystal (Section 2.7 and Figure 2.13(a) and Figure **2.14**(a)). This leads, in turn, to a fluctuating backaction force $dF = \eta\, dn$ on the oscillator through piezoelectric coupling (see Section 2.3), where for typical parameters $\eta = 3.7\times10^{14}$ N/C.

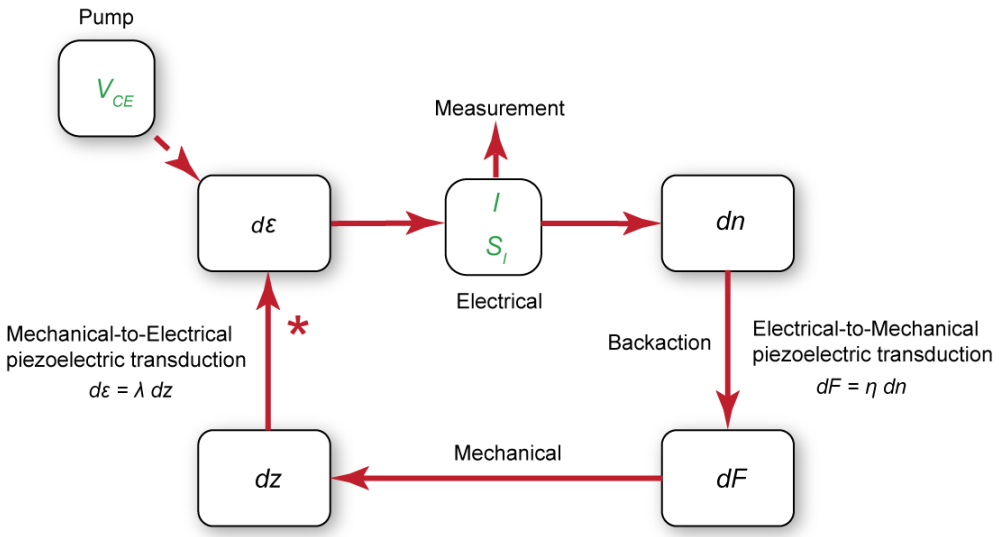

Figure 2.2 A diagram illustrating the naturally occurring feedback loop generated by the backaction of the measurement process. Starting with a displacement *dz* of the crystal, piezoelectric transduction causes an energy difference $d\varepsilon$ between the reservoirs *L* and *R*. The resulting flow of current *I* through the QPC can be used to obtain information regarding *dz*. In this manner the current *I* and its spectral fluctuations S_I constitute measurements of the mechanical system (i.e., displacements of the crystal). Quantum statistical fluctuations in electron tunneling invariably results in shot noise. This causes fluctuations in the accumulated dipolar charge *dn*. These charge fluctuations through piezoelectric transduction in turn lead to a fluctuating force *dF*. Through a straightforward mechanical coupling, the noisy force *dF* imparts a noisy momentum kick to the lattice. The crystal responds preferentially at its resonant frequency with displacement values *dz* having fluctuations peaked at this frequency. These noisy frequency dependent displacements close the feedback loop and introduce a frequency component into the subsequent electrical and mechanical behavior of the system. The energy needed to maintain the current *I* is provided by a bias voltage V_{CE}.

Like a tuning fork struck by an impulsive force, the crystal responds to the backaction force *dF* with mechanical fluctuations *dz* that are strongly peaked at its resonant frequency ω_m. Piezoelectric coupling now leads to fluctuations in the chemical potential $d\varepsilon = \lambda\, dz$ that are also peaked at the mechanical resonance.

In this way, a backaction induced feedback loop [8], [46] coupling the electrical and mechanical degrees of freedom naturally arises as the chemical potential $d\varepsilon$

fluctuations (and the corresponding charge fluctuations *dn*) are now weighed at the ω_m. This transforms the initially white impulsive force $dF = \eta\, dn$ into one that drives the mechanical system preferentially at its own resonant frequency.

2.3 Electrical-Mechanical Piezoelectric Coupling

First we calculate the electrical response of electrons in the 2DEG to mechanical displacements of the host crystal. As illustrated in Figure 2.1 assume a GaAs crystal is subject to a *y*-*z* shear strain $S_{yz} = dz/(w/2)$ at the depth of the 2DEG where *dz* is the *z*-displacement at the edge of a crystal of width *w*. Piezoelectric coupling will give rise to a bulk polarization $P_x = \mu d_{x4} S_{yz}$ where $\mu = 60$ GPa and $d_{x4} = 2.6\times10^{-12}$ C/N are the shear modulus and the piezoelectric stress constant of GaAs, respectively. Within the 2DEG channel at the edges of the crystal a total bound polarization charge per unit length given by $P_x t = (2\mu d_{x4} t/w)\, dz$ will therefore appear; here *t* is the thickness of the 2DEG. The mobile 2DEG electrons will attempt to screen the piezoelectrically induced polarization charge over a Thomas-Fermi screening length $k_{\mathrm{TF}}^{-1} = \sqrt{\varepsilon_r \varepsilon_0 t / e^2 g_{2\mathrm{D}}}$ where ε_r is the relative dielectric constant of GaAs, ε_0 is the permittivity of free space, $g_{2\mathrm{D}}$ is the two-dimensional density of states, k_{TF} is the Thomas-Fermi wave vector, and *e* is the electronic charge. This will result in a dipolar sheet density fluctuation *dn* in the 2DEG on the order of $dn = (2\mu d_{x4} t k_{\mathrm{TF}}/ew)\, dz$ that will appear at each edge of the crystal and also on either side of the QPC. (Here we make use of the fact that the dielectric response time of the 2DEG is much shorter than the response time of the QPC itself.) The

corresponding shift in the electron energies in the reservoirs *L* and *R* is given by $d\varepsilon = 2dn / g_{2D} = (4e\mu d_{x4} / \varepsilon_r \varepsilon_0 w k_{TF})\, dz = \lambda\, dz$ where

$$\lambda = \frac{4e\mu d_{x4}}{\varepsilon_r \varepsilon_0 w k_{TF}} \qquad 2.1$$

describes the response of the chemical potential in the 2DEG to displacements of the GaAs crystal containing it. Using $\varepsilon_r = 13$, $k_{TF}^{-1} \approx 5\,\text{nm}$ and a typical crystal width $w = 2\ \text{mm}$ we estimate $\lambda \approx 2.4\,\text{fN}$.

We now need to consider the mechanical response of the crystal to a dipolar charge fluctuation *dn* at the location of the ohmic contacts. Such a charge fluctuation will lead to a free charge sheet density fluctuation $d\sigma_F = dn / w_c^{\,2}$ where w_c is a typical lateral dimension of the contacts. The presence of free charge at the surface of the crystal will induce a bulk polarization beneath it given by $dP_z = (\varepsilon_r - 1) d\sigma_F / \varepsilon_r$, where we have treated the contact as the top plate of a parallel plate capacitor. Piezoelectric coupling in GaAs will now lead to an induced strain fluctuation

$$dS = \frac{\varepsilon_r - 1}{\varepsilon_r} \frac{d\sigma_F}{\mu d_{x4}} = \frac{\varepsilon_r - 1}{\varepsilon_r} \frac{dn}{\mu d_{x4} w_c^{\,2}}$$

To find the mechanical force *dF* produced by a charge fluctuation *dn*, we first consider the elastic response of the crystal. Clearly $dF = k\, dy$ where $k = \omega_m^{\,2}\, m$ is the stiffness of the GaAs crystal when oscillating in the *Ey*-1 mode; for sample A, we find $k_a = 2.12 \times 10^8$ N/m using the known resonant frequency and mass of the sample. Since $dS = dy / l$, we may write

$$dy = \frac{\varepsilon_r - 1}{\varepsilon_r} \frac{l\, dn}{\mu d_{x4} w_c^{\,2}} = \frac{dF}{\omega_m^{\,2} m}$$

which leads directly to $dF = \eta\, dn$ where

$$\eta = \frac{\varepsilon_r - 1}{\varepsilon_r} \frac{\omega_m^{\,2} m l}{\mu d_{x4} w_c^{\,2}}.$$

For sample A, using $l = 3$ mm and $w_c = 100\ \mu$m, we find $\eta = 3.7 \times 10^{14}$ N/C. Even small charge fluctuations can therefore give rise to large forces on the sample. For instance, for a number fluctuation *dn* of only 10,000 electrons, we find $dF = 0.6$ N, a testament to the great strength of electrical forces, particularly when applied on the microscopic scales responsible for such phenomena as piezoelectricity.

2.4 System Hamiltonian and Master Equation

As described above in Section 2.2, our GaAs-based QPC is a naturally occurring electromechanical system consisting of a macroscopic mechanical oscillator whose position is continuously monitored by a mesoscopic electrical detector. The current section reviews the initial theoretical treatment devised by M.P. Blencowe including the system Hamiltonian and the resulting master equation. Although not reviewed in this thesis, this treatment has been further developed in conjunction with L.L. Benatov [47]. Part of this further work demonstrates that the bias dependent electro-mechanical coupling can be recast such that the tunnelling amplitude varies with the crystal's momentum and not its position.

Referring to Figure 2.3 , the quantum point contact (QPC) can be modelled as a tunnel barrier separating left (*L*) and right (*R*) reservoirs. The single electron energy levels of the *L* and *R* reservoirs are shifted in opposite directions proportionally to the *z* displacement. This shift corresponds to the piezoelectric effect associated with the flexing GaAs wafer being modelled as a potential difference between the two *L* and *R* 2DEG reservoirs.

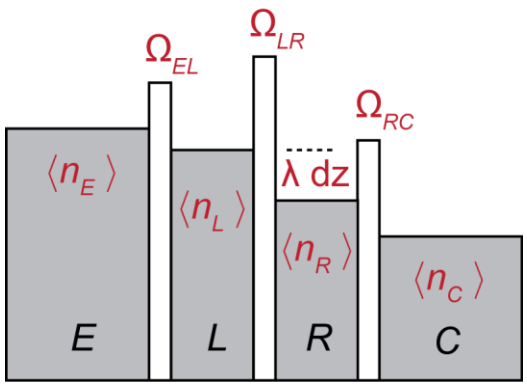

Figure 2.3 Model for chemical potential of QPC including non-negligible contact resistance of several kΩ. The model assumes that the metallic wires *E* and *C* connected to the crystal are held at a fixed potential difference while the potentials of *L* and *R* are free to change as electrons tunnel through the QPC. The electron distribution functions $\langle n_E \rangle$ and $\langle n_C \rangle$ for *E* and *C* are Fermi distributions, whereas the corresponding distributions $\langle n_L \rangle$ and $\langle n_R \rangle$ for *L* and *R* are not. The QPC is treated as a tunnel barrier with coupling Ω_{LR} and the ohmic contacts as tunnel barriers with coupling Ω_{EL} and Ω_{RC}.

The emitter (*E*) and collector (*C*) reservoirs are held at fixed chemical potential difference $\mu_E - \mu_C = eV_{CE}$ and couple to the *L* and *R* reservoirs, respectively, via some contact resistance modelled as tunnel barriers. The recognition of the presence of this contact resistance and its implications for the noise properties of the QPC is an important way in which our approach differs from the usual treatment, which treats the reservoirs *L*

and *R* as being held at fixed potentials. In particular the contact resistance allows the chemical potentials μ_L and μ_R to vary with the fluctuating charge distribution *dn* as electrons tunnel.

The Hamiltonian is given by $H = H_{\text{sys}} + H_{\text{bath}} + H_{\text{int}}$ where the system Hamiltonian is given by

$$H_{\text{sys}} = \hbar\omega_m a^\dagger a + \sum_L (\varepsilon_L + \lambda\hat{z}/2) b_L^\dagger b_L + \sum_R (\varepsilon_R - \lambda\hat{z}/2) b_R^\dagger b_R ,$$

the bath Hamiltonian is

$$H_{\text{bath}} = \sum_E \varepsilon_E b_E^\dagger b_E + \sum_C \varepsilon_C b_C^\dagger b_C ,$$

and the interaction Hamiltonian is

$$H_{\text{int}} = \sum_{E,L} \hbar\Omega_{EL} (b_E^\dagger b_L + b_L^\dagger b_E) + \sum_{C,R} \hbar\Omega_{CR} (b_C^\dagger b_R + b_R^\dagger b_C) + \sum_{L,R} \hbar\Omega_{LR} (b_L^\dagger b_R + b_R^\dagger b_L) .$$

Here *m* is the effective mass of the GaAs crystal containing the QPC and ω_m is the crystal's resonant frequency of interest. The operators b_i ($b_i^\dagger$) denote in shorthand the fermionic lowering (raising) operators for energy levels ε_i of a given reservoir $i = E, L, R, C$, while the operators *a* ($a^\dagger$) represent the lowering (raising) operators for the mechanical resonator. The parameter λ characterizes the piezoelectric coupling between the vibrational mode and reservoir electrons, while the Ω_{ij} characterize the contact resistance barriers between the various adjacent reservoirs. Unlike most treatments of electromechanical coupling to QPCs, this coupling does not modify the

QPC tunnel barrier, but instead acts as an additional voltage bias across the barrier. This is in accord with the observation that the coupling modifies the shot noise rather than acting as amplitude modulation, which would be expected from a modulation of the barrier height.

To gain a clearer idea about how the mechanical resonator and electron gas subsystems interact, we write down the master equation resulting from tracing over the bath degrees of freedom comprising the *E* and *C* reservoir electrons. The system probability density $\rho\left(\{n_L\},\{n_R\},N,z,v,t\right)$ is specified by the *L* and *R* reservoir level occupation numbers $n_L, n_R = 0,1$, and the oscillator position *z* and velocity *v*. The probability function also depends on the total number of electrons *N* that have traversed the *RC* barrier starting from some initial reference time. In terms of the system probability density, the Born-Markov approximated master equation is

$$\frac{\partial\rho}{\partial t} = \left[\omega_m{}^2 z + \frac{\lambda}{2m}\left(\sum_L n_L - \sum_R n_R\right)\right]\frac{\partial\rho}{\partial v} - v\frac{\partial\rho}{\partial z} + \gamma_{\text{ext}}\frac{\partial}{\partial v}\left(v\rho + \frac{k_B T}{m}\frac{\partial\rho}{\partial v}\right)$$
$$-2\pi\hbar\sum_{E,L}\Omega_{EL}^2\delta\left(\varepsilon_L + \lambda z/2 - \varepsilon_E\right)\left\{\begin{array}{l}\left[\left(1-n_L\right)\rho\left(n_L\right) - n_L\rho\left(n_L-1\right)\right]\left\langle n_E\right\rangle \\ +\left[n_L\rho\left(n_L\right) - \left(1-n_L\right)\rho\left(n_L+1\right)\right]\left(1-\left\langle n_E\right\rangle\right)\end{array}\right\}$$
$$-2\pi\hbar\sum_{C,R}\Omega_{CR}^2\delta\left(\varepsilon_R - \lambda z/2 - \varepsilon_C\right)\left\{\begin{array}{l}\left[\left(1-n_R\right)\rho\left(n_R,N\right) - n_R\rho\left(n_R-1,N+1\right)\right]\left\langle n_C\right\rangle \\ +\left[n_R\rho\left(n_R,N\right) - \left(1-n_R\right)\rho\left(n_R-1,N-1\right)\right]\left(1-\left\langle n_C\right\rangle\right)\end{array}\right\}$$
$$-2\pi\hbar\sum_{L,R}\Omega_{LR}^2\delta\left(\varepsilon_L - \varepsilon_R + \lambda z\right)\left\{\begin{array}{l}n_L\left(1-n_R\right)\rho\left(n_L,n_R\right) - \left(1-n_L\right)n_R\rho\left(n_L+1,n_R-1\right) \\ +\left(1-n_L\right)n_R\rho\left(n_L,n_R\right) - n_L\left(1-n_R\right)\rho\left(n_L-1,n_R+1\right)\end{array}\right\}$$

The first line in the master equation describes the resonator dynamics: the electron-induced piezoelectric force acting on the resonator depends on the relative charge imbalance between the *L* and *R* reservoirs on either side of the QPC. On the other

hand, the resonator-induced piezoelectric force acting on the electrons manifests itself through the *z*-dependent shifts of the *L* and *R* reservoir energy levels appearing in the energy conserving delta functions for the tunnelling electrons. The *E*, *C* baths are characterized by Fermi-Dirac distributions

$$\left\langle n_{E(C)} \right\rangle = \frac{1}{\exp[(\varepsilon_{E(C)} - \mu_{E(C)}) / k_B T] + 1}$$

where we assume the two baths are at the same temperature *T* but have different chemical potentials as a result of the applied voltage bias across the QPC: $\mu_E - \mu_C = eV_{CE}$. The counting variable *N* that tracks the total number of electrons that have traversed the *RC* barrier allows one to express the current noise in terms of the moments $\langle z \rangle$, $\langle N \rangle$, $\langle n_R \rangle$, $\langle N n_R \rangle$, $\langle Nz \rangle$ and $\langle z n_R \rangle$.

2.5 Frequency Dependent Shot Noise

This section discusses the remarkable frequency dependence noise signal that we observe and establishes its origin as shot noise. The presence of strongly frequency dependent shot noise was unanticipated in the literature with over 20 years of theoretical treatment assuming the presence of white shot noise. As part of our demonstration, we first present the dc characterization of a representative sample to show that we are dealing with a standard high quality device. Next, the initial rf characterization of the device is used to show the spontaneous strong frequency dependence we observe. The noise signal's power dependence is then analysed and shown to vary as $P_{in}^{1/2}$, the first signature of shot noise. Finally, the partition dependence of the signal is explored and shown to

vary appropriately with QPC conductance, the second signature of shot noise. Having established that the noise we observe is shot noise, subsequent sections describe the origin of the frequency dependence and its connection to mechanical modes of the crystal.

Figure 2.4 shows the essentials of our rf-QPC measurement step-up. A full discussion of the measurement set-up and device characteristics are provided in Sections 4.1 and 4.2. The QPCs studied were formed by depleting a GaAs/AlGaAs two-dimensional electron gas with a voltage V_g applied to metallic surface gates. We used standard lock-in techniques to measure the differential conductance G_{QPC} by applying a small excitation signal (V_{ac} = 20 μV at 13 Hz) to the dc port of the bias-tee while simultaneously recording the differential current. G_{QPC} was extracted from the raw data by accounting for series resistance in the measurement wiring and sample, and for the shunt capacitance of the coaxial feedline, such that $G_{QPC} \approx G_0$ on the first plateau and $G_{QPC} \approx 0$ at pinch-off. Application of a dc voltage V_{dc} allowed for measurement of nonlinear differential conductance G_{QPC} versus both V_g and V_{dc}. For charge sensitivity measurements, an ac voltage V_m applied to the QPC gates in addition allowed for modulation of G_{QPC}.

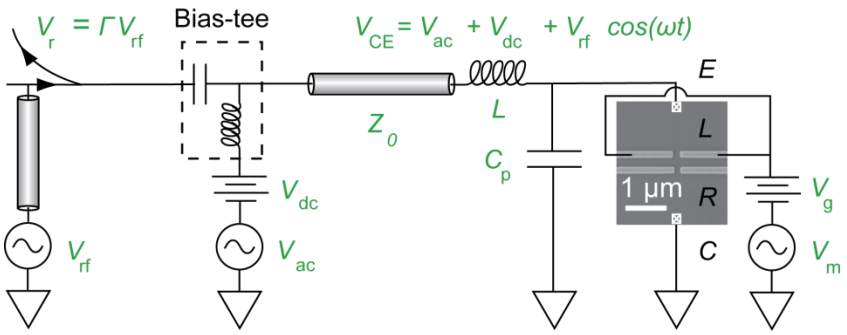

Figure 2.4 Schematic of rf-reflectometry measurement circuit with SEM image of a representative device. RF V_{rf}, dc V_{dc}, and near-dc V_{ac} voltages are applied to the current path of the sample via a bias-T. The chemical potentials of the leads μ_E and μ_C are considered fixed whereas the chemical potentials of the 2DEG μ_L and μ_R are separated by contact resistances and hence free to fluctuate with the electron density *dn*. The sample is embedded in a tank circuit consisting of a spiral chip inductor *L*, the sample R_d, and the inherent parasitic capacitance C_p. The conductance of the QPC G_{QPC} can be externally adjusted with ac V_m and dc V_g voltages. As the impedance of the tank circuit *Z* depends on G_{QPC}, changes in the conductance modulate the reflected signal V_{rf} allowing fast signal detection (see Sections 1.7 and 4.1 for additional details).

As described above in Section 1.7, the large bandwidth of the system is achieved via RF-reflectomery [32] that allows for microwave measurements simultaneously with the dc and near dc characterization. Embedding the QPC in an *LC* tank circuit impedance matches the high resistance of the QPC, R_{QPC} ~10 kΩ, to a standard 50 Ω transmission line. To perform the fast measurements, a high frequency signal V_{rf} is applied to the tank circuit via a bias-tee and the reflected signal $V_r = \Gamma V_{rf}$ is measured. As the reflection coefficient Γ depends on the differential conductance G_{QPC} of the QPC, changes in G_{QPC} modulate V_r and allow for time resolved measurements down to ~ 1 µs. The bandwidth of the system is determined by the width of the tank circuit resonance,

$\Delta f = f_0 / Q \approx 60\,\text{MHz}.$

Figure 2.5 shows the dc characterization of our most sensitive rf-QPC sample (Sample A). The linear differential conductance data $G_{QPC}(V_g)$ shows well-defined

plateaus at integer multiples of the conductance quantum $G_0 = 2e^2/h$, the classic signature of ballistic 1D transport with its quantized transverse conduction channels.

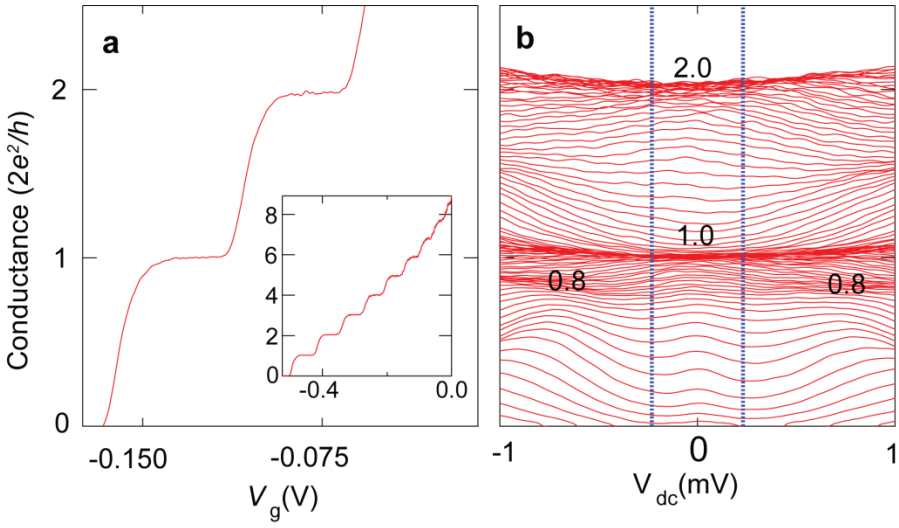

Figure 2.5 (a) Measurements of sample A of G_{QPC} versus gate voltage V_g at zero magnetic field showing standard 1D sub-bands. Inset: G_{QPC} after exposure of the sample to light, showing multiple conductance plateaus. (b) Nonlinear differential conductance G_{QPC} (V_{dc}, V_g). The vertical dashed lines indicate the estimated rms rf voltage V_{rf} applied to the QPC for noise measurements shown in Figure 2.6. (Data from M. Thalakulum Thesis [41].)

The non-linear measurements in Figure 2.5(b) record the differential conductance G_{QPC} (V_g, V_{dc}) as a function of both the gate V_g and bias voltage V_{dc}. For $T < 500$ mK, there is a peak in G_{QPC} around $V_{dc} = 0$ for QPC conductance in the range $0 < G_{QPC} < G_0$. This zero-bias anomaly has been studied previously [5] and interpreted as the onset of Kondo physics in a QPC, [5], [48] as has an additional plateau at finite bias ($V_{dc} \approx 700$ μV) for which $G_{QPC} \approx 0.8\ G_0$ [5].

Figure 2.6 shows the spontaneously generated structure representative of our rf data measurements. The data shown is from Sample A. The QPC conductance was set in

the tunneling regime around $G_{QPC} \approx 0.5\ G_0$, an RF excitation V_{rf} was applied, and the reflected power spectrum P_n was measured.

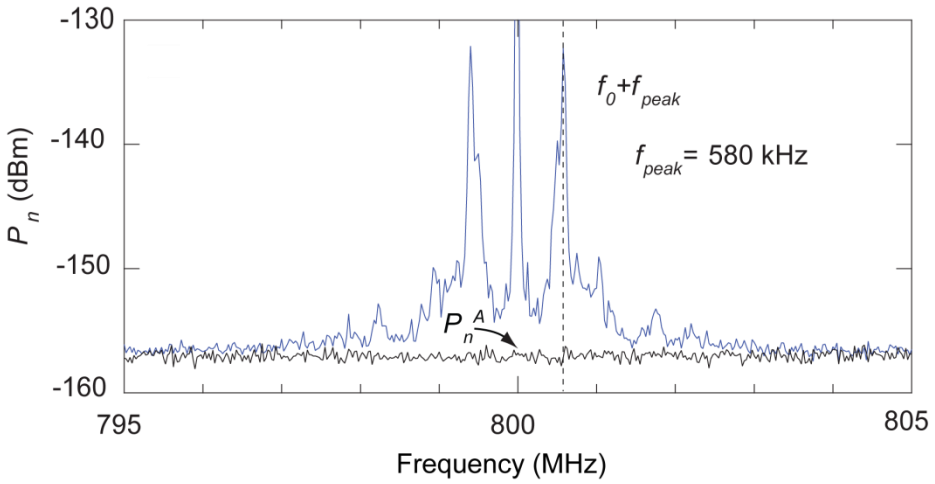

Figure 2.6 Output power spectrum P_n of the rf-QPC for input power $P_{in} = -78$ dBm and $G_{QPC} \approx 0.5 G_0$ for Sample A. The output signal includes a central peak at the drive frequency $f_0 = 800$MHz and strong frequency dependent features at ~ ± 580 kHz. The frequency dependent features are spontaneously generated as no external modulation other than f_0 is applied to the sample's bias or gate lines. Also noteworthy, as described below, these features clearly exceed the noise floor of the cryogenic HEMT amplifier P_n^A. (Data from M. Thalakulum Thesis [41].)

Remarkably, the signal is strongly frequency dependent with pronounced spontaneously generated peaks at $f = f_0 \pm 580$ kHz, where $f_0 = 800$ MHz is the tank circuit's resonance. As are discussed below, the spontaneously arising features in P_n are in fact the shot noise of the QPC. Furthermore, they are electromechanical in origin and arise from the coupling of a particular normal vibrational mode in the GaAs crystals to electrons in the 2DEG.

Since P_n depends on P_{in} and G_{QPC} (see below), it is clearly associated with the QPC. A review of the corresponding time domain signal reveals that the frequency

features are stochastic, i.e. noise. There are two broad categories into which such noise might fall: modulation noise, for which current through the QPC is amplitude modulated, and shot noise [49]. Modulation noise scales with input power at least as $P_n \propto P_{in}$ whatever its origin, whether the motion of trapped charges in the substrate, electromagnetic noise coupled to the QPC gates, mixing due to the QPC nonlinearity, or some other source [49]. Shot noise, in contrast, scales as $P_{in}^{1/2}$ [43], [50].

To help evaluate the power dependence of P_n, we created a known modulation signal P_s for comparison, as shown in Figure 2.7(a). When a small ac voltage V_m at 97 kHz was applied to the QPC gates, the rf-QPC output showed clear side peaks of size P_s at $f_0 \pm 97$ kHz, indicative of the amplitude modulation riding on a broad noise background. As we varied P_{in}, we found that $P_s \propto P_{in}$ over three decades before the excessive modulation drive caused the response to saturate, as shown in Figure 2.7(b).

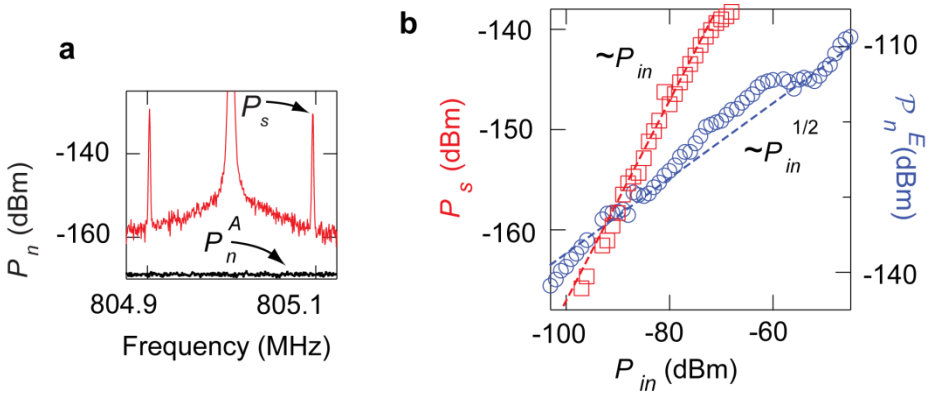

Figure 2.7 (a) The reference modulation signal P_s is generated by applying an ac excitation to the QPC gates of Sample A. (b) The dashed lines are guides to the eye showing that the modulation signal P_s (red squares, left axis) scales as ~ P_{in} while the integrated excess noise $\mathcal{P}_n^E$ (blue circles, right axis) scales as $P_{in}^{1/2}$, the first signature of shot noise. (Data from M. Thalakulum Thesis [41].)

To properly evaluate P_n for the noise features in Figure 2.6, we examined the integrated excess noise $\mathcal{P}_n^E$ in a 4.8 MHz bandwidth above f_0. In contrast to P_s, $\mathcal{P}_n^E$ scales as $P_{in}^{1/2}$ over nearly five decades (see Figure 2.7(b)) strongly suggesting that the spontaneous spectral features in P_n are shot noise. For this to be the case, however, the spectral features must not only scale as $P_{in}^{1/2}$, but must also show partition dependence.

Partition dependence arises from the stochastic partitioning of a discrete charge stream into transmitted and reflected beams by the QPC tunnel barrier. The resulting shot noise is maximal when the conduction channel is partially transmitting and minimal when completely closed or open [43]. This is exactly what we observed. The spectral noise features vanished [red (green) trace in Figure 2.8(a)], and the corresponding $\mathcal{P}_n^E$ is minimal [red (green) line in Figure 2.8(b)] when the differential conductance G_{QPC} was 0 and G_0, respectively. Similarly the noise features were present [black trace in Figure 2.8(b)], and $\mathcal{P}_n^E$ is maximal [black line in Figure 2.8(b)] when $G_{QPC} \approx 0.5G_0$. The suppression of the measured shot noise relative to the single-particle theory for $G_{QPC} \gtrsim 0.5$ has been observed by others and attributed to the many body physics of the 0.7 structure [51].

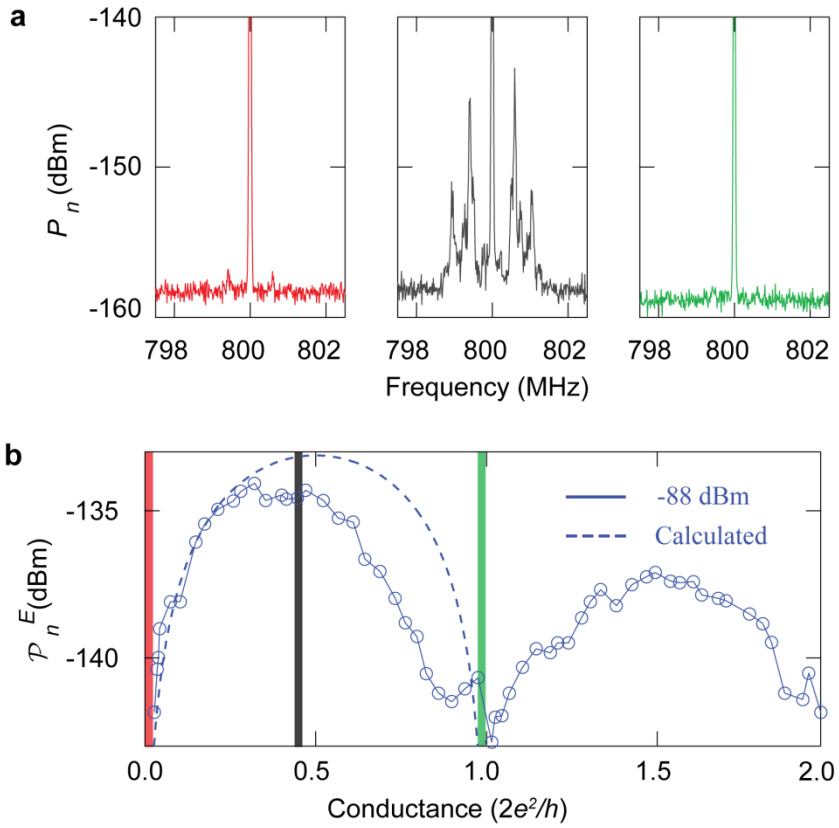

Figure 2.8 (a) The reflected power spectra P_n for P_{in} = -88 dBm and $G_{QPC} \approx 0$ (red), $G_{QPC} \approx 0.5G_0$ (black), and $G_{QPC} \approx G_0$ (green) showing that P_n is minimal for fully open or closed channels, and maximal for half-open channels, the second signature of shot noise. Data from Sample A. (b) Quantitative comparison of measured shot noise with theory. The measured integrated excess noise $\mathcal{P}_n^E$ (blue circles) and the calculated integrated noise power $\int (2L/C_p Z_0) S_I(\omega, \omega_0) df$ (blue dashes) as a function of QPC differential conductance G_{QPC}. (Data from M. Thalakulum Thesis [41], calculations subsequent.)

In addition to this striking qualitative correspondence, our data show close quantitative agreement with a theoretical calculation of the magnitude of the shot noise as a function of QPC conductance. In our experiment, shot noise arises from the partition noise of electron hole pairs created by the rf voltage V_{rf}^{QPC} across the QPC, so called photon assisted shot noise (PASN) [43], [45], [50], [52]. Assuming energy independent

transmission coefficients T_n, it can be shown (See appendix, Section 6.1) that the spectral density of photon-assisted shot noise is given by

$$S_I(\omega,\omega_0) = \frac{4e^2}{h}\sum_n T_n(1-T_n)\sum_{l=-\infty}^{\infty}(\hbar\omega + l\hbar\omega_0)J_l^2(\alpha)\coth\left[\frac{\hbar\omega + l\hbar\omega_0}{2k_BT}\right]$$

where $\alpha = \sqrt{2}eV_{\mathrm{rf}}^{\mathrm{QPC}}/\hbar\omega_0$. The expression for $S_I(\omega, \omega_0)$ is only very weakly frequency dependent and cannot account for the spectral features we observe. For low temperatures and $\alpha \gg 1$, the infinite sum can easily be evaluated and scales as $\alpha \propto P_{in}^{1/2}$. Our data confirm that the measured $\mathcal{P}_n^E$, Figure 2.8(b) - blue circles, is well described by a theoretical calculation of the shot noise $S_I(\omega, \omega_0)$ integrated over the same bandwidth and converted to voltage noise[25] by the tank circuit, Figure 2.8(b) -blue dashed line. For the partition power dependence data shown in Figure 2.8(b), we shifted the calculated noise power downward by 3.9 dB but used no other fitting parameter.

The partition dependence and $P_{in}^{1/2}$ scaling of $\mathcal{P}_n^E$ together conclusively demonstrate that the spectral features we observe, despite their unusual nature, are in fact shot noise. Additional details on our calculation of the integrated excess noise $\mathcal{P}_n^E$ are discussed in the appendix, Section 6.1

2.6 Feedback Loop Coupling Electrical and Mechanical Degrees of Freedom

Having established that the source of the frequency features is shot noise, this section develops further the details of how the initial white shot noise spectrum is transformed through the feedback loop between current flow and crystal vibrations. In

particular our analysis demonstrates that the spectral features arise from the coupling of electronic transport to a particular normal vibrational mode of the GaAs crystal that possesses a piezoelectric polarization field as illustrated in Figure 2.1. In all we collected data from eight samples and found that the spectral features depended only on sample geometry and not on other parameters such as magnetic field, temperature, drive frequency, or matching network [41].

Figure 2.9 shows data from two representative samples (A and B) with different geometries and gate configurations. We numerically solve [53],[54] for the three dimensional normal vibrational modes as determined by sample dimensions and the material parameters of GaAs. We find close correspondence between our data and the predicted frequencies for the *Ey*-1 flexural mode [53]. As discussed below, this mode is excited is due to a combination of sample-specific ohmic contact and QPC gate geometry. This mode combines large flexural motion in *y* with small shear displacements *dz* in the vicinity of the QPC such that $dy = \beta dz$, where $\beta >> 1$ is a geometry-dependent dimensionless parameter.

The rf data for sample A is reproduced in Figure 2.9(a) with an additional value of P_{in} (-98 dBm) and a top-down view of the sample's geometry. The dimensions of sample A yield a resonant frequency f_a = 510 kHz that falls almost exactly on the shot noise peak. To further demonstrate coupling of the shot noise to the *Ey*-1 mode, we engineered sample B to move the shot noise peak to a frequency of ~ 1 MHz, providing a large bandwidth for charge detection with reduced shot noise. Based on the dimensions of sample B, we predict f_b = 1.07 MHz, remarkably close to the measured feature peak, as

shown in Figure 2.9(b). Note that as the power is increased (from red to black) the broadband shot noise decreases while the total increases becoming concentrated at the sample's resonant frequency, supporting the observation that the initially white electronic noise spectrum is transformed by its coupling to a resonant mode.

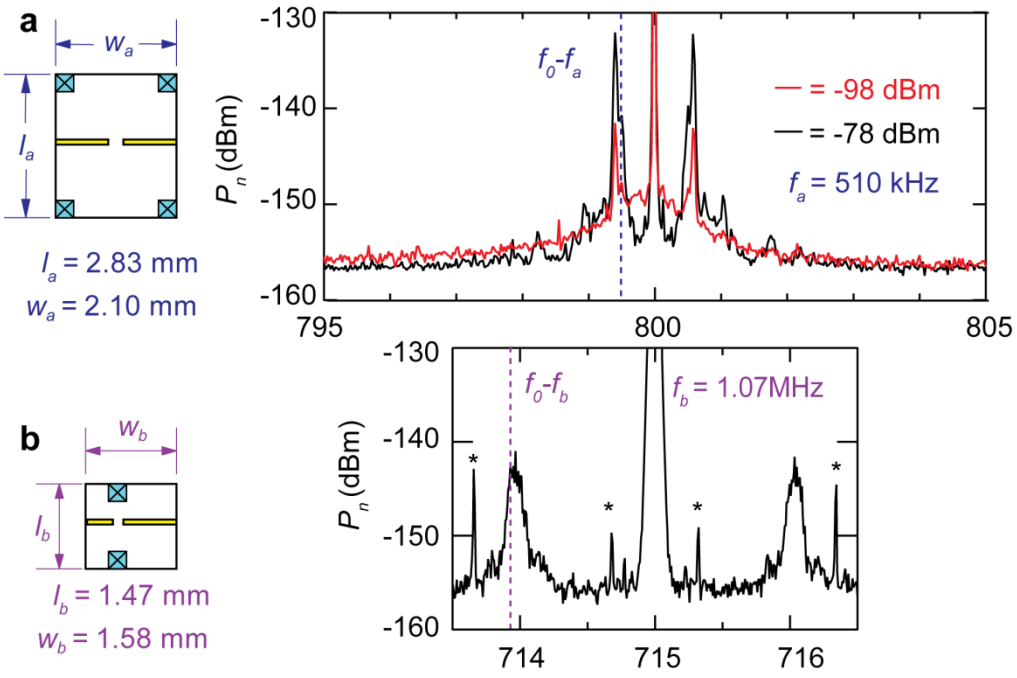

Figure 2.9 (a) The reflected power spectrum P_n from sample A reproduced with the inclusion of data from an additional input power excitation (P_{in} = -98 dBm). On left: a diagram of the sample geometry including the ohmic contacts (blue crossed-boxes), QPC (yellow rectangles), and linear dimensions. The calculated value for the excited 3D acoustic mode (f_a = 510 kHz) falls almost exactly on the shot noise peak. (b) The shot noise spectrum for sample B whose dimensions were chosen to generate a coupled resonant mode of ~ 1MHz. On left: the sample dimensions shown correspond to a predicted resonant frequency (f_b = 1.07 MHz) remarkably close to the shot noise peak. The sharp starred features are modulation noise rather than shot noise and scale as P_{in}, not $P_{in}^{1/2}$.

The frequency calculations discussed above include a fitting parameter of 10 percent (f_{meas}= 0.9* f_0) that likely accounts for factors such as material parameter differences between our GaAs/AlGaAs 2DEG material and generic GaAs. In addition at

the shallow 100 nm depth of the 2DEG, the acoustic excitation may include a surface wave perturbation to the bulk mode. Individual frequency deviations for particular samples may be attributable to factors such as actual non-ideal rectangular geometries and crystal defects.

A detailed examination of the three dimensional polarization field ***P*** associated with the *Ey*-1 mode indicates that it is in fact capable of coupling to electrons in the 2DEG. As shown in Figure 2.1, the polarization ***P*** at the location of the 2DEG contains a nearly constant *x*-component that couples the mechanical motion to transport through the QPC. In addition, the polarization at the location of the ohmic contacts has a strong dipolar component in the *z* direction that couples to dipolar charge fluctuations in the reservoirs *L* and *R*, allowing for efficient electrical actuation of the mechanical mode.[28] The presence of the *Ey*-1 mode means that a measurement of QPC current is necessarily also a measurement of lattice displacement *dz*. The resulting backaction then requires the existence of a feedback loop, as discussed with respect to Figure 2.2.

Intuition into the transformational properties of the feedback loop can be gained by considering by analogy a white noise source, such as electrical current noise generating static from a speaker, and a resonant system, such as a glass. The feedback loop consists of two halves: a speaker that transfers energy from the current to the glass and a microphone that transfers energy from the glass to the current. Although all frequencies are initially present in the electrical noise, the glass responds to the static at its resonant frequency, and this, coupled with the feedback loop, leads to a spectrum

heavily weighted at the resonant frequency as the ringing of the glass causes an increased acoustic drive at this frequency.

In our system the initial white noise is broadband shot noise. Analogous to above, one half of the feedback loops consists of energy being transferred from the current to acoustic vibrations of the crystal. This occurs by macroscopic charge fluctuations in the ohmic contacts inducing a polarization field that piezoelectrically excites an acoustic mode. In the other half of the feedback loop, also analogous to above, energy from the acoustic vibration is returned to the current. In particular the acoustic vibration generates an in plane polarization field $\boldsymbol{P}$ that combines with an electric displacement field $\boldsymbol{D}$ to create an ac bias across the QPC. The ac bias causes correlations in the tunnelling of electrons at the resonant frequency. This increases the weight of the PASN at this frequency and completes the feedback loop.

Figure 2.10 shows in more detail the interaction of the polarization field $\boldsymbol{P}$, the electric displacement field $\boldsymbol{D}$, and the free charge. The figure also presents a device geometry with two perpendicular QPCs that is used to test the feedback hypothesis. As shown, the component of the polarization field $\boldsymbol{P}$ in the plane of the 2DEG for the flexural mode we observe is nearly constant and points along the transport direction connecting the ohmic contacts. In the high conductance regions, free charge in the 2DEG generates an electric displacement field $\boldsymbol{D}$ that screens the polarization field $\boldsymbol{P}$ resulting in no net electric field $\boldsymbol{E} = \frac{1}{\varepsilon_0}(\boldsymbol{D} - \boldsymbol{P}) = 0.$ Under the gates and in the QPC, however, the polarization $\boldsymbol{P}$ and electric displacement $\boldsymbol{D}$ fields combine to create an electric field $\boldsymbol{E}$, and hence a bias voltage, across QPC 1 but not across QPC 2.

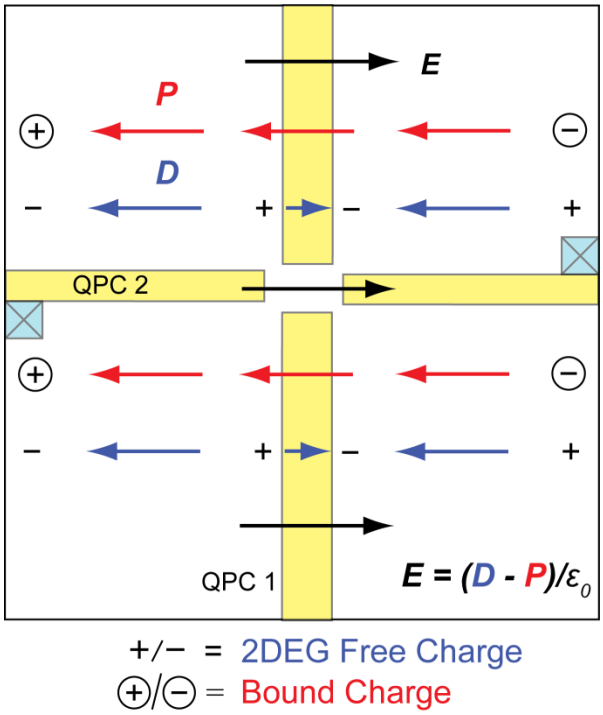

Figure 2.10 Details of a sample with two perpendicular QPCs (QPC 1 and QPC2) used to test the piezoelectric feedback hypothesis. In the high conductance regions, the 2DEG free charge naturally arranges itself to screen the bound charge. Under the gates and in the QPC gap, however, the polarization field ***P*** and the displacement field ***D*** combine to create a net electric field ***E*** across QPC 1 but not QPC 2.

Figure 2.11 presents the data used to verify the existence of the feedback loop with sample C, a device having the gate geometry discussed in Figure 2.10. Energizing QPC 1 generates shot noise with the proper partition dependence, i.e., no noise when the channel is open or closed and maximum noise when partially transmitting. By contrast, energizing QPC 2 breaks the feedback loop at the asterisk in Figure 2.2, since lattice displacement in this case does not result in a bias across QPC2. The resulting noise spectrum (inset) shows no frequency dependent noise features even for a partially transmitting barrier. The peak for QPC 1 again falls close to the frequency f_c = 839 kHz predicted by the sample dimensions.

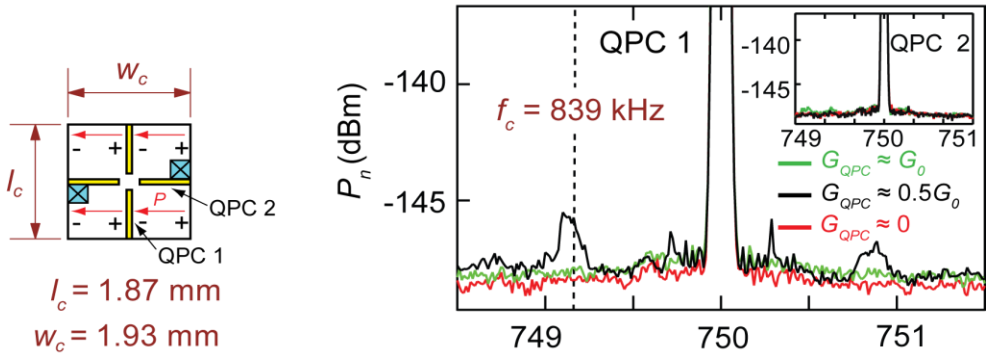

Figure 2.11 The reflected power spectra P_n for QPC 1 and QPC 2 in sample C when $G_{QPC} \approx 0$ (red), $G_{QPC} \approx 0.5G_0$ (black), and $G_{QPC} \approx G_0$ (green) showing partition dependence for QPC 1 but no shot noise features for QPC 2. This confirms the existence of a backaction-mediated feedback loop between the shot noise and the normal vibrational mode. Without a bias across QPC 2, energy transferred to the *Ey*-1 mode cannot be returned to the current, thereby breaking the feedback loop. On left: the sample dimensions again correctly predict the location of the peak in the shot noise.

2.7 Generation and Geometry of Resonant Modes

In general as part of the shot noise piezoelectric mediated feedback loop present in our system, the excitation of an acoustic mode has two necessary aspects. First as shown and discussed with respect to Figure 2.1, the piezoelectric polarization field that is associated with the crystal deformation of an acoustic mode must contribute to a bias across the QPC. This is required so that acoustic mode energy can be transferred to the current. Second, the induced polarization field due to bound charge induced by current in the ohmic contacts must closely match the acoustic mode's piezoelectric polarization field. This is required so that charge fluctuations can in turn excite the acoustic mode thereby transferring energy from the current to mechanical vibrations of the crystal.

Figure 2.12(a) shows the calculated 3D geometry [53–55] of the displacement field at the top, bottom and middle of the sample for the flexural acoustic mode we observe, which is the *Ey*-1 mode according to the notation of Ohno [53]. The largest amplitude motion of this mode is flexural displacement in *y* at the ends of the sample. At its center, the sample undergoes shear displacement such that it is pinched along one edge and bloated on the other. An expanded view of the displacement is shown in Figure 2.12(b), which focuses on a *y*-*z* cross-sectional plane showing the upper 50 μm of the crystal immediately beneath the QPC. Downward displacement *dz* for negative *y* changes to upward displacements *dz* for positive *y*, resulting in a shear strain S_{yz} at the QPC. The *z* displacements that cause the strain are typically significantly smaller than the corresponding *y* displacements. We write $dy = \beta\, dz$ where $\beta >> 1$ is a sample dependent dimensionless parameter that we determine from the mode calculations. For sample A, we find $\beta \approx 100$. A description of the method used to calculate the full displacement fields and the resulting strain and polarization fields is presented in Section 6.2 of the Appendix.

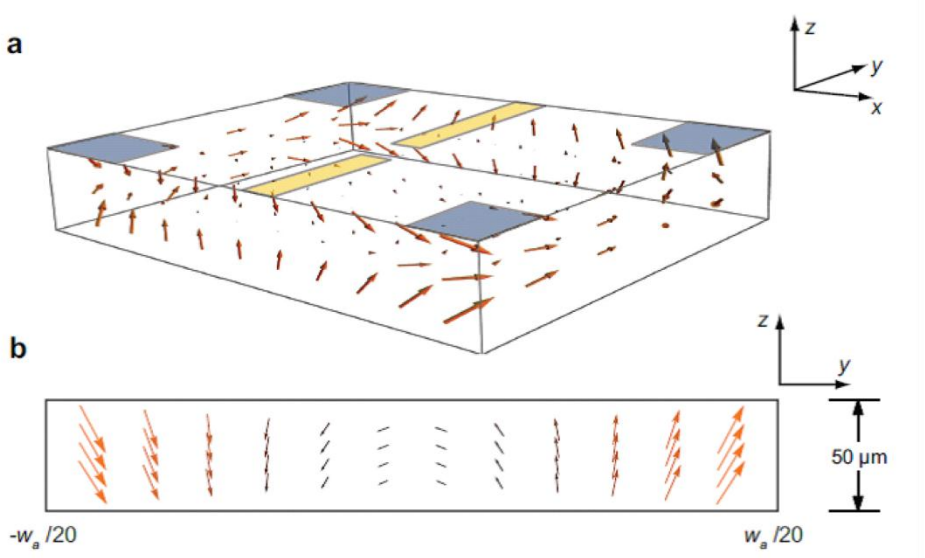

Figure 2.12 (a) Calculated displacement field of the *Ey*-1 mode for Sample A. Approximate locations of the ohmic contacts are shown by the blue squares, while the QPC location is shown by the yellow rectangles. In this figure the *z* displacement has been multiplied by a factor of 100 so that it is clearly visible. (b) Displacement field in the *x*-*z* plane near the center of the crystal, within 50 µm of the surface beneath the QPC. The *z* displacement varies with *y* changing both magnitude and sign, giving rise to a strain S_{yz} at the location of the QPC.

The piezoelectric polarization field for the *Ey*-1 mode displacement field of Figure 2.12 is shown in Figure 2.13(a) and Figure 2.14(a). This mode shows a dipolar *z*-component of the total polarization, as well as a nearly constant component in the *x* direction that is strongest at the top and bottom of the sample. Due to the location of the 2DEG, the field at the top of the sample is the one directly involved in the electromechanical coupling. In particular, for our sample geometry, free charge in the ohmic contacts induces a macroscopic layer of bound surface charge that generates an induced 3D polarization field that closely matches the piezoelectric polarization field.

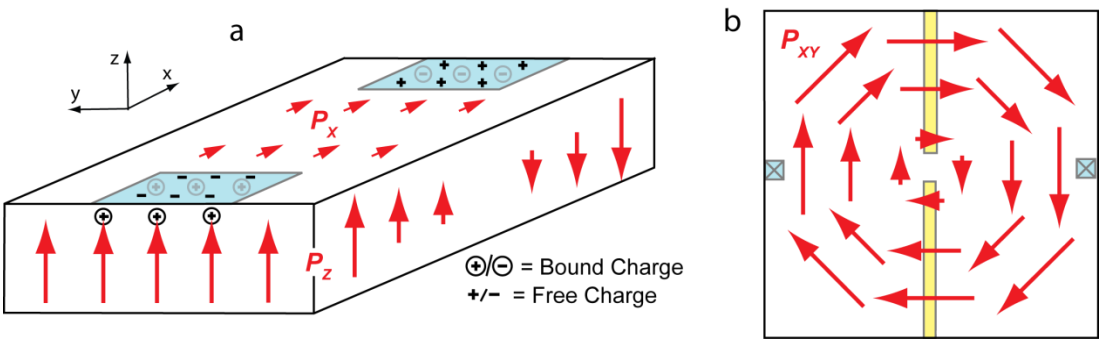

Figure 2.13 (a) Schematic of polarization field for the upper portion of sample A for the *Ey*-1 mode. The *z* component of polarization P_z is dipolar for this mode (opposite orientation at opposite ends of the sample), allowing efficient electromechanical coupling of charge dipoles to the strain field. The polarization also shows a nearly constant P_x component, allowing the strain to induce transport across the QPC. In this figure the value of P_z is not to scale and has been reduce by a factor of ~ 100 relative to the P_x component. (b) Schematic of piezoelectric polarization field of an acoustic mode that does not generate a bias across a QPC located at the sample center or couple efficiently to charge dipoles at the ohmic contacts. P_z has not been rescaled relative to P_x in this figure.

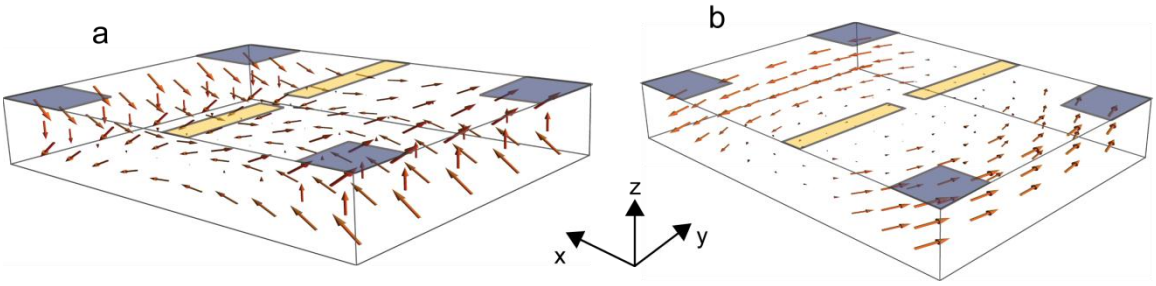

Figure 2.14 (a) Calculated piezoelectric polarization field for the top, middle, and bottom of the *Ey*-1 mode, shown as a schematic in Figure 2.13(a). In this figure, the plotted value of P_z has been divided by a factor of 100 so that the much smaller P_x component is clearly visible. (b) Calculated piezoelectric polarization field for the mode shown in Figure 2.13(b) as a schematic in which the field does not generate a bias across the QPC.

This 3D geometric correspondence between the induced and piezoelectric polarization fields can be seen by imagining the field lines from the bound surface charge in Figure 2.13(a). These field lines will be concentrated and perpendicular directly under the ohmic contacts and horizontal and dispersed in the middle regions of the sample, as with the piezoelectric polarization field. In addition, the voltage difference between the

ohmic contacts means that bound charge of different signs, and hence an induced polarization field with opposing orientation, is generated at opposite ends of the sample, again in accordance with the piezoelectric polarization field. Reflecting the disparity in the size of *y* and *z* displacements, the perpendicular component P_z at one end of the sample is up to two orders of magnitude larger than the in-plane component P_x. (Note that in Figure 2.14(a), P_z is divided by a factor of 100 relative to P_x so that the latter component is clearly visible.) Interestingly, the dimensions of our most sensitive sample correspond to a ratio of $P_z / P_x \sim 10^2$, the largest of the three samples, suggesting this ratio may most closely match the polarization field induced by our ohmic contact geometry.

For the numerous modes that we do not prominently observe, either the geometry of the piezoelectric polarization field is wrong or its magnitude is too low. A first failure in geometry is related to coupling to the external circuit. For example, we do not observe any torsional modes as these couple strongly to side gates and only weakly to our surface gates [56]. A second failure in geometry is that the polarization field does not generate a significant bias across the QPC. Figure 2.13(b) and Figure 2.14(b) show an example of such a mode. In particular, the circular in-plane field P_{xy} vanishes at the sample center, the location of QPCs in our experiments. In addition to geometric considerations, many of the modes not excited generate strain fields, and hence polarization fields, orders of magnitude smaller than the flexural mode we observe.

2.8 Displacement Analysis

This section relates our measurements of electrical noise to displacements of the GaAs crystal. Assuming a Lorentzian profile for the satellite peaks in the measured

excess noise power P_n^E, we can relate the mean squared voltage noise across the QPC $\langle V_n^2 \rangle$ to the peak excess voltage $V_{n,peak}$ as follows.

Consider a driven harmonic oscillator

$$\ddot{V} + \frac{\omega_0}{Q}\dot{V} + {\omega_0}^2 V = \frac{F_0}{m} e^{i\omega t}, V = V_n e^{i\omega t}$$

$$V_n V_n^* = \frac{{F_0}^2}{m^2} \frac{1}{(\omega^2 - \omega_0^2)^2 + \left(\omega\omega_0 / Q\right)^2}$$

so that when driven at resonance, the magnitude of the amplitude is given by

$$\left|V_{n,peak}\right|^2 = \frac{F_0^2 Q^2}{m^2 \omega_0^4}.$$

The root-mean-square value of a response to voltage noise $S_V(\omega)$ in V^2/Hz is calculated assuming white noise $S_V(\omega) = S_V$

$$\langle V_n^2 \rangle = \int_0^\infty \frac{S_V}{m^2} \frac{1}{\left(\omega^2 - \omega_0^2\right)^2 + \left(\omega\omega_0 / Q\right)^2} d\omega$$

$$= \frac{S_V}{m^2 \omega_0^3} \frac{\pi Q}{2} = \left|V_{n,peak}\right|^2 \frac{\pi\omega_0}{2Q} \qquad 2.2$$

The peak voltage $V_{n,peak}$ is calculated from the peak excess noise power $P_{n,\max}^E$, the conductance of the QPC G_{QPC}, the fraction of available power from the rf-QPC that is

transferred to our measurement circuitry $K \approx 0.16$, and the resolution bandwidth of the spectrum analyzer used in the noise power measurement RBW:

$$dV_n^2 = \left\langle V_n^2 \right\rangle = \frac{\pi f_m}{2Q_m} V_{n,peak}^2 = \frac{\pi f_m}{2Q_m} \frac{P_{n,\max}^E}{G_{\mathrm{QPC}} K \ \mathrm{RBW}}.$$

We then use $dz^2 = d\varepsilon^2 / \lambda^2 = dV^2 (e/\lambda)^2$ to relate voltage fluctuations across the QPC to mechanical fluctuations *dz* and *dy*:

$$dz = \frac{e}{\lambda} \sqrt{\frac{\pi f_m}{2Q_m} \frac{P_{n,\mathrm{peak}}^E / \mathrm{RBW}}{G_{\mathrm{QPC}} K}}, \text{ and}$$

$$dy = \beta dz = \beta \frac{e}{\lambda} \sqrt{\frac{\pi f_a}{2Q_m} \frac{P_{n,\mathrm{peak}}^E / \mathrm{RBW}}{K G_{\mathrm{QPC}}}} \approx 50\,\mathrm{nm}$$

where Q_m = 15 is the quality factor of the mechanical resonance as determined from its spectral width, and $\beta \approx 100$ for sample A. These expressions are used to compute the rms displacements *dy* and *dz* versus frequency and input power shown in Figure 2.15. From this is easy to show that our oscillations are clearly non-equilibrium. A typical thermal vibration y_{th} for sample A for a lattice temperature T = 40 mK and m_a = 16 mg is given by $y_{\mathrm{th}} = \sqrt{k_B T / m\omega_a^2} \approx 0.05\,\mathrm{fm} \ll dy \approx 50\,\mathrm{nm}$.

To estimate displacement sensitivity, we replace the mean square excess noise $(\pi f_m / 2Q_m)(P_{n,\max}{}^E / \mathrm{RBW})$ in our estimate of *y* displacement with the HEMT amplifier noise floor per hertz P_n^A / RBW = -157 dBm/RBW, giving a sensitivity to *y* displacements of $\delta y \approx 1 \times 10^{-11} \mathrm{m}/\sqrt{\mathrm{Hz}}$. For a smaller resonator with a width of roughly 100 nm we

would expect a sensitivity of $\delta y \approx 6\times10^{-16}\,\mathrm{m}/\sqrt{\mathrm{Hz}}$; this compares favourably with sensitivities achieved using an SET charge detector [57].

2.9 Fano Factor – Backaction and Electron-Electron Correlations

In addition to macroscopic manifestations of quantum mechanical backaction, the feedback loop in our system also generates correlations in the tunnelling of electrons through the QPC as has been predicted. As mentioned above, once the crystal is oscillating at its resonant frequency, the piezoelectric coupling generates an ac bias across the QPC at this same frequency. Because the individual electron tunnelling rate is much faster than the crystal's resonant frequency (the tunnelling current is on the order of ~1nA = 1 GHz >> ~ 1MH) , the correlations in electron tunnelling are due to the oscillating bias causing oscillating periods in the number of tunnelling events. This bunching in the tunnelling of electrons is referred to as super-Poissonian noise.

Mathematically we can explore the correlations in electron tunnelling via a frequency dependent Fano factor. For dc currents, the Fano factor is given by $\mathcal{F}_{\mathrm{dc}} = S_I(0)/2eI = \sum_n T_n(1-T_n)/\sum_n T_n$ in QPCs; super- and sub-Poissonian correlations (bunching and anti-bunching of electrons) correspond to $\mathcal{F}_{\mathrm{dc}} > 1$ and $\mathcal{F}_{\mathrm{dc}} < 1$ respectively. Since here we measure photon-assisted shot noise, we define a frequency-dependent Fano factor as $\mathcal{F}(\omega) = \mathcal{F}_{\mathrm{dc}} S_I^{\mathrm{meas}}(\omega)/S_I(\omega,\omega_0)$ where $S_I^{\mathrm{meas}}(\omega)$ is the measured current noise spectral density determined from P_n^E and $S_I(\omega,\omega_0)$ as specified above in equation 1.27. As can be seen in Figure 2.15, $\mathcal{F}(\omega)$ is strongly frequency dependent.

Furthermore, it rises to larger than 100 near the resonant frequency of the crystal, while dropping to roughly 0.1 away from resonance. The electromechanical coupling thus has a powerful effect on electron-electron correlations at different frequencies, with both strongly super- and sub-Poissonian noise coexisting in our samples.

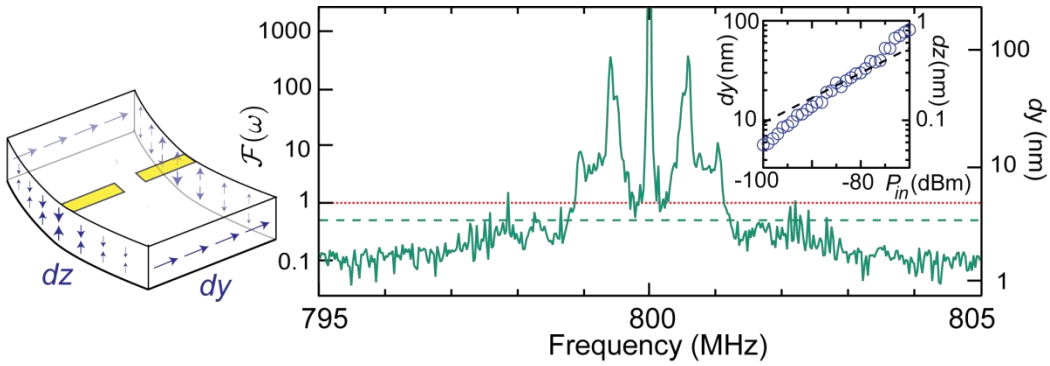

Figure 2.15 Left axis: frequency dependent Fano factor $\mathcal{F}(\omega)$ for sample A for $P_{in} = -68$ dBm, showing dramatically super-Poissonian ($\mathcal{F} \gtrsim 100$) and sub-Poissonian ($\mathcal{F} \approx 0.1$) noise as a function of frequency. The red dotted line indicates Poissonian noise, while the green dashed line gives the Fano factor $\mathcal{F}(\omega) = \mathcal{F}_{dc} = 0.5$ expected for an uncoupled detector. Note logarithmic scale. Right axis: displacement *dy* versus frequency, showing the strongly non-thermal nature of the resonator dynamics. Inset: displacement *dy* (left axis) and *dz* (right axis) versus input power for sample A. The dashed line is a guide to the eye showing scaling as $P_{in}^{1/2}$. On left: blue arrows indicate the *dy* and *dz* deformation of the crystal in the *Ey*-1 mode.

Similar effects on correlations of electron tunnelling events in the detector have been predicted to occur in a generic system consisting of a detector linearly coupled to an oscillator [11]. In that case, classical constructive and destructive interference effects in the response of the detector to the oscillator motion lead to a resonance (bunching) and anti-resonance (anti-bunching) in the detector noise. Other electromechanical effects such as feedback [10] and non-equilibrium phonons [58] have also been predicted to have a pronounced effect on noise, specifically leading to super-Poissonian correlations.

While further analysis is required for a complete explanation of the noise in our system, our work clearly shows that the interplay between electrical and mechanical degrees of freedom in the presence of backaction-mediated feedback can have a profound effect on electron-electron correlations, as has been predicted [10], [11].

Knowledge of the Fano factor $\mathcal{F}$ also allows comparison of the mechanical response expected from the piezoelectric mediated backaction to that calculated based on the noise power measurements in Section 2.8. To estimate the rms displacement *dy* expected from the backaction force, we first consider the response of a mechanical resonator with mass *m*, resonant frequency ω_m and quality factor Q_m to white force noise with spectral density S_F in N^2 per unit angular frequency. As shown with respect to equation 2.2, the mean square oscillator displacement $dy^2 = \langle y^2 \rangle$ is given by

$$dy^2 = \frac{S_F}{m^2 \omega_m{}^3} \frac{\pi Q_m}{2}.$$

We can also express the mean square displacement in terms of the mean square force dF^2 and hence charge fluctuation dn^2 within the bandwidth of the resonance using $dF^2 = (\omega_m / Q_m) S_F$, $dF = \eta\, dn$ and $k = \omega_m{}^2 m$ (see Section 2.3) to find

$$dy^2 = \frac{\pi}{2} Q_m{}^2 \frac{dF^2}{m^2 \omega_m{}^4} = \frac{\pi}{2} Q_m{}^2 \frac{dF^2}{k^2} = \frac{\pi}{2} Q_m{}^2 \frac{\eta^2}{k^2} dn^2.$$

On a characteristic mechanical time scale $t_0 = Q_m / f_m$ the mean square charge fluctuation is of the order

$$dn^2 \sim e\mathcal{F}It_0 .$$

Combining this with the above expression for *dy* gives

$$dy = \sqrt{\frac{\pi}{2}} Q_m \frac{\eta}{k} \sqrt{\frac{e\mathcal{F}IQ_m}{f_m}} ,$$

allowing us to estimate the rms displacement *dy* expected for a given current *I*.

For sample A an estimated rms charge fluctuation *dn* in a characteristic mechanical response time $t_0 = Q_m / f_a$ is given by $dn \sim \sqrt{\frac{e\mathcal{F}IQ_m}{f_0}} \approx 9{,}000e$ for *I* = 3 nA. Due to piezoelectric coupling, the charge fluctuations *dn* generate an rms displacement $dy = \sqrt{\frac{\pi}{2}} Q_m \frac{\eta}{m_a \omega_a^{\,2}} dn \approx 46$ nm. This is in good agreement with the value inferred from the reflected power measurement ≈ 50 nm. This means that the tunnelling of ~9000 electrons generates oscillations of the crystal ~ 46 nm.

In summary the electromechanical coupling in our system provides a fascinating example of classical dynamical behavior of a macroscopic object whose origins lie in fundamental quantum statistical fluctuations. The effect we observe is also a demonstration of the strength of the electric force and the dramatic impact it can have when a mesoscopic device generates charge imbalances in a macroscopic system. Given the tremendous disparity in masses, the effect of the tiny electrons striking the crystal and causing it to vibrate is analogous to a flea hitting Mt. Everest and causing meter scale vibrations in the mountain.

3 Electron Spin Resonance and Coherent Magnet Spin Rotations

3.1 Introduction

Originally proposed by Loss and DiVincenzo [59], the spins of electrons trapped in semiconductor quantum dots are an attractive candidate for quantum bits (qubits). The system is inherently scalable, is easily tunable via externally controlled parameters, and can be readily initialized [14]. Read-out in a double quantum dot (DQD) system can be accomplished via spin-to-charge conversion [60]. In addition the spin relaxation times T_1 are on the order of milliseconds [61],[62] and decoherence times T_2 as long as 200 μs have been achieved [63]. While weak coupling of spin with the environment enables the long T_1 and T_2 times, it also presents significant challenges related to the coherent manipulation of spin information.

One of the most direct mechanisms for achieving these coherent rotations is electron spin resonance (ESR) [64], [65]. In ESR a large constant external magnetic field B_{ext} is applied to a spin to create a Zeeman energy E_z splitting between the up and down S_z eigenstates. In addition a smaller transverse ac magnetic field B_{ac} is applied at the resonant frequency of the Zeeman splitting $f_z = E_z/h = \gamma_e B_{ext}/h$, where γ_e is the gyromagnetic ratio for the electron. By controlling the amplitude, phase, and duration of the ac magnetic field B_{ac}, it is possible to achieve arbitrary rotations including simple spin flips.

Two principal challenges in locally addressable ESR are: (1) the creation of a local field differential ΔB so that different dots have different resonant frequencies and (2) the generation of large ac magnetic fields B_{ac} that are not accompanied by significant ac electric fields E_{ac}. Part of my research efforts has been focused on a project to develop a system for ESR in which a lateral semiconductor double quantum dot is coupled to an externally generated ESR field. On chip ESR fields have previously been employed to perform ESR, but these systems have been challenged by an ill-defined electromagnetic environment. In particular, the presence of significant ac electric fields E_{ac} have caused sample heating and unwanted photon assisted transitions complicating the operation and interpretation of these ESR approaches [65]. Some current efforts have made progress in well defining spin manipulation with all electrical controls [60]. The strength of our system with the external generation of the ESR magnetic field is that we are able to carefully engineer the electromagnetic environment so that we can place the DQD sample at a peak in the magnetic fields B_{ac} and a node in the electric field E_{ac}.

This chapter reviews the physical set-up we employed for ESR manipulation, the Hamiltonian of this system, measurements enabled by our approach and the data we collected. The physical system discussion includes a review of the off sample stripeline, of the different sample geometries we employed and of the nano-magnets we used for the generation of a local field differential. The Hamiltonian discussion reviews the energetically accessible two electron singlet and triplet eigenstates and then explores how the energetics of the system can be used to appropriately manipulate the desired states. As our system is capable of arbitrary coherent spin manipulations, the enabled measurements include not only determinations of fundamental parameters such as T_1, T_2,

and T_2^* but also numerous significantly more involved explorations. The data presented includes a discussion of the results obtained and a review of the devices we measured and the constraints we encountered.

3.2 Physical System

The primary components of our physical set-up are: 1) the design and architecture of the stripeline and its integration with the DQD sample and 2) the various sample geometries that we employed to combine charge sensing, an on-chip matching network, the stripeline, and the nano-magnet.

As shown in Figure 3.1, our novel approach for generating a large ac magnetic field B_{ac} employs a stripline geometry (a narrow conductor with a width w separated by dielectric from upper and lower ground planes). A fundamental constraint on our system is limiting the external magnetic field $B_{ext} \approx 0.3$T to a regime where our rf-SET charge sensor remains superconducting. This sets our resonant frequency $f_{ac} = g^* \mu_B B_{ext} / h \approx$ 2Ghz. The stripline is chosen $\lambda_{ac}/2$ in length with one end terminated in an open circuit. Given the boundary conditions, a standing wave develops with a maximum in the ac magnetic field B_{ac} (and a node in E_{ac}) at a distance $\lambda/4$ from the end of the stripline. At this location we cut an electrically narrow slot and mechanically insert our mounted sample to make contact with the base of the stripline. According to our conformal mapping calculations, the stripline should generate a $B_{ac} \approx 1.5$ mT at a distance of 5 μm. This corresponds to a gating time $\tau_\pi \approx 50$ns, $T_{Rabi} = 2h/(g^* \mu_B B_{ac}) = 2\tau_\pi$.

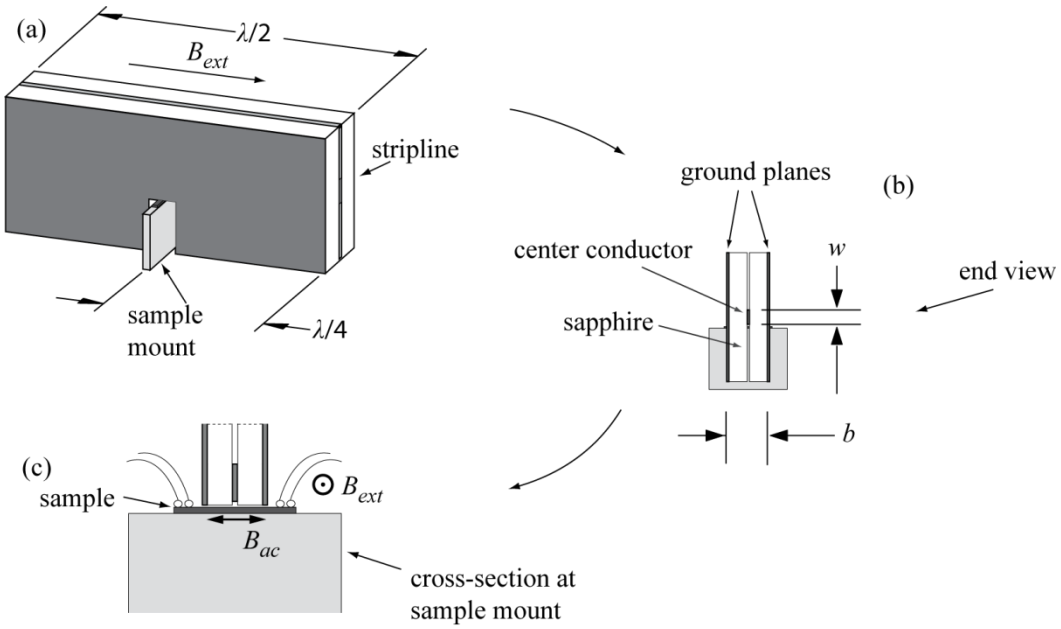

Figure 3.1 Schematic diagram of stripline geometry for generating an alternating magnetic field B_{ac} at the sample surface: (a) a perspective drawing of the stripline showing the electrically narrow slot at λ/4 where the sample is inserted, (b) an end-view highlighting the width *w* of the central conductor and the thickness *b* of the stripline, and (c) a magnified cross-sectional view at the location of the sample mount indicating the directions of B_{ext} and B_{ac} and the location of the sample wiring.

As detailed in Sections 4.3.3 and 4.3.4 in the experimental techniques chapter, bring the sample within 5 μm of the center conductor of the stripeline is a non-trivial experimental undertaking. This required a custom designed sapphire grinding apparatus and a specialized mounting apparatus. As part of our approach, we also developed specialized procedures that allowed us to achieve the tight physical tolerances.

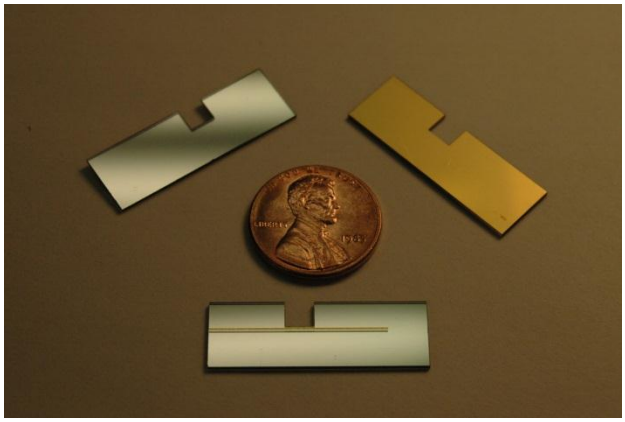

Figure 3.2 Images of the sapphire half stripelines with the electrically small notch that allows samples to be brought in close proximity to the central conductor. To form a stripeline, two stripeline halves are mated, each having an Au ground plane and one having a central conductor. The stripeline halves on the left and bottom of the image show the inside surfaces that are mated. As shown, the central conductor is placed on one of the halves. The stripeline half on the right shows the outer ground plane.

The final system that we used included an on-chip matching network, a charge sensor, and gate geometries allowing for the integration of the stripeline and the nanomagnet. Figure 3.3 shows the device geometry in which the integrated charge sensor is a superconducting SET. As shown, the device includes a standard DQD gate architecture in which the sickle shaped lower left and right gates function as plunger gates allowing for an adjustment of the chemical potential of the left and right dots. The use of the sickle gates for chemical potential adjustment allows for the elimination of separate plunger gates. This simplifies the design and increases device yield. The upper left and right gates are used to form tunnel barriers with the central gate as part of the dot formation. Unlike in earlier designs, the upper gates are separated from the lower sickle gates to facilitate fast manipulation of the dot potentials and to allow this manipulation to be independent of the voltages required for proper tunnel barrier formation. As discussed in Section 4.3.3, the alignment of the SET and the nanomagnet are experimentally

challenging steps that required the development of specialized procedures to achieve high yield.

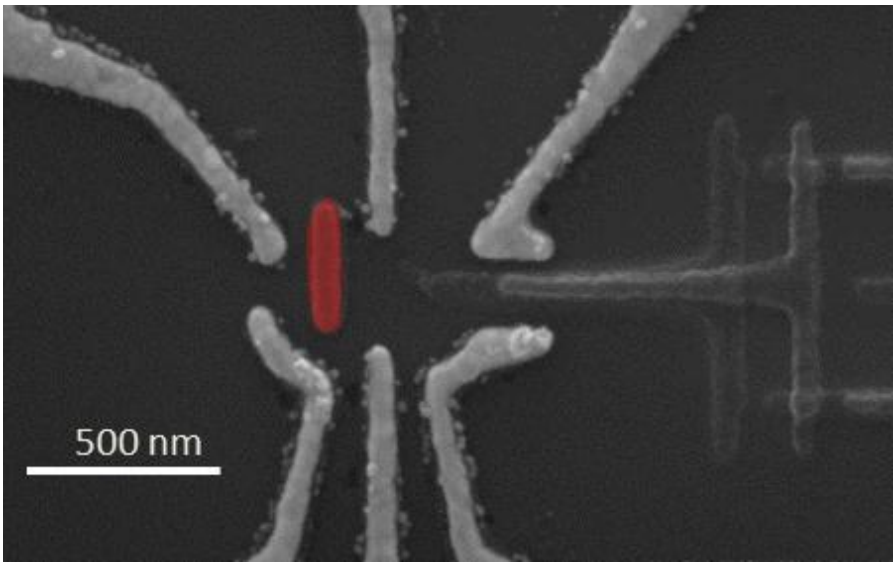

Figure 3.3 SEM image of DQD device similar to those measured with a nanomagnet (false color red) and an SET as a charge sensor.

To achieve the local field differential ΔB as shown in Figure 3.3, we fabricated a small (on the order of 200nm × 50nm × 50nm) permalloy (Fe:Ni 78:20) magnet above one of the QDs in a DQD. Using a finite-element modelling package (FEMLAB), we have estimated ΔB at 10-20mT at the 100nm depth of our 2DEG. This difference in Zeeman energies ΔE_z corresponds to a difference in resonance frequencies $\Delta f_z = \Delta E_z / h \approx$ 90 Mhz, which should be more than adequate for local resonant tuning.

3.3 System Hamiltonian

For our system we consider two electrons trapped in the double well potential of a DQD. In this analysis we confine ourselves to a bias regime where the possible dot occupancies are the electrons separated in different dots (1,1) or both confined to the

right dot (0,2). Prior to the perturbation introduced by the nanomagnet, the eigenstates of the system are the separated (1,1) triplet $|T_+\rangle_{11}, |T_-\rangle_{11}, |T_0\rangle_{11}$ and singlet $|S\rangle_{11}$ states as well as the (0,2) singlet state $|S\rangle_{02}$. Given the size of our dots, the (0,2) triplet states $|T\rangle_{02}$ lie ~ 100's μeV above the (0,2) singlet state $|S\rangle_{02}$ and are energetically inaccessible. Therefore, these states are not considered here. Including the perturbative effect of the nanomagnet δh and a tunnel coupling t between the singlet states $|S\rangle_{11}$ and $|S\rangle_{02}$, the Hamiltonian H_0 for our system is

$$
\begin{array}{ccccc}
|T_+\rangle_{11} & |T_-\rangle_{11} & |T_0\rangle_{11} & |S\rangle_{11} & |S\rangle_{02}
\end{array}
$$

$$
H_0 = \begin{pmatrix}
\Delta + \varepsilon_z & 0 & 0 & 0 & 0 \\
0 & \Delta - \varepsilon_z & 0 & 0 & 0 \\
0 & 0 & \Delta & -\delta h & 0 \\
0 & 0 & -\delta h & \Delta & -t \\
0 & 0 & 0 & -t & -\Delta
\end{pmatrix}
$$

where the detuning parameter $\Delta = (\mu_L - \mu_{RS})/2$ and μ_L is the chemical potential of the left dot and μ_{RS} is the chemical potential for placing a second electron in the right dot in the $|S\rangle_{02}$ state. The z-axis Zeeman term $\varepsilon_z = E_z + \delta h$ includes a component $E_z = -g^*\mu_B B_{ext} \approx 7\ \mu$eV for the external magnetic field and one $\delta h = -g^*\mu_B \Delta B/2 \approx 0.2\mu$eV for the nanomagnet field. Typical tunnelling couplings in GaAs are of the order t ~ 10's of μeV. The detuning parameter Δ adjusts the energetics of the system thereby controlling mixing between the original eigenstates and determining which states are energetically favorable. For example consider the new low energy eigenstate of the perturbed system $|\varphi_-\rangle$, which

will be discussed in more detail with respect to Figure 3.5. In the bias regime that we are considering, at least one electron is always present on the right dot. As shown in Figure 3.4 when the detuning parameter $\Delta = 0$, the chemical potentials of the left and right dots are equal and the system oscillates between the (1,1) and (0,2) charge states. When Δ is negative, the favoured charged state is (1,1), and, similarly, when Δ is positive, the favoured charged state becomes (0,2).

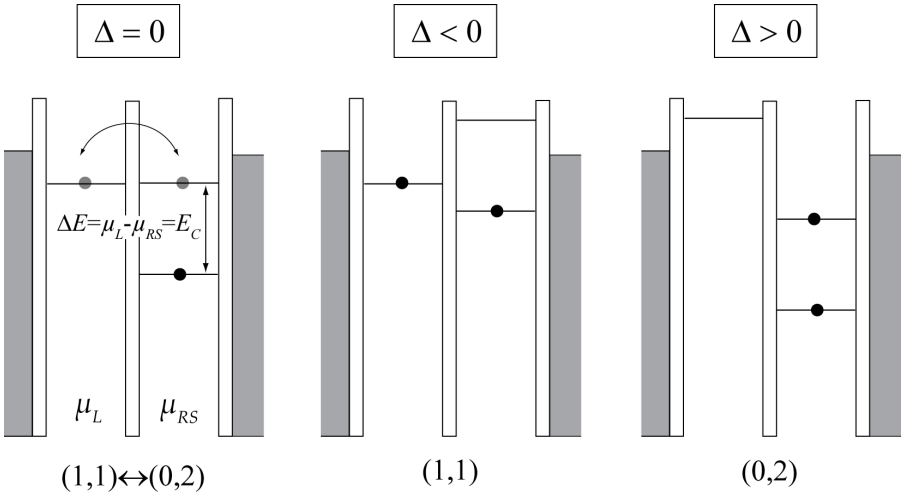

Figure 3.4 A schematic diagram of the charge states of a DQD corresponding to different values of the detuning parameter $\Delta = (\mu_L - \mu_{RS})/2$. In the bias regime considered, the right dot is always occupied with at least one electron. When the chemical potentials of the two dots are equal, the system oscillates between the (1,1) and (0,2) states. This corresponds to the chemical potential of the left dot μ_L being equal to the charging energy E_C of the right dot. When the $\mu_L < \mu_{RS}$, the system is in the (1,1) state and when $\mu_L > \mu_{RS}$, the system is in the (0,2) state.

The eigenenergies for the coupled perturbed system can be solved by diagonalizing the Hamiltonian H_0. As shown in Figure 3.5, the external field B_{ext} separates the energies of the parallel triplets $|T_+\rangle_{11}, |T_-\rangle_{11}$ which remain eigenstates of the system and only mix with the other states at discrete energy crossing points (circles). At small detuning values ($\Delta \leq t$), the states $|T_0\rangle_{11}, |S\rangle_{11}, |S\rangle_{02}$ strongly mix (yellow) and the

resulting eigenstates $|\varphi_-\rangle, |\varphi_0\rangle, |\varphi_+\rangle$ are labelled in order of increasing energy. Due to the presence of the nanomagnet at large detuning values ($|\Delta| \gg t$), the approximate eigenstates are given by $|T_+\rangle_{11}, |T_-\rangle_{11}, |\uparrow\downarrow\rangle_{11}, |\downarrow\uparrow\rangle_{11}, |S\rangle_{02}$. In this analysis the nanomagnet is placed on the right dot and is parallel to B_{ext} resulting in $|\uparrow\downarrow\rangle_{11}$ having a lower energy than $|\downarrow\uparrow\rangle_{11}$.

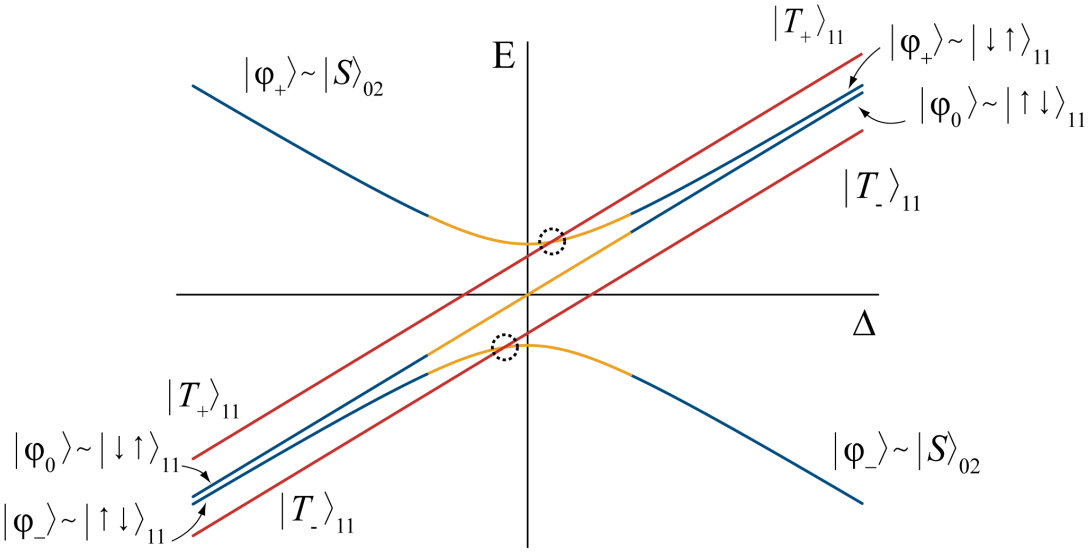

Figure 3.5 A schematic diagram of the eigenenergies of a DQD system with an integrated nanomagnet and an external magnetic field B_{ext} as a function of the detuning parameter $\Delta = (\mu_L - \mu_{RS})/2$. At small detuning ($\Delta \leq t$), the states $|T_0\rangle_{11}, |S\rangle_{11}, |S\rangle_{02}$ strongly mix (yellow lines). Circles highlight the points where mixing occurs between the triplet states $|T_+\rangle_{11}, |T_-\rangle_{11}$ and other states of the system.

It is useful to note that $|\uparrow\downarrow\rangle_{11} = \frac{1}{\sqrt{2}}(|T_0\rangle_{11} + |S\rangle_{11})$ and $|\downarrow\uparrow\rangle_{11} = \frac{1}{\sqrt{2}}(|T_0\rangle_{11} - |S\rangle_{11})$. This is especially relevant for read-out measurement schemes. As tunneling preserves the total

spin state, this means that there is a finite probability of either $\left|\uparrow\downarrow\right\rangle_{11}$ or $\left|\downarrow\uparrow\right\rangle_{11}$ tunneling to $\left|S\right\rangle_{02}$ when the detuning parameter Δ is swept from the (1,1) to the (0,2) state.

3.4 Prospective ESR Measurements

With the ability of our ESR set-up to coherently rotate addressable spins, we have a flexible platform for numerous experiments. The first order measurement is simply a demonstration of the proper operation of ESR in the system. The next series of measurements would likely include the relaxation time $T_{1,}$ the decoherence time $T_{2,}$ and the time-ensemble-average decoherence time T_2^* [66], all important phenomenological parameters regarding the coherent evolution for any ESR DQD system. In addition, with a tuneable ESR DQD system, we should be able to perform a partial Bell-state (parity) measurement on our two qubit system. This measurement is a central component in a proposed universal gate set based entirely on single qubit operations [67], [68]. In addition to simplifying potential implementations, such an approach would avoid the charge dephasing that is associated with the two-qubit operation of exchange based systems [60], [69], [70].

The demonstration of ESR in our system is based on the spin-to-charge conversion enabled by spin-blockade [60], [71]. As shown in Figure 3.6, spin blockade can be established by first tuning the DQD system so that a single electron is trapped in the right dot. The large spacing in the right dot's chemical potential levels corresponds to the charging energy E_C associated with placing both electrons on the right dot. When in the (0,2) state, both electrons are assumed to be in the same single particle ground state, and

the Pauli Exclusion Principle requires that the spins have opposite orientation. The smaller energy separations for the left dot correspond to the Zeeman splitting.

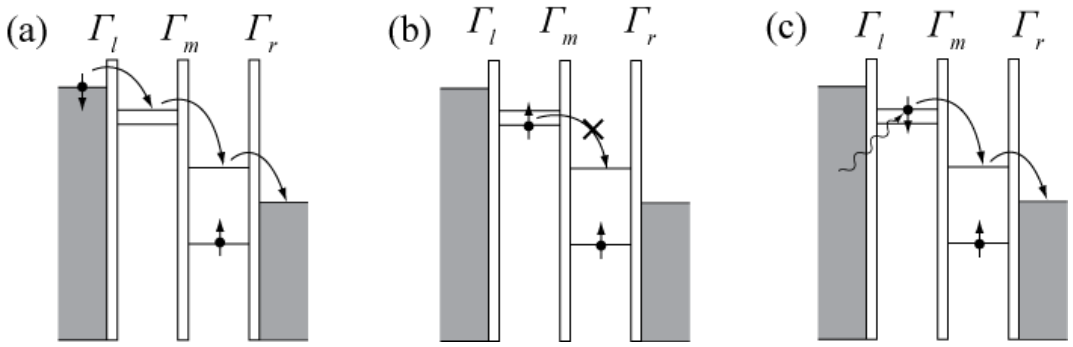

Figure 3.6 Transport through a DQD becomes spin blocked whenever the spins are aligned parallel. An ESR pulse resonant with the left dot lifts the spin blockade.

Transport through the dot occurs through the sequence (0,1)→(1,1)→(0,2)→(0,1). This sequence is enabled as long as the spin of the tunnelling electron differs from that of the trapped electron. Transport, however, becomes spin blocked whenever the spins are parallel. With an ESR pulse resonant on the left dot, spin-blocked electrons can be flipped thereby recommencing transport. If the tunnelling rate $\Gamma_r \ll \Gamma_m, \Gamma_l$, then the spin-flips will shift the average state of the DQD from (1,1) to (0,2), an easily detectable difference.

Central to spin manipulation measurements is the rapid initialization of the system. Referring to Figure 3.7, the system is first placed at the point *L* in the charge stability diagram. At the point *L*, the sequence $|T\rangle_{02} \rightarrow (0,1) \rightarrow |S\rangle_{02}$ is energetically favorable. This ensures that regardless of the initial (0,2) state the DQD will be in $|S\rangle_{02}$ with a high degree of probability after a time on the order of the $(0,2) \leftrightarrow (1,1)$ tunnelling time. The system is then ramped to the point *P*. Here the detuning Δ is large and

positive, and the state is $|\varphi_-\rangle \sim |S\rangle_{02}$. After a settling time ~200ns, the gates are slowly ramped to the point *C*. The ramping is long with respect to the slowest time scale of the system $h/\delta h \approx 20ns$. As this passage is adiabatic, the system should remain in the ground state which at the large negative detuning of the point *C* means that the state $|\phi_-\rangle \sim |\uparrow\downarrow\rangle_{11}$.

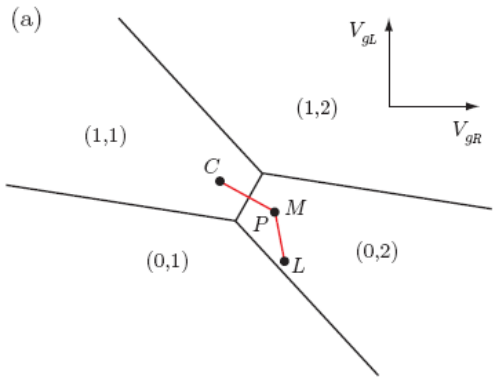

Figure 3.7 A DQD stability diagram showing the points used for initialization and read-out.

After initializing in the state $|\uparrow\downarrow\rangle_{11}$, a procedure to measure T_1 is to simply wait a period of time τ_1 before projecting onto the $|S\rangle_{02}$ state. This measurement step corresponds to sweeping the gates back to the point *M* at large positive detuning. If one of the spins has flipped thereby relaxing the system into $|T_+\rangle_{11}$, then the system will be blocked in the (1,1) state. Varying τ_1 will give a measure of T_1. A procedure for measuring T_2 is to use an ESR field to drive Rabi oscillations between, for example, the $|\uparrow\downarrow\rangle_{11}$ and $|T_+\rangle_{11}$ states. The period over which the oscillations decay should give a measure of T_2

The ability of ESR to achieve arbitrary coherent rotations is a powerful tool that should enable the exploration of an implementation of a Fermionic Bell State analyzer [67]. One of the most significant advantages of such an approach is that entirely magnetic control enables potentially long decoherence times T_2. Theoretically the intrinsic decoherence time of an isolated spin T_2 in a GaAs dot has been estimated as 1-50 μs [66], [72]. Experimentally the time-ensemble-average for a collection of spins T_2^*, which sets a lower bound on T_2, has been measured as on the order of 10-100 ns [60], [69]. Using a multiple-pulse Carr–Purcell–Meiboom–Gill echo sequence, a recent experiment extended the decoherence time to more than 200 μs [63]. These T_2^* times are based on singlet-triplet qubits which are inherently sensitive to charge fluctuation dephasing as their eigenstate energy separation is based on the electrically mediated exchange operation. In a system not dependent on the exchange interaction, control sequences to dynamically decouple electron spins from the nuclear spin reservoir might well be able to achieve longer T_2. With a gate operation $\tau_\pi \sim 50$ns, coherence times on the order of 500 μs would correspond to a $Q \sim 10^4$.

3.5 Data

The DQD samples we used to perform ESR measurements were complicated and required numerous fabrication and mounting steps, each with a yield less than unity (see Section 4.3). Despite being a significant challenge, careful dedicated work allowed us to reduce these risks to manageable levels. In all we were able to cool and take data from over fifteen samples. These samples included eleven DQDs with rf-QPCs as the charge sensor and four with rf-SSETs as the charge sensor, see Appendix Section 6.3. Given

their simpler structure, rf-QPC samples were included in part to increase our throughput and device yield. Our ultimate constraint in being able to perform ESR measurements, however, were issues of material performance and stability combined with the time intensive nature of the sample fabrication as well as other experimental challenges. The material and device issues included charge instability, noisy QPC charge sensing current and an unresolved weak electrostatic coupling of the SET to the dot charge and island gate.

In virtually all instances the presence of a 2DEG with an acceptable resistance required the introduction of carriers through illumination with an LED. To make this process as gentle as possible, our final approach to cooling down samples included current biasing the LED's in the range of ~ 1 μA, corresponding to a few μW's of power. As shown in Figure 3.9 with this gentle illumination technique, we were able to form reasonable dots with some samples.

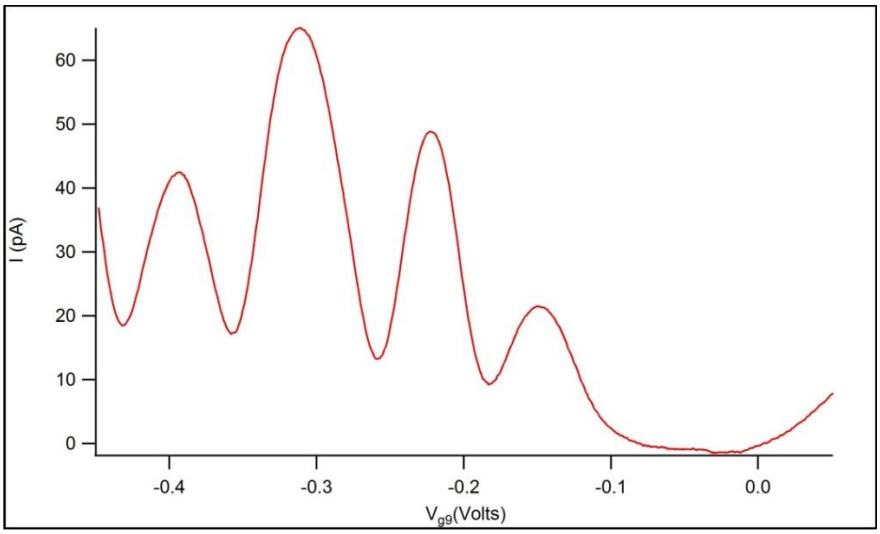

Figure 3.8 Coulomb oscillations corresponding to a single dot formed using the outer gates of a double quantum dot pattern. The charging energy E_C is computed from ΔV_g by the ratio $\eta = C_g/C \sim 0.1$, $E_C = e\eta\,\Delta V_g = (e^2/C_g)(C_g/C) \approx 15$ meV.

The low noise introduced by our measurement set-up is evidenced by the fact that the current data shown in Figure 3.8 was taken with a dc bias with the output signal being fed into a digital oscilloscope for monitoring. We used this simplified measurement approach when forming dots as monitoring the current in real time on the oscilloscope allowed us to explore the large parameter space associated with determining the appropriate gate voltages in a reasonable time frame.

The coulomb oscillations shown in Figure 3.8 were at times stable on the scale of minutes to hours. After periods of stability, however, the device performance frequently spontaneously transitioned to one in which charge hoping was pronounced. Such typical unstable behaviour is shown in Figure 3.9 in which the coulomb oscillations for two sequential voltage sweeps are recorded. The time from the beginning of the first sweep to the end of the second sweep was on the order of 10 minutes. As can be seen, there is a commonality in the oscillation structure at smaller gate voltages. At more negative voltages, however, the oscillations are noisy, not well formed and not repeatable.

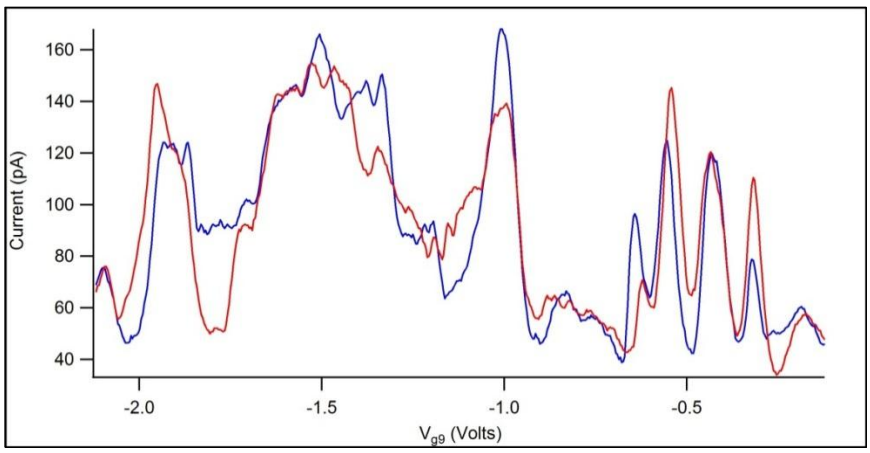

Figure 3.9 Typical coulomb oscillations for a sample displaying unstable behavior. The red and blue current traces were taken in succession with all the data having been collected in about 10 minutes

Once stable behaviour had been demonstrated for a particular dot, we would at times thermally cycle the sample to restore such behaviour if a disturbance or a particular cool down resulted in erratic performance. For one of our most promising samples, Sample 11, we performed a total of 6 runs. Ultimately noise in the QPC charge sensing current prevented operation in the few electron regime and at high frequency. Figure 3.10 shows correspondence between the dot coulomb oscillations and changes in the QPC current.

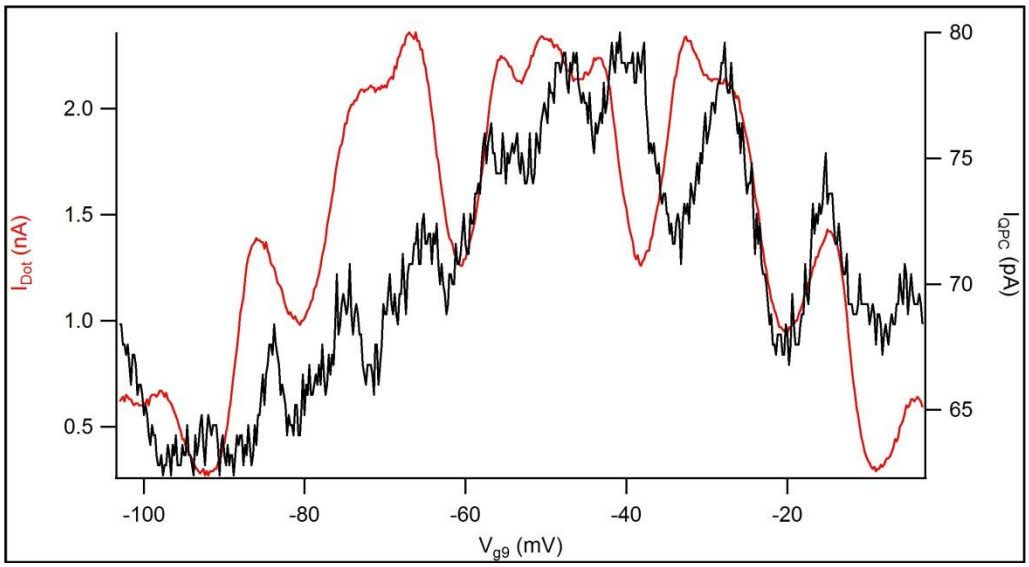

Figure 3.10 A plot of the dc currents through a dot and an adjacent charge sensing QPC showing a correspondence between the dot current's Coulomb oscillations and changes in the QPC current for Sample 11. Noise in the QPC current prevented its ac operation and its effective use as a charge sensor.

As can be seen, however, the QPC current is noisy. To investigate this we recorded the QPC current over time with no dot present and the filtering removed. When biased near a ½ plateau, the current showed random variations on the order of ~ 0.5 nA.

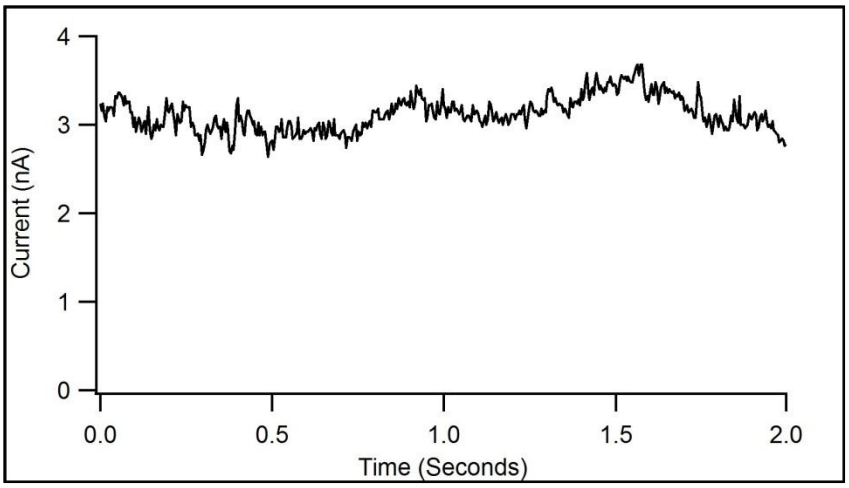

Figure 3.11 A record of the charge sensing QPC biased near ½ plateau as a function of time with no filtering and no dot formed for Sample 11.

To use a QPC as a charge sensor requires a relatively clean current signal in which the QPC is biased around a ½ plateau and changes in the differential conductance are recorded and correlated with changes in the local electromagnetic. The variations in QPC current shown in Figure 3.11 appear to be inherent to the sample and were too significant to allow its effective use as a charge sensor.

We have confidence in our overall measurement set-up as with pre-ESR samples we were able to effectively perform charge sensing with a QPC. For example the data shown in Figure 3.12 is from a DQD device that included both SET and QPC charge sensing. The data shows clear correspondence between changes in the QPC current and changes in the charge state of the dot. In particular the relatively clean QPC signal allowed the charge sensing to continue past the point where the dot tunnel barriers had become too opaque for a direct current measurement.

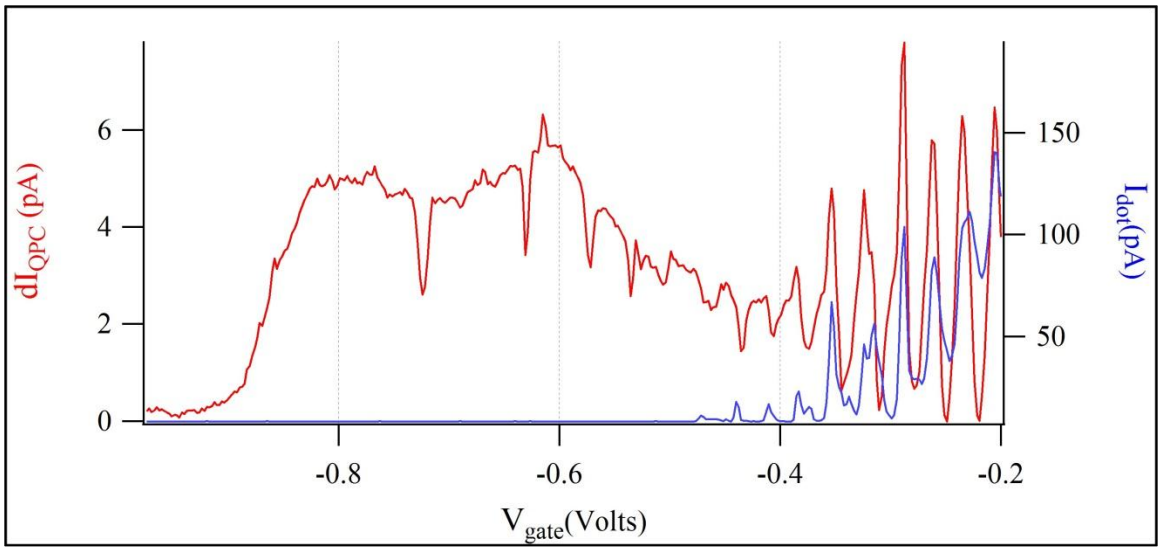

Figure 3.12 Charge sensing in a DQD using an adjacent QPC. Dips in the QPC differential current correlate with coulomb oscillations in the dc dot current. The charge sensing in the QPC continues past the point where the tunnel barriers are pinched off for a direct current measurement.

Figure 3.13 shows the promising performance of the rf-QPC for Sample 11. The best impedance matching, i.e., the lowest reflected power where $\Gamma \approx 0$, occurred when the QPC was biased around the second plateau. Subtracting off the 2.2 kΩ ohmic contact resistance, yields a channel resistance for best matching of 5.15 kΩ. Using equation 1.21

$$\omega_0 = \sqrt{\frac{1}{LC}}\sqrt{1-\frac{L/C}{R_d^2}}$$

and equation 1.22 with an assumption of perfect matching

$$Z = \frac{L}{CR_d} \approx 50\Omega$$

yields lumped parameter model values of $C = 428\,\text{pF}$ and $L = 110\,\text{nH}$ for a resonant frequency of $\omega_0 = 2\pi * 729\text{MHz}$.

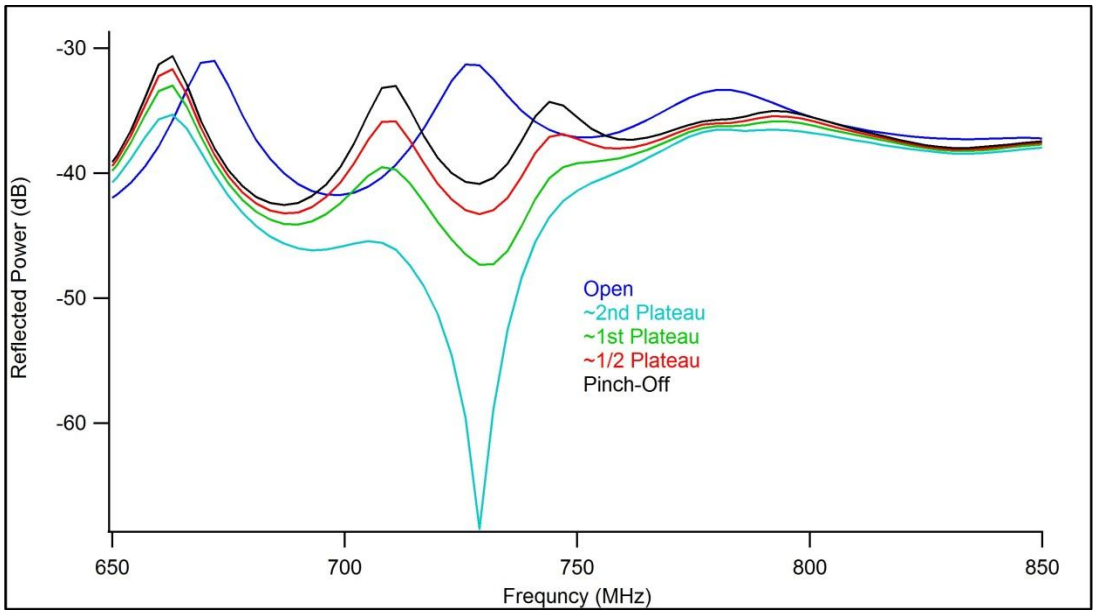

Figure 3.13 RF performance of the charge sensing QPC for Sample 11. The reflected power spectrum shows that the best impedance matching occurred when the QPC was biased around the second plateau.

Ideal operation of an rf-QPC corresponds to perfect matching when biased around ½ plateau where charge sensitivity is the greatest. This is approximately a five-fold increase in resistance relative to sample 11. Equation 1.22 requires a corresponding reduction in C or increase in L. To keep the resonant frequency within the 700MHz -1.2 GHz bandwidth of our HEMT cold amplifier, offsetting changes to both the capacitance and inductance would likely be the best approach. This should be experimentally achievable as the inductance can be increased with additional turns and for other samples, we have routinely had capacitances in the range of 100 to 150 nH.

As shown in Figure 3.14, we also formed dots in devices in which a superconducting SET was used as the charge sensor. As mentioned with respect to Sample 8, the Coulomb oscillation data shown in Figure 3.14 for Sample 9 was taken with a simplified set-up to facilitate the exploration of dot gate parameter space. The

current data and the ramp gate data are both plotted as a function of time mimicking the output plotted on the oscilloscope. At times as shown in Figure 3.14, Sample 9 displayed reasonably stable behaviour but overall charge fluctuations remained a problem with this sample.

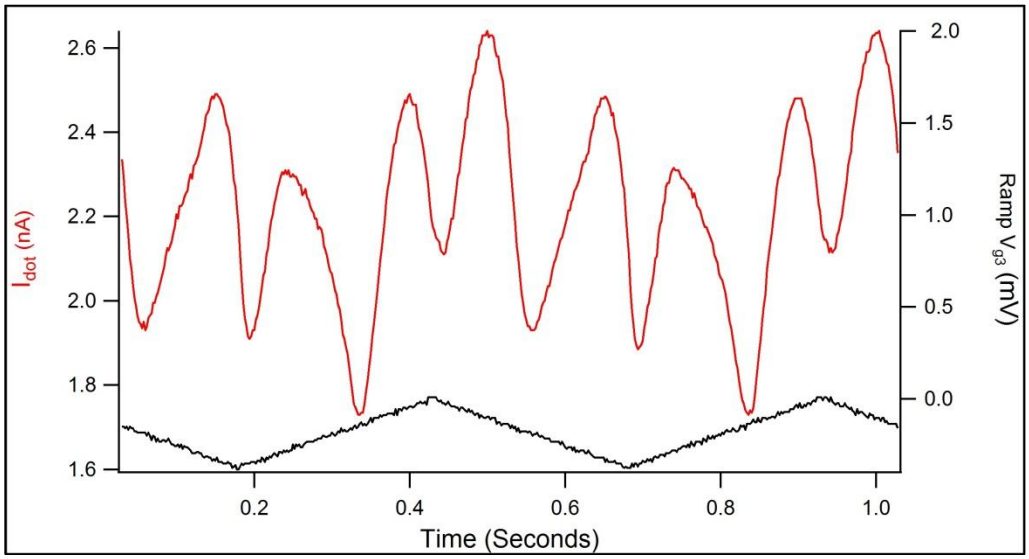

Figure 3.14 Coulomb oscillation data for Sample 9, a DQD device with an integrated RF-SSET as a charge sensor.

Figure 3.15 shows the I-V curve for the charge sensing SSET of Sample 9. The SSET is well formed showing the traditional sub-gap features including the central super current peak as well as the Double Josephson Quasi Particle (DJQP) and Josephson Quasi Particle (JQP) peaks [38], [42].

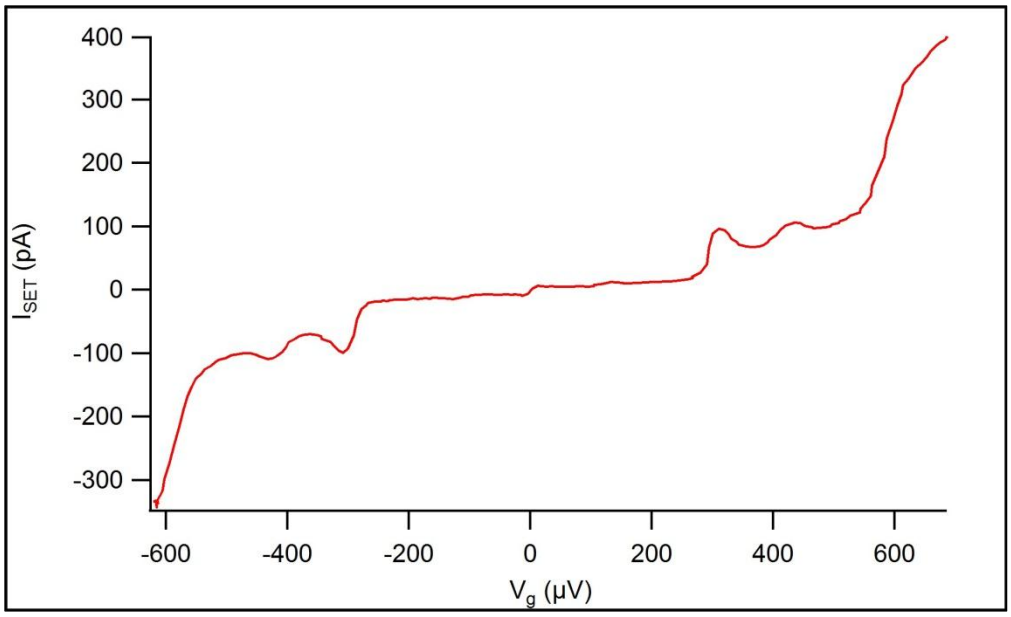

Figure 3.15 DQD integrated charge sensing SET I-V curve for Sample 9.

The unresolved problem for Sample 9 was poor coupling of the SSET to its electrostatic environment. For both Sample 9 and Sample 10, also an ESR rf-SSET device, it was not possible to modulate the current features of the SSET. In particular, neither SSET responded to voltages applied to the SSET island gate or to charge oscillations in the dot. Pre and post run optical and SEM investigation of the sample leads and device fine structure showed no evidence of breakage or systemic lithographic errors. The proper I-V behaviour of the SSET also argues against lithographic problems as the SSET leads, fabricated at the same time as the SSET island gate, were clearly continuous. The SSET island gate was 200 nm from the island, comparable to the distance of other SSETs routinely fabricated in the lab. One possible mechanism for the lack of SSET modulation is related to the shallow 57 nm depth of the 2DEG for the material used for Samples 10 and 11. It is proposed to explore this as the failure mechanism by fabricating a pair of SSETs on a piece of 2DEG material in which one

SSET is deposited on an etched surface and one on a pristine surface to evaluate differences in performance, especially with relation to modulation.

The final experimental challenge encountered was a helium cold leak in the inner vacuum can (IVC) of the Kelvinox 400 dilution refrigerator. Out of the final seven runs, four were terminated due to a cold helium leak. The suspected culprit is the IVC can itself. The container was partially crushed during its original shipment and was made operational by the Oxford technician hammering a cone wedge into the top opening to restore a nominally round shape. Given the potentially time consuming nature of resolving the IVC issue, such as ordering a new IVC can, it was decided to transition experimental operation of the recondensing cryostat to the cavity-SSET experiment while the cold leak was addressed.

In summary, the fabrication and mounting of the DQD ESR samples with on-chip matching network and integrated rf QPC or SSET charge sensor was time intensive and required meticulous work. Diligent effort, however, yielded numerous samples from which dot and rf data was collected. The ultimate limitation in terms of proceeding to ESR spin manipulation in the few electron regime was material stability and cryogenic challenges. As a continuation of the ESR project in the future, a strong candidate material is SiGe with a strain induced 2DEG. The material and device fabrication techniques for the SiGe material used in our lab have proceeded to the point were stable dots are regularly formed. In addition, the lack of a nuclear spin background eliminates one of the main decoherence mechanisms and offers the prospect for potential longer coherence times, a crucial metric for any spin based information processing system.

4 Experimental Techniques

4.1 RF-QPC Device Details

The QPC samples were produced from GaAs/AlGaAs heterostructure material containing a two-dimensional electron gas with sheet density n_s = 1.3 x 10^{11} cm^{-2} and mobility $\mu = 3\times10^6 \text{cm}^2/\text{V s}$ at a depth of 100 nm below the crystal surface. The 2DEG material was supplied by Loren Pfeiffer of Princeton University and identified by 3-30_05.2. Annealed ohmic contacts were either pressed In (sample A) or thin film Ni/Au/Ge alloys (all other samples) with typical lateral dimensions on the order of 100 µm. A mesa was etched to remove the 2DEG from most of the surface, except for the ohmic contacts and a relatively narrow channel (typically a few hundred microns wide) where the QPC was formed. Au surface Schottky gates for defining the QPC were patterned using standard electron beam lithography techniques and thermal evaporation. Sample geometries presented in Figure 2.8 and Figure 2.9 were measured by optical microscopy giving l_a = 2.83 mm and w_a = 2.10 mm for sample A, l_b = 1.47 mm and w_b = 1.58 mm for sample B and l_c = 1.87 mm and w_c = 1.93 mm for sample C. All samples had a height h = 0.5 mm. Based on the sample geometries, the sample masses are estimated as A, (B), [C] as $m \approx$ 16, (6.2), [9.2] mg. Given the molar mass of GaAs, this corresponds to a total of $1.3\times10^{20}, (5\times10^{19}), [8.1\times10^{19}]$ atoms. For electrical measurements, samples were secured to a printed circuit board mount using rubber cement.

As discussed in Section 2.6, two perpendicular QPCs were used to evaluate the existence of the feedback loop. The device pattern used for this part of the experiment underwent a few iterations. The first pattern consisted of the two perpendicular QPCs being formed around the top and side of the same point on the sample. This pattern failed to function effectively as the positive bias used during cool down for each QPC interfered with the conductance through the other. The final pattern consisted of several QPCs for each direction to allow for material variations. In addition the parallel QPCs and the perpendicular QPCs were displaced from each other by several microns to ensure that the positive bias used during the cool down and any residual 2DEG shadow from the gates after being energized did not interfere with the operation of the other set of gates.

The rf-QPC data also suggests that there is some material dependence in the performance of the piezoelectric feedback loop. This is not surprising given the complicated and specific nature of the GaAs/AlGaAs heterostructures used to form 2DEGs. Material from Vladimir Umansky's group at the Technicon in Israel was also used during the rf-QPC experiment. As shown in Figure 4.1 and Figure 4.2 material from the batch 8-271 yielded well-formed stable QPC plateaus but the rf data displayed additional features that were not easily interpreted. The data did, however, show proper partition dependence and power scaling, i.e., $\sim P_{in}^{1/2}$. With samples from the 8-145 batch, it was difficult to form conductance plateaus and the rf data did not show clear partition dependence.

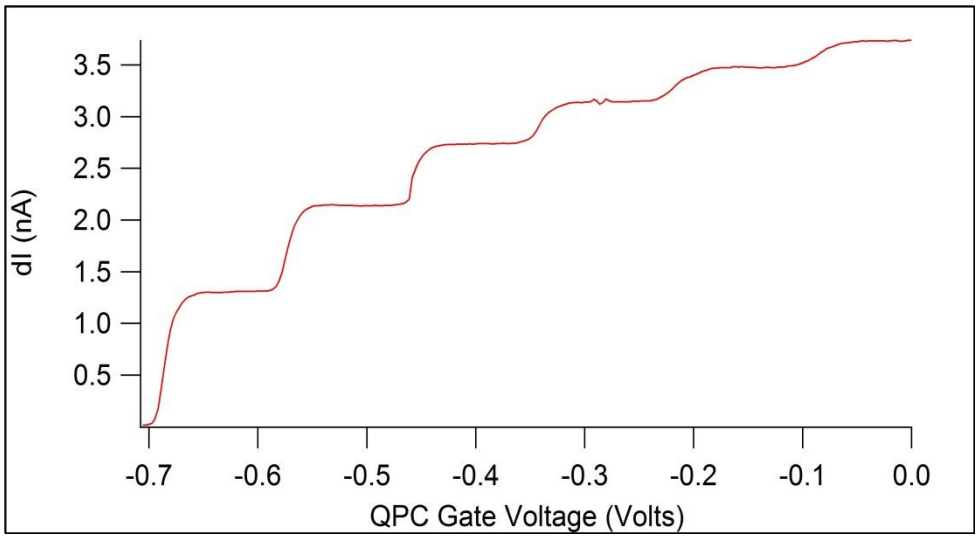

Figure 4.1 QPC differential current data showing well-formed plateaus for a device generated with Umansky material from the batch 8-271.

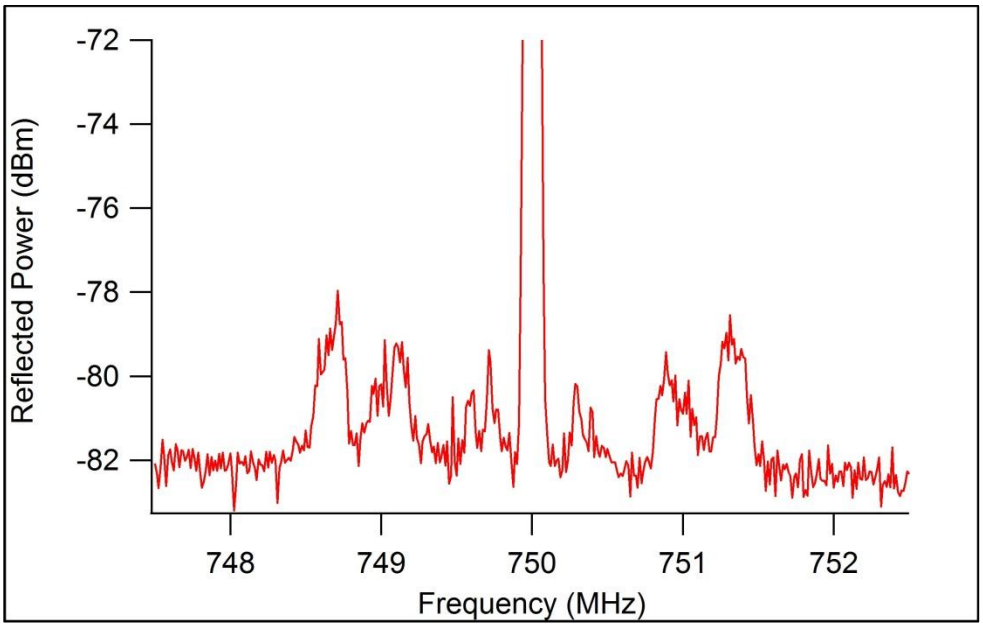

Figure 4.2 RF data from a QPC formed with Umansky material from the batch 8-271 showing additional features not easily interpreted.

4.2 RF-QPC Measurement Set-Up

As part of our QPC data collection, we used both a Kelvinox 100 dilution refrigerator with a base temperature of $T \approx 25$ mK and an effective electron temperature $T_e \approx 80$ mK (rf-QPC Samples A and B) and a Heliox pulse-tube cooled ^{3}He refrigerator with a base temperature $T \approx 290$ mK (sample C). The dc lines pass through cascaded π-type, microwave filters, and RC filters. On the Kelvinox 100 [^{3}He cryostat], there are copper powder [copper and stainless steel powder] microwave filters. The input rf lines have approximately 48 dB [35dB] of attenuation to filter incoming broadband radiation from room temperature. The input rf signal is fed to the sample by a directional coupler and then combined with the dc signals by a commercial 100kHz – 18 GHz bias-tee (Paterneck 1406).

Signals reflected from the sample pass through the main line of the directional coupler and then a circulator. To minimize initial signal loss, the rf cabling from the sample to the circulator is superconducting Nb (except in the case of sample A). The circulator serves to isolate the sample from noise sources on the output line. After the circulator, the output line includes a QuinStar cryogenic HEMT amplifier (Gain = 35 dB [26 dB]) with a noise temperature of 2.3K [9.5K] followed by a Miteq GaAs FET amplifier (Gain = 40 dB [38 dB]) at room temperature.

The complete dc and low frequency measurement set-up employed for samples B and C is shown in Figure 4.3. The heart of the measurement set-up is an ultra-low noise current amplifier that is wired in a floating configuration. Most of the electrical components including the ultra-low noise current and voltage amplifiers, the precision

voltage references, and the optical isolators were built by members of the lab based on original designs by Alex Rimberg. The measurement set-up for sample A is similar with a different configuration for the grounding of the current amplifier. This configuration is fully described in the thesis by Madhu Thalakulum [41], a 2007 graduate of the Rimberg Lab.

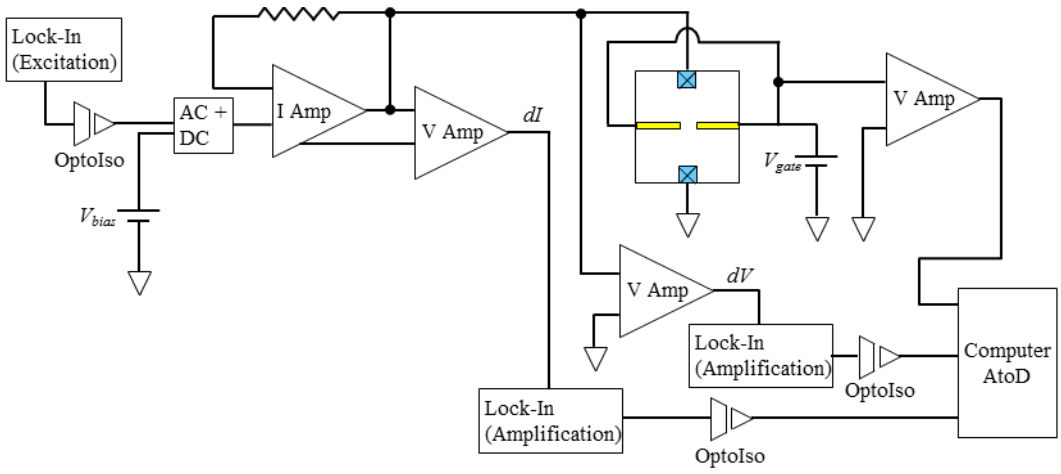

Figure 4.3 Complete dc measurement set-up for rf-QPC samples B and C. A simplified set-up in which the differential excitation voltage *dV* was not measured directly was frequently employed.

In measuring the conductance of the QPC as shown in Figure 4.3, the ac bias excitation was taken as the output from a Stanford Research Systems RS-830 lock-in amplifier. To isolate the sample from the ground of the lock-in, the excitation was passed through an optoisolator. This ac signal was then combined with the dc bias in a coupling divider box [21] that reduced the ac signal by a factor of 10^5 and the dc signal by 10^3. The ac + dc bias was feed into the non-inverting input of the current amplifier which through the virtual internal short placed the bias on the inverting input which was connected to the sample. In floating configuration, the (+) output of the current amplifier

was taken relative to the (−) output of the internal board ground. This differential signal was converted to a single ended one by a voltage amplifier set to a unity gain. The ac current signal was then fed into a RS-830 lock-in whose ground was again isolated by an optoisolator before being passed to the analog-to-digital converter of the computer data acquisition board.

In the complete measurement set-up the, ac voltage bias signal is directly measured from the sample and feed into a voltage amplifier, a lock-in and then the computer. As the ac voltage bias was found to be well maintained at the 20 μV value nominally applied after the coupling divider, direct measurement of the ac bias was eliminated in a simplified measurement set-up employed in some instances. As with the dc component of the bias voltage, the gate voltage was set with a precision voltage reference. This signal was sent to a voltage amplifier and passed to the computer. This configuration for setting the gate voltage was used when the QPC conductance needed to be carefully set and maintained, such as when the rf signal was measured at various conductance values to determine power and partition dependence. When the overall performance of the QPC was characterized by measuring the conductance plateaus, the voltage reference was replaced with a voltage sweep box. In addition when modulation of the QPC gate was required an ac voltage source was added was to the line.

4.3 General Fabrication with Details Specific to the DQD ESR Samples Including Mounting and Stripeline Alignment

The fabrication and mounting procedures for the DQD ESR samples with on chip matching network and integrated rf charge sensor were complex requiring a methodical

approach. Given the device configuration required for integration with the off-chip stripeline, only one device could be located on each chip. Even when the procedures were fully tuned and working properly, device fabrication required two to three weeks of intensive effort for each sample. To maximize throughput and yield, we employed dummy testing for sensitive steps and parallel processing of at least two real samples for each fabrication run. Device preparation included fabrication, wire bonding, stripeline alignment, and mounting to the fridge.

4.3.1 Device Fabrication

A fabrication run began with the careful cleaving of a new chip from the original wafer. The generation of a device then included six separate lithographic and metallization stages: alignment marks, etch, ohmic contacts, large gates, dot fine structures, nanomagnet, inductor, and SET, when present.

To minimize the scratching that was introduced by repeated cleaving of the wafer as new samples were prepared, we covered the entire original waver with a protective layer of resist spun on at low speed, ~1,000 rpm, and baked at a low temperature, ~100 - 150 °C. Prior to applying the protective resist layer to remove native oxide which can inhibit the formation of good ohmic contacts, we dipped the wafers in a surface refreshment solution of HCL:H_20::50:50 for 20 seconds. The procedure that I adopted for the careful cleaving of the wafers included: making a small scratch on the outer edge of the top surface of the chip, removing particulate remnants with a spray of IPA, inverting the chip and placing the chip on two pieces of cleanroom lint free tissue so that the scratched section of the chip was suspended between them with a few millimeter gap

on each side. I then pressed down gently on the backside of the chip directly over the scratch with the end of a pair of tweezers that had been wrapped in a tissue sheet to provide a cushioning effect. If the chip did not easily cleave, I introduced a slightly deeper scratch and repeated the subsequent steps. I found that effective cleaving was best achieved by repeatedly scratching until gentle pressure fractured the chip as opposed to exerting forceful pressure initially to induce a crack.

To eliminate potential current leakage paths and to improve high frequency performance, the 2DEG was removed from all parts of the sample except for those required for dot formation and current measurements. Based on the suggestion and investigation of Mustafa Bal, we replaced the lab's traditional citric acid etch with a phosphoric acid etch that had a more consistent etch rate through the different heterostructure layers and resulted in a smoother surface and cleaner interface. After experimentation, the concentration that we employed was H_3PO_4:H_2O_2: H_2O::1:1:204. Over a range of times, this yielded an etch rate of approximately 4.3 nm/s. The etch solution temperature 21.3 °C. The etch step was preceded by oxygen RIE descumming at 100 mT and 25 watts and followed by an IPA rise for 10 seconds.

For different samples, optimization of the ohmic annealing recipe was required to account for the different material composition and 2DEG depth. This was easily done by preparing one or more small sample pieces with simple ohmic patterns and progressively annealing and testing the ohmic resistance. The annealing was done in an enclosure built by Alex Rimberg that has a sealed top, inlet and outlet ports for the controlled flow of gas, and a resistance heated sample space driven by a Variac voltage control. The sample

space has an attached thermocouple for precise temperature monitoring. The lab has a probe station that includes fine adjustment in *x* and *z* that in combination with the long focal length Meiji microscope allows for the resistance of samples to be checked in a straight-forward manner.

Although we were careful not to waste material, we made sure to use good representative material from the center of a wafer for the ohmic testing as edge material had been found to have poor and inconsistent properties. In addition, even with the testing, we made sure to check the ohmic resistance for each real sample to avoid the commitment of significant time resources on an errant faulty piece. The probing of the real samples was done with considerable care so as to avoid damaging the surface.

As part of fabrication of the dots and the SETs, we employed standard lithographic and metallization techniques that are well described elsewhere. For example see theses from this lab by Weiwei Xue [42], Madhu Thalakulum [41] and Wei Lu [40]. The system we employed was a FEI XL-30 ESEM-FEG (field emission gun environmental scanning electron microscope) with Nabitity's Nano Pattern Generation System (NPGS) lithographic software. The director of Dartmouth's Electron Microscope Facility is Dr. Charles Daghlian who was a tremendous asset to our research efforts by maintaining the facility, despite extensive and varied use, in excellent operating condition.

The alignment of the nanomagnet and the SET finger for coupling to the dot were two of the most sensitive lithographic steps in the fabrication process. Crucial in the success that we achieved was a procedure developed by Mustafa Bal that reduced the alignment variation from 30-50 nanometers to remarkably less than 10 nanometers for the

nanomagnet and 10 – 30 nanometers for the SET finger. Figure 4.4 shows a dummy device with an integrated nanomagnet over the left dot and SET finger entering the right dot.

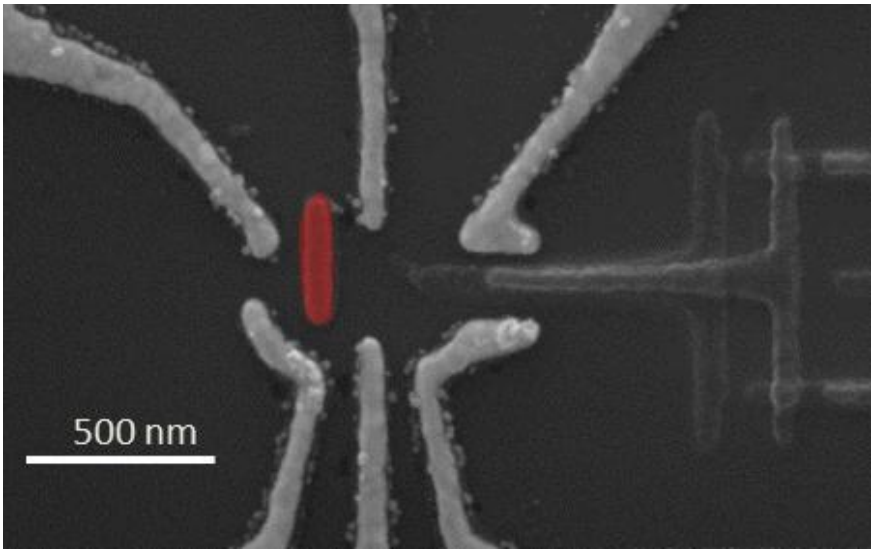

Figure 4.4 SEM image of dummy DQD device with nanomagnet (false color red) and SET, each deposited during separate lithographic steps. The alignment accuracy of the separate lithographic steps was on the order of 10-30 nm. The surface particles attached to the gates are resist remnants that accumulated due to the repeated processing and storage of the dummy array. This is the same image as Figure 3.3, reproduced here for convenience.

By reducing the alignment variation, we were able to decrease the separation between the gate electrodes. The top middle (TM) and top left (TL) gates were used to form the QPC tunnel barrier that separated the double dot from the electron source reservoir. It was important the TM and TL electrodes were close enough that the QPC properly formed before the dot became depleted by the application of the negative gate voltages. Similarly, the separation between the top right (TR) and lower right (LR) gates for the SET coupling finger between had to be narrow enough that the conduction channel underneath the finger was completely pinched off by the voltages applied as part of

normal dot formation. Prior to using the improved alignment procedure, we had attempted to couple the SET to the dot by first placing a finger over the dot as part of the dot lithographic step. As shown in Figure 4.5, the finger had an extended overlap region, that was used to couple to the SET.

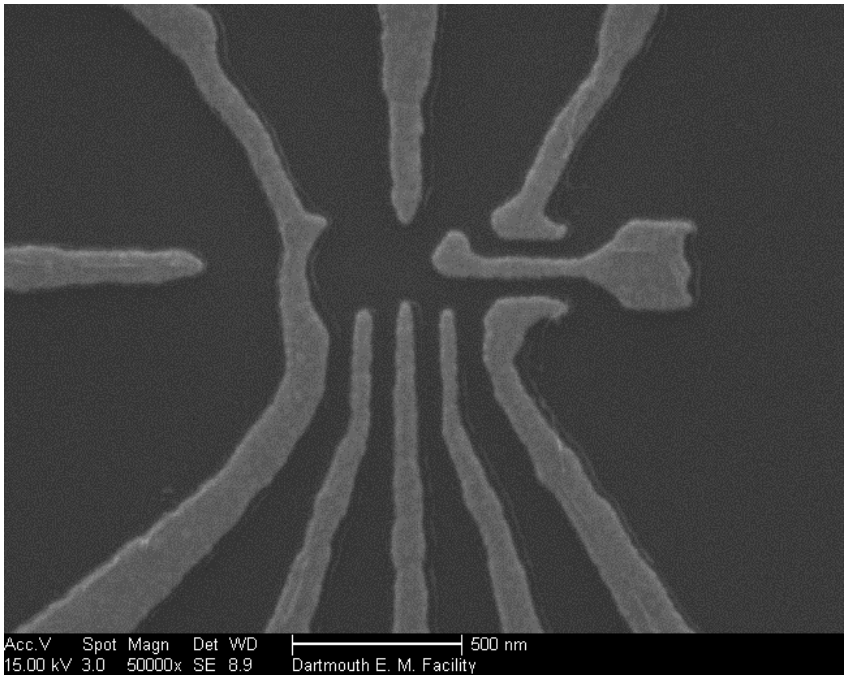

Figure 4.5 SEM image of dummy DQD device of earlier gate iteration in which coupling between the SET and the DQD employed a finger patterned with the dot gates. The finger included an extended overlap region to address the challenge of achieving metallic contact between submicron regions deposited during separate dot and SET lithographic steps.

This approach proved challenging as getting good metallic contact in the overlap region was not easy as SET junction size constraints severely limited the amount of RIE descumming that could be employed.

The essence of Dr. Bal's improved alignment procedure was to use physical movements of the SEM sample stage to achieve as much alignment as possible before

employing the NPGS matrix software routine. The procedure used the NPGS alignment windows that are opened initially when the alignment program is run. By shifting the alignment overlay patterns, the stage shift required could be determined. For stage shifts less than a micron, repeated attempts were usually required before a displacement of the appropriate amount was achieved. The displacements were executed by entering the desired location into the SEM stage control program and using the software to execute the stage movement. With the external manual stage adjustment knobs, stage movements on the order of ~ 1 micron were the practical limit of accuracy. With patience and repeated effort, it was possible to mechanically align the alignment marks within 100 nm of their required position with the stage control program. For the remaining fine alignment and any rotation required, the standard NPGS matrix alignment procedure was employed.

4.3.2 Wire Bonding

Successful wire bonding required that the bonder be in good working order. Most important with respect to this was that the tip be fresh and properly adjusted. For different sample materials, different operational parameters, as recorded in the bonding log book, were identified. The most sensitive bonding step involved connecting to the center of the spiral chip inductor. Given the limited size and the metallic thin film fracturing that occurs with a failed bond, usually only one or two bond attempts were possible. If the second bond failed, an alternative method employing indium was used.

The indium method used the mechanical action of the bonder in effectively manipulating pieces of indium on the order 100 μm or less. The preparation steps

involved in the indium procedure were: 1) inserting an old tip that had been dedicated for use with indium, 2) preparing a fresh piece of indium by cutting away with a clean x-acto knife the outer oxidized surface, 3) kneading the indium on a glass slide to make it pliable and sticky, and 4) attaching an inverted x-acto blade for indium manipulation in the bonder microscope's field of view. To attach a dangling failed wire bond, I would first use the inverted x-acto blade and the bonder indium tip to isolate a piece of indium ~ ¼ the size of the central inductor bonding pad. Next I would attach this piece to the central pad by repeatedly dabbing it on the surface. This would slowly build of remnants of indium on the surface which at some point would be adequate so that the indium blob would stick to the surface. It was important for the success of this step that the indium be barely attached to tip to facilitate its transition to the sample surface. I would then use the bonder tip to gently press the dangling failed bond into the indium blob. Once the wire was stuck to the surface, I would use the bonder tip to gently bring in another indium piece to sandwich the wire. The final step required care in that if the indium was too attached to the tip it could end up pulling off the first piece and the wire. Gentle dabbing with a barely attached piece of indium was again the preferred method.

4.3.3 Sapphire Stripeline Grinding

Maximizing the magnitude of the ac magnetic field placed a premium on bring the sample as close to the center conductor of the stripeline as possible. As shown in Figure 4.6(a), fabrication limitations meant that outer edge in the sample notch of the stripelines that we received from the contracted manufacturer were rough and ~ 130 μm away from the edge of the center conductor. To address this, we developed a technique to

controllably remove material that produced a smooth edge that was a few microns from the center conductor. The stripelines after processing are shown in Figure 4.6(b).

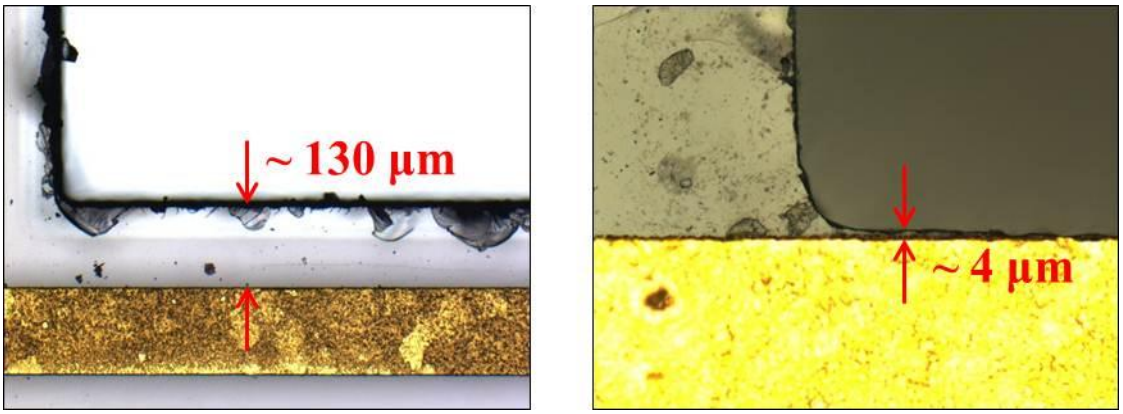

Figure 4.6 (a) Optical image of the details of the outer edge of the electrically narrow notch cut in the stripeline to allow the samples to be brought in close proximity to the central conductor. Given fabrication limitations by the contracted manufacturer, the stripelines received had a rough outer edge that was ~ 130 µm from the central conductor. (b) Optical image of a stripeline after a grinding procedure was used to smooth the notch edge and bring the outer edge within a few microns of the center conductor.

The overall set-up used in the procedure is shown in Figure 4.7. The set-up was based on the modification of a South Bay Technology diamond wheel saw. In particular

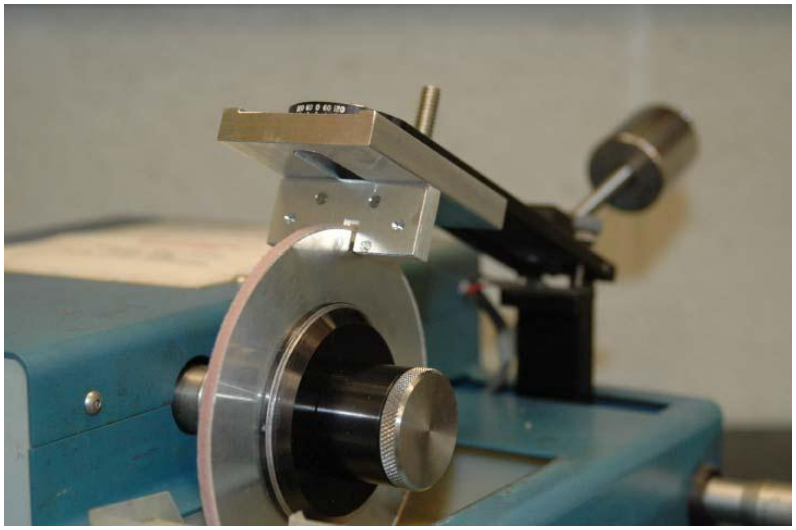

Figure 4.7 Set-up used to grind excess sapphire material from the sample notch in ESR stripelines. The set-up includes a grinding wheel specifically machined to have a thickness just under the notch width. The two stripelines halves are securely mounted in

a holder. In operation, the spinning grinding wheel's lower edge dips into 7 μm diamond slurry.

the thin diamond saw was replaced with a grinding disk that was machined to have a thickness a few hundred microns thinner than the stripeline notch. The lower edge of the grinding wheel sat in a 7 μm diamond slurry so that when spinning the grinding interface between the stripeline and the wheel was constantly refreshed with slurry. Two stripeline halves were mated and securely mounted in the holder. Figure 4.8 shows one of the

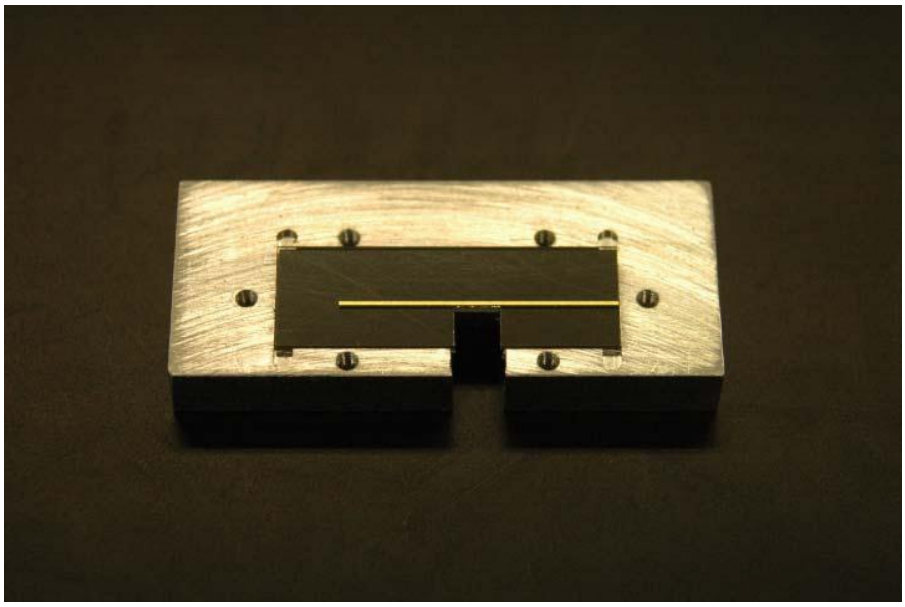

Figure 4.8 The stripeline holder with one stripeline half. For grinding, the second stripline half is carefully mated and secured with an outer tissue buffer and a cover plate.

stripeline halves in the holder before mating and being secured with a cover plate. To protect the Au outer ground planes and provide some cushioning, clean room tissues were used as an outer barrier layer. The position of the stripeline holder could be adjusted up and down the holder balance arm to ensure that grinding commenced in the middle of the stripeline; that is symmetrically between the Au ground planes. The grinding pressure could be finely tuned with a screw adjustable counter balance.

Once mated, it was not possible to see the central conductor. Therefore, before joining the halves, optical measurements were used to determine the amount of material to be removed. A small scratch was then made in the outer Au ground plane as a reference mark and the amount of material removed determined with respect to this mark. During grinding the stripeline holder was periodically removed from the grinding apparatus and measurements with the optical microscope were performed. Because precisely remating the stripeline halves was a time consuming process, optical inspection of the sapphire edge relative to the central conductor was only done to carefully control the removal of the final 5 – 10 μm of material. The South Bay Technology slurry had a suspension of diamond particles with a maximum diameter on the order of 7 um. As can be seen in Figure 4.6(b), this resulted in an unavoidable surface roughness on the order of a few microns. Grinding with a slurry having a finer suspension was not found to be effective as the grinding rate varied considerably. This made it difficult to properly terminate grinding within a few microns of the central conductor as grinding time was necessarily used as a metric for the amount of material to be removed.

4.3.4 Aligning the Sample

To get the maximum ac magnetic field at the sample it was important to precisely align the center of the stripeline with the sample. This alignment included both vertical and lateral alignment. The lateral alignment was achieved via mechanical adjustment relative to reference marks and the vertical alignment was achieved via grinding.

The stripeline holder was secured to the sample tail with two fine screw adjustable non-magnetic stages capable of submicron displacement. One stage provided for vertical

adjustment of the stripeline perpendicular to the sample surface and the other provided for lateral adjustment parallel to the sample surface. The objective of the lateral adjustment was to place the center conductor directly over the dot. The first step in this involved lithographically patterning reference marks symmetrically on opposite sides of the dot at a distance where the outer edges of the stripeline should line up. These reference marks are the short vertical Au lines in the middle of Figure 4.9. Once the stripeline was in place over the sample, the lateral stage was used to move the sample until the outer edges of the stripeline matched the reference marks.

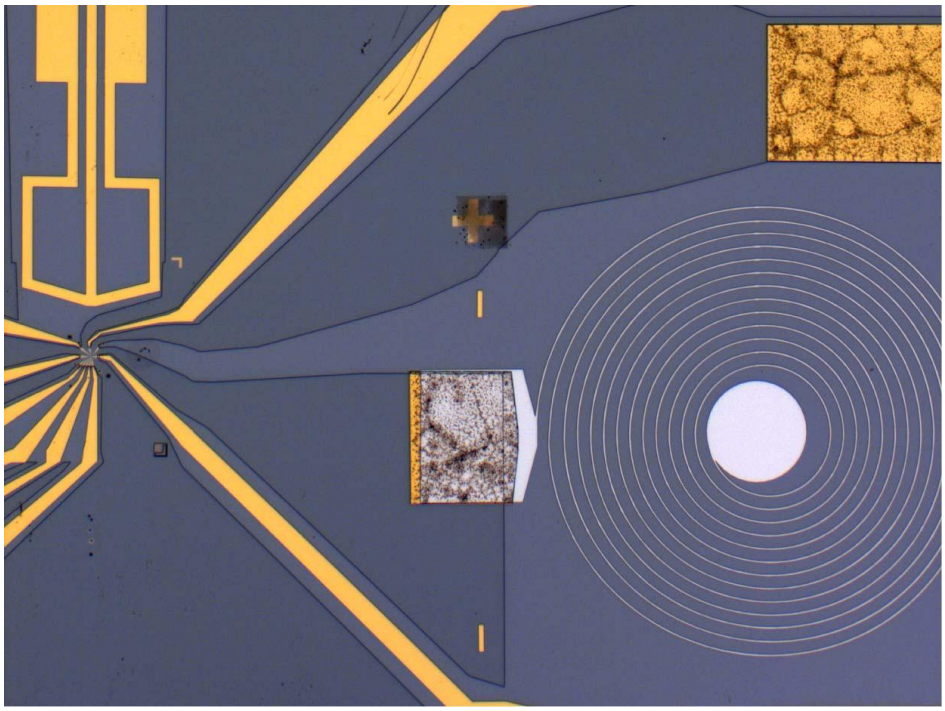

Figure 4.9 Optical image of the central portion of an rf-QPC sample showing the leads to the DQD device, a lateral alignment pick-up loop, alignment hash marks, and the on-chip spiral loop inductor.

As the sample mount set-up required that the lateral alignment with the Meiji optical microscope be done at oblique angle, determining a correspondence between the outer

stripeline edge and the reference mark proved challenging. To address this, later lateral alignment patterns had a series of marks. Symmetrically aligning these marks with their reflections on the sample surface ultimately provided the most accurate means of laterally aligning the sample. Also as shown in Figure 4.9, an initial method contemplated for use in the lateral alignment of the stripeline was the use of an rf pick-up loop. This method was not ultimately employed as it was determined that optical alignment could achieve the desired accuracy and removing the pick-up loop simplified the lithography and the rf connections to the sample.

As described in the previous Section 4.3.3, it was necessary to remove sapphire from the sample notch to bring the central conductor as close to the edge of the sapphire as possible. It was determined that this grinding could also be used to achieve vertical alignment. In as shown in the Figure 4.6(b), the natural rounding of the outer edges of the grinding wheel meant that corners of the notch were a few microns further from the central conductor then the middle region. With this difference in separation, the process of vertical alignment simply involved lowering the stripeline until the outer edge of the notch made contact with the sample surface. The gap provided by the additional grinding of the central portion ensured that the stripeline did not make direct physical contact with the fragile central device gates themselves.

This process of direct physical contact for vertical alignment was quick and clean and preferable to initial procedures that were based on creating a protective barrier between the sample and the stripeline with an optically hardened substance such as SU-8, an epoxy-based negative photoresist. With the SU-8 approach, the stripeline was lowered

until it was in contact with the sample. There were numerous problems with the SU-8 approach. First it introduced an additional step in an already length fabrication process. Second, it involved direct physical contact with the sample which although separated by the SU-8 still had the potential to damage the fragile fine device structures. Third, the SU-8 did not always adhere completely to the sample leading to the loss of some devices at the last fabrication stage. Fourth, in the non-hardened regions after lift-off, the SU-8 still left a residue that made bonding difficult. Given its numerous problems, the use of SU-8 was abandoned after the conceptualization and development of the grinding approach.

5 Summary and Future Directions

Once demonstrated, our ESR system with an integrated fast charge detector will be a powerful tool for manipulating and exploring electron charge and spin dynamics. With the μs time resolution of our rf-SET, there are a number of phenomena that it will be possible to investigate. Along with our collaborators at the University of Wisconsin, significant progress has been made in developing material and techniques to produce DQDs in strained SiGe with a high yield. With the faster gating times τ_π enabled by the higher g factor and the longer decoherence times T_2 due to the absence of a nuclear spin bath, a possible future research direction is the use of SiGe DQDs in the ESR set-up.

With respect to the piezoelectrically mediated shot noise feedback loop discussed in Chapter 2, a first relatively straight-forward immediate extension of the work would include an effort to improve the response of the system by increasing its Q. As attention was not directed towards optimizing this during the experiment, significant advances might be readily attainable. For all of the devices measured as described in Section 4.3, the samples were attached to a rigid measurement platform with rubber cement applied to one side. Suspending the crystal sample by some mechanism would be an interesting and easy modification. In addition, the epitaxial growth of the heterostructure leaves a remnant layer of indium on the GaAs substrate. This layer provides an ill-defined amorphous component to the otherwise highly crystalline structure of the sample. Its removal can be readily achieved with a standard bromide etch which should improve the resonant properties of the sample. In general, improvements in the mechanical Q are likely to make backaction effects more pronounced and easier to detect, as was the case for nanotube resonators [73–76]. In addition the increased spectral resolution provided

by a higher *Q* should allow us to explore finer details in the signal such as any harmonic components.

Another interesting and relatively straight-forward extension of the rf-QPC work would be the inclusion of an on-chip matching network as was done for the rf-QPC ESR samples and for the low dissipation rf-SET work done in the lab [35]. The primary benefits of a superconducting on-chip matching network are better impedance matching and the removal of signal loss mechanisms. With these techniques, two specific issues that would be interesting to further investigate are the details of the Fano factor measurements and the nature of the coupling between the rf-QPC and the mechanical resonator. With respect to the Fano factor measurements as can be seen in Figure 2.15, there are regions where the noise is strongly sub-Poissonian. It would be interesting to more precisely verify these measurements as sub-Poissonian noise is a quantum mechanical rather than a classic phenomenon. In addition measurements in the regime where the shot noise is suppressed would allow the exploration of a rf-QPC relative to the quantum limit [77–79]. With respect to the coupling between the rf-QPC and the mechanical resonator, this interaction as discussed above, is via the bias voltage. As such, the nature of the backaction is qualitatively different from most other systems. As mentioned in Section 2.4, L.L. Benatov and M.P. Blencowe [47] have shown it is possible to recast the bias electro-mechanical coupling to a variation in barrier height via a polaron transformation. The difference is that the coupling is now via the crystal's momentum and not its position. With an on-chip matching network and other techniques to reduce losses, our results should be more efficient and better calibrated and allow us to further explore the nature of this interesting backaction coupling.

Additional rf-QPC measurements, such as those employing micron or sub-micron devices, would also be of interest in accessing even higher frequency regimes. However, these experiments would be much more involved than those suggested above and would be most appropriate after the completion of the work already described.

6 Appendix

6.1 Calculation of Photon Assisted Shot Noise

Here we give a more in-depth discussion of the theoretical curves show in Figure 2.8. The plotted curves are derived from an expression for photon-assisted shot noise $S_I(\omega,\omega_0)$ at a frequency ω due to an ac drive at a frequency ω_0

$$S_I(\omega,\omega_0)=\frac{4e^2}{h}\sum_n T_n(1-T_n)\sum_{l=-\infty}^{\infty}(\hbar\omega+l\hbar\omega_0)J_l^2(\alpha)\coth\left[\frac{\hbar\omega+l\hbar\omega_0}{2k_BT}\right]$$

where $\alpha=\sqrt{2}eV_{\mathrm{rf}}^{\mathrm{QPC}}/\hbar\omega_0$, $V_{\mathrm{rf}}^{\mathrm{QPC}}$ is the rms amplitude of the ac bias voltage across the QPC, and $J_l(x)$ is a Bessel function of the first kind. This expression can be derived from a more general expression for the shot noise given by Pedersen and Büttiker [44] under the assumption that the transmission coefficients T_n are independent of energy and assuming zero dc bias across the QPC. This form is equivalent to that for the zero frequency photon-assisted shot noise at non-zero dc bias V_{dc} given elsewhere [45] with the substitution of $\hbar\omega$ for eV_{dc}.

To make a comparison between this expression and our experimental results, we first identify the rms amplitude of the voltage across the QPC as $V_{\mathrm{rf}}^{\mathrm{QPC}}=2Q\sqrt{P_{\mathrm{in}}Z_0}$. We take the electron temperature to be 85 mK (the results are not very sensitive to this parameter). For large values of the argument α of the Bessel function (in our case $\alpha\approx 99$ for P_{in} = -88 dBm) the series converges for a number of terms on the order of 2α

and can easily be summed numerically. We note that the $l = 0$ term in the series corresponds to thermal noise of electron hole pairs rather than partition noise, but it is negligible for large α. While the shot noise $S_I(\omega, \omega_0)$ predicted by theory is frequency-dependent, its variation with frequency is very weak (less than 0.1% over the range of frequencies in our measurement) and cannot explain our data. We can, however, compare the integrated shot noise predicted by theory with the measured integrated excess noise $\mathcal{P}_n^E$. This latter quantity is calculated from the raw noise spectra by integrating the noise power for frequencies in the range $f_0 + 10\,\text{kHz}$ to $f_0 + 4.81\text{MHz}$ once with and once without rf power applied and taking the difference of the two measurements. We checked the major visible features in P_n (*e.g.*, the noise peak at $f_0 + 580\,\text{kHz}$) for scaling as $P_{\text{in}}^{1/2}$ before including them in the calculation of $\mathcal{P}_n^E$. It was not necessary to exclude any features from calculation of $\mathcal{P}_n^E$ for the data presented in Figure 2.7 and Figure 2.8. In the rf data presented, both input power and measured noise power are referred to the input of the HEMT amplifier. The resolution bandwidth (RBW) for all noise spectra is 10 kHz.

To make a comparison with theory, we first convert the theoretical expression for shot noise at the QPC to noise power at the input to the HEMT amplifier. Following Korotkov and Paalanen [80], we take the voltage noise outside the resonant circuit to be given by $S_V(\omega, \omega_0) = (2L/C_p) S_I(\omega, \omega_0)$ where we have assumed that the temporal fluctuations of the shot noise occur slowly in comparison to the oscillations of the carrier wave. Rather than integrate over the measurement bandwidth, we make use of the fact

that $S_I(\omega,\omega_0)$ varies only weakly with frequency, and simply evaluate it at $f_0+1\,\mathrm{MHz}$ and multiply by the measurement bandwidth BW. Finally, we convert to noise power to obtain a theoretical expression for the integrated excess noise $\mathcal{P}^E_{n,\mathrm{th}}=(2L/C_pZ_0)S_I(\omega,\omega_0)\,\mathrm{BW}$ that we then use to produce the dashed curves in Figure 2.8.

Agreement is excellent, considering the considerable uncertainties associated with our estimates of the rf voltage across the QPC and the noise voltage at the HEMT amplifier due to the shot noise. These uncertainties arise primarily because of losses in the matching network, which ensure that our estimates for $V_{\mathrm{rf}}^{\mathrm{QPC}}$ and $S_V(\omega,\omega_0)=(2L/C_p)S_I(\omega,\omega_0)$ are both upper bounds. While the inductor in our matching network is superconducting, the bond pads and wires are normal metal. To account for the losses due to normal metal components and the ohmic contacts, and the imperfect impedance matching of our network, we introduce a factor *K* that characterizes the fraction of available power from the QPC that reaches the measurement circuitry; we can then write $\mathcal{P}^E_{n,\mathrm{th}}\approx(K\,S_I(\omega,\omega_0)/G_{\mathrm{QPC}})\,\mathrm{BW}$. The 3.9 dB reduction used to fit our theory to experiment in Figure 2.8 corresponds to $K\approx 0.16$. Improved performance and noise sensitivity could be achieved by use of a fully superconducting on-chip matching network for which impedance matching would be better and losses would be negligible [35]. Using the above notation, we can relate the measured excess noise power P_n^E to the voltage and current spectral densities S_V and S_I by means of $P_n^E=G_{QPC}KS_V\mathrm{RBW}=KS_I\mathrm{RBW}/G_{QPC}$ leading to an expression $S_I^{\mathrm{meas}}=G_{QPC}P_n^E/K\,\mathrm{RBW}$ for the measured spectral density of current noise in terms of

the measured excess noise. This expression is used to calculate the Fano factor presented in the main text in Figure 2.15.

6.2 Resonant Mode Calculation: Displacement, Strain, and Polarization Fields

6.2.1 Resonant Modes and Displacement Vectors

This section provides details on the calculation of the resonant modes and their corresponding resonant frequencies discussed above in Section 2.6. In general our analysis follows Nishiguchi, *et al*. [55] and implements the techniques discussed in Visscher, *et al* [54], both of whom start from the variational approach that Demarist [81], [82] applied to the problem of an anisotropic elastic body.

We begin by applying Hamilton's principle and form the Lagrangian with its kinetic and potential energy terms

$$L = \int_{\mathrm{V}} \left[\frac{\rho}{2} \omega^2 u_i u_i - \frac{1}{2} c_{ijkl} \partial_i u_j \partial_k u_l \right] \mathrm{dV} \qquad 6.1$$

where ρ is the mass density, ω is the angular frequency, u_i is the i^{th} components of the displacement vector $\boldsymbol{u}$, and c_{ijkl} is the elastic stiffness constant analogous to a microscopic spring constant. Throughout repeated indices imply summation. A shift in $u_i \rightarrow u_i + \delta u_i$ generates a variation δL in the Lagrangian

$$\delta L = \int_{\mathrm{V}} \left[\frac{\rho}{2} \omega^2 u_i + \partial_j \sigma_{ji} \right] \delta u_i \ \mathrm{dV} - \int_{\mathrm{S}} n_j \sigma_{ji} \delta u_i \, \mathrm{dS} \qquad 6.2$$

where n_j is a unit vector normal to the surface S and $\sigma_{ij} = c_{ijkl} \partial_k u_l$ is the stress tensor.

The boundary conditions for our freestanding rectangular GaAs parallelepiped is that the stress field vanishes on the surface S,

$$\sigma_{ij} n_j \,|_{\mathrm{S}} = 0. \tag{6.3}$$

Applying these boundary conditions 6.3 and assuming that the Lagrangian has a minimum with respect to u_i yields elastic wave equation

$$\rho\omega^2 u_i + \partial_l \sigma_{li} = 0. \tag{6.4}$$

To solve, we expand with the displacement vectors $\boldsymbol{u}$ with a complete set of basis functions $\{\Phi_\lambda\}$ as $u_i = \chi_{i\lambda}\Phi_\lambda$. This yields the relation

$$\chi_{i\lambda}\rho\omega^2\Phi_\lambda + \chi_{l\lambda} c_{ijkl}\partial_i\partial_k\Phi_\lambda = 0. \tag{6.5}$$

We now multiply by $\Phi_{\lambda'}$ and integrate over the volume of the GaAs crystal $\mathrm{V=W\times L\times H}$ to achieve the generalized eigenvalue problem

$$\chi_{i\lambda}\rho\omega^2 \int \Phi_{\lambda'}\Phi_\lambda \mathrm{dv} - \chi_{l\lambda} c_{ijkl} \int \partial_j \Phi_{\lambda'} \partial_k \Phi_\lambda \mathrm{dv} = 0. \tag{6.6}$$

This can be rewritten in matrix form

$$\left[\omega^2[\mathrm{E}] - [\Gamma]\right][\chi] = 0 \tag{6.7}$$

where the matrix elements $E_{\lambda i\lambda' i'}$ and $\Gamma_{\lambda i\lambda' i'}$ are given by

$$E_{\lambda i\lambda' i'} = \delta_{ii'}\frac{\rho}{V}\int \Phi_{\lambda'}\Phi_\lambda \mathrm{dV}, \text{ and} \tag{6.8}$$

$$\Gamma_{\lambda i\lambda' i'} = \frac{c_{iji'j'}}{V}\int \partial_j \Phi_\lambda \partial_{j'} \Phi_{\lambda'} \mathrm{dV}. \qquad 6.9$$

As suggested by Nishiguchi *et al.* [55], an effective set of basis functions for calculational purposes is

$$\Phi_\lambda = \left(\frac{2x}{\mathrm{L}}\right)^l \left(\frac{2y}{\mathrm{W}}\right)^m \left(\frac{2z}{\mathrm{H}}\right)^n . \qquad 6.10$$

where the length L in *x*, the width W in *y*, and height H in *z* of the parallelepiped are as discussed in the main text, for example as shown in Figure 2.1. This choice of basis functions is convenient for several reasons. First, λ is completely specified by the triplet of numbers $\{l,m,n\}$. Second the form matches the symmetry of the problem making the integrals in $E_{\lambda i\lambda' i'}$ and $\Gamma_{\lambda i\lambda' i'}$ straight forward to calculate. Lastly, as is shown below, the parity of the components can be used to greatly simplify the problem, and the with the form 6.10, the parity of the basis functions is easily determined and is specified by the triplet $\left[(-1)^l,(-1)^m,(-1)^n\right]$.

In calculating the matrix elements $\Gamma_{\lambda i\lambda' i'}$ and $E_{\lambda i\lambda' i'}$ integrals of the following form are encountered

$$\begin{aligned}\frac{1}{\mathrm{V}}\int \Phi_\lambda \mathrm{dV} &= \frac{1}{\mathrm{V}}\int \left(\frac{2x}{\mathrm{L}}\right)^l \left(\frac{2y}{\mathrm{W}}\right)^m \left(\frac{2z}{\mathrm{H}}\right)^n \mathrm{dV} \\ &= \frac{1}{\mathrm{V}}\frac{1}{(l+1)}\frac{\mathrm{L}}{2}\left(\frac{2x}{\mathrm{L}}\right)^{l+1}\Big|_{-\frac{\mathrm{L}}{2}}^{\frac{\mathrm{L}}{2}} \times \frac{1}{(m+1)}\frac{\mathrm{W}}{2}\left(\frac{2y}{\mathrm{W}}\right)^{m+1}\Big|_{-\frac{\mathrm{W}}{2}}^{\frac{\mathrm{W}}{2}} \times \frac{1}{(n+1)}\frac{\mathrm{L}}{2}\left(\frac{2z}{\mathrm{H}}\right)^{n+1}\Big|_{-\frac{\mathrm{H}}{2}}^{\frac{\mathrm{H}}{2}} .\end{aligned} \qquad 6.11$$

This simplifies to

$$\begin{aligned}\frac{1}{\mathrm{V}}\int \Phi_{\lambda}\mathrm{dV} &= \frac{1}{\mathrm{V}}\frac{(\mathrm{LWH}/8)}{(l+1)(m+1)(n+1)}[1^{l+1}-(-1)^{l+1}][1^{m+1}-(-1)^{m+1}][1^{n+1}-(-1)^{n+1}] \\ &\equiv F(l,m,n) \\ &= \frac{1}{(l+1)(m+1)(n+1)}\delta_{l,even}\delta_{m,even}\delta_{n,even}.\end{aligned} \tag{6.12}$$

The calculation of the matrix elements is greatly simplified by the cubic symmetry of GaAs which reduces the number of independent stiffness constants c_{ijkl} from the general case of 21 for a generic medium to four. Using abbreviated subscripts given the simplification, the stiffness tensor is

$$\begin{pmatrix} c_{11} & c_{12} & c_{12} & 0 & 0 & 0 \\ c_{12} & c_{11} & c_{12} & 0 & 0 & 0 \\ c_{12} & c_{12} & c_{11} & 0 & 0 & 0 \\ 0 & 0 & 0 & c_{44} & 0 & 0 \\ 0 & 0 & 0 & 0 & c_{44} & 0 \\ 0 & 0 & 0 & 0 & 0 & c_{44} \end{pmatrix} \tag{6.13}$$

where

$$\begin{aligned} &c_{11} = c_{xxxx} = c_{22} = c_{33} \\ &c_{12} = c_{xxyy} = c_{21} = c_{13} = c_{31} = c_{23} = c_{32} \\ &c_{44} = c_{xyxy} = c_{55} = c_{66} \end{aligned} \tag{6.14}$$

$$c_{ijkl} = 0 \text{ for all other combinations}$$

with

$$
\begin{aligned}
1 &= xx \\
2 &= yy \\
3 &= zz \\
4 &= yz, zy \\
5 &= xz, zx \\
6 &= xy, yx.
\end{aligned}
\qquad 6.15
$$

For arbitrary λ, λ' there are nine Γ matrix elements as i, i' each run over $x, y, z.$ As an example, consider the first Γ matrix element for $i, i' = x$

$$
\begin{aligned}
\Gamma_{\lambda x \lambda' x} &= \frac{c_{xjxj'}}{\mathrm{V}} \int \frac{\partial \Phi_\lambda}{\partial x_j} \frac{\partial \Phi_{\lambda'}}{\partial x_{j'}} \mathrm{dV} \\
&= \frac{c_{xjxj'}}{\mathrm{V}} \sum_{j=x,y,z} \sum_{j'=x,y,z} \int \frac{\partial \Phi_\lambda}{\partial x_j} \frac{\partial \Phi_{\lambda'}}{\partial x_{j'}} \mathrm{dV}.
\end{aligned}
\qquad 6.16
$$

Given 6.13 and 6.14 the only non-zero terms in the sum are

$$
\Gamma_{\lambda x \lambda' x} = \frac{c_{11}}{\mathrm{V}} \int \frac{\partial \Phi_\lambda}{\partial x} \frac{\partial \Phi_{\lambda'}}{\partial x} \mathrm{dV} + \frac{c_{44}}{\mathrm{V}} \int \frac{\partial \Phi_\lambda}{\partial y} \frac{\partial \Phi_{\lambda'}}{\partial y} \mathrm{dV} + \frac{c_{44}}{\mathrm{V}} \int \frac{\partial \Phi_\lambda}{\partial z} \frac{\partial \Phi_{\lambda'}}{\partial z} \mathrm{dV}. \qquad 6.17
$$

Considering the first term by way of example and using 6.12

$$
\begin{aligned}
\frac{c_{11}}{\mathrm{V}} \int \frac{\partial \Phi_\lambda}{\partial x} \frac{\partial \Phi_{\lambda'}}{\partial x} \mathrm{dV} &= \frac{c_{11}}{\mathrm{V}} \int \frac{\partial \left(\left(\frac{2x}{\mathrm{L}} \right)^l \left(\frac{2y}{\mathrm{W}} \right)^m \left(\frac{2z}{\mathrm{H}} \right)^n \right)}{\partial x} \frac{\partial \left(\left(\frac{2x}{\mathrm{L}} \right)^{l'} \left(\frac{2y}{\mathrm{W}} \right)^{m'} \left(\frac{2z}{\mathrm{H}} \right)^{n'} \right)}{\partial x} \mathrm{dV} \\
&= \frac{c_{11}}{\mathrm{V}} \left(\frac{2}{\mathrm{L}} \right)^2 l l' \int \left(\left(\frac{2x}{\mathrm{L}} \right)^{l-1} \left(\frac{2y}{\mathrm{W}} \right)^m \left(\frac{2z}{\mathrm{H}} \right)^n \right) \left(\left(\frac{2x}{\mathrm{L}} \right)^{l'-1} \left(\frac{2y}{\mathrm{W}} \right)^{m'} \left(\frac{2z}{\mathrm{H}} \right)^{n'} \right) \mathrm{dV} \\
&= \frac{c_{11}}{\mathrm{V}} \left(\frac{2}{\mathrm{L}} \right)^2 l l' \int \Phi \left(l + l' - 2, m + m', n + n' \right) \mathrm{dV} \\
&= \frac{4 c_{11} l l'}{\mathrm{L}^2} F \left(l + l' - 2, m + m', n + n' \right).
\end{aligned}
\qquad 6.18
$$

The total matrix element is then

$$\begin{aligned}\Gamma_{\lambda x\lambda' x} = &\frac{4c_{11}ll'}{\mathrm{L}^2}F\left(l+l'-2,m+m',n+n'\right)\\ &+\frac{4c_{44}mm'}{\mathrm{W}^2}F\left(l+l',m+m'-2,n+n'\right).\\ &+\frac{4c_{44}nn'}{\mathrm{H}^2}F\left(l+l',m+m',n+n'-2\right)\end{aligned} \qquad 6.19$$

The other matrix elements $E_{\lambda i\lambda' i'}$ and $\Gamma_{\lambda i\lambda' i'}$ are calculated in a similar manner.

Now as we consider calculating the eigenvalues and eigenvectors of 6.7, the high degree of symmetry in GaAs great simplifies the problem. In particular a cubic system such as GaAs has inversion symmetry along all three axis; that is, $x\to -x, y\to -y, z\to -z.$ As Demarist showed [81], [82] and as discussed by Ohno [53], this means that the Γ matrix can be split into 8 sub-matrices that can be solved separately. Each of these sub-matrices corresponds to an independent set of modes of vibration. In addition, each set of modes or sub-matrix only connects displacement vectors of particular parities. For example, $u_x:(\mathrm{O,E,E}), u_y:(\mathrm{E,O,E}),$ and $u_z:(\mathrm{E,E,O})$ only appear with each other where E and O represent even and odd parity, respectively. This means that the sets of modes can be classified according to the parity of the displacement vectors. We follow the classification scheme of Ohno [53] based on this fact.

$Od-n$	x	y	z
u_x	O	E	E
u_y	E	O	E
u_z	E	E	O

$Ex-n$	x	y	z
u_x	E	E	E
u_y	O	O	E
u_z	O	E	O

$Ey-n$	x	y	z
u_x	O	O	E
u_y	E	E	E
u_z	E	O	O

$Ez-n$	x	y	z
u_x	O	E	O
u_y	E	O	O
u_z	E	E	E

$Ox-n$	x	y	z
u_x	O	O	O
u_y	E	E	O
u_z	E	O	E

$Oy-n$	x	y	z
u_x	E	E	O
u_y	O	O	O
u_z	O	E	E

$Oz-n$	x	y	z
u_x	E	O	E
u_y	O	E	E
u_z	O	O	O

$Ev-n$	x	y	z
u_x	E	O	O
u_y	O	E	O
u_z	O	O	E

6.20

Table 6-1 Classification of sets of vibrational modes of a rectangular parallelepiped of an orthorhombic crystal according based on the parity (Even/Odd) of the displacements u_x, u_y, u_z according to Ohno [53].

The total number of basis vectors is limited by constraining the total power of each basis function according to

$$l+m+n \le N. \tag{6.21}$$

The total order R of the E and Γ matrices is determined by the number of basis functions according to the condition

$$R = 3\frac{(N+1)(N+2)(N+3)}{6}. \tag{6.22}$$

Equation 6.22 is the number of ways that 6.21 can be realized for non-negative integers with an additional factor accounting for each of the three dimensions. As $R \propto N^3$, the problem quickly become computationally intensive as a function of N. We determined

that limiting the total power of the exponent to seven, i.e., $N = 7,$ provided solutions that were highly accurate while also computationally reasonable.

The basis functions that are used to solve each of the eight reduced eigenvalue equations 6.7 for each sub-matrix E and Γ are selected in accordance with the displacement parity classification system shown in Table 6-1. The generation of the basis functions is facilitated by a generation triplet (p, q, r). The condition 6.21 that $N \leq 7$ requires that the generation triplets satisfy either

$$p + q + r \leq 2 \tag{6.23}$$

or

$$p + q + r \leq 3 \tag{6.24}$$

depending on the parity of the basis function components. The set of 10 generation triplets for 6.23 is

$$\begin{array}{l} (0,0,0) \\ (1,0,0),(0,1,0),(0,0,1) \\ (2,0,0),(0,2,0),(0,0,2),(1,1,0),(1,0,1),(0,1,1) \end{array} \tag{6.25}$$

and the set of 20 generation triplets for 6.24 includes the set 6.25 with the addition of

$$\begin{array}{l} (3,0,0),(0,3,0),(0,0,3) \\ (2,1,0),(2,0,1),(0,2,1),(1,2,0),(1,0,2),(0,1,2) \\ (1,1,1). \end{array} \tag{6.26}$$

By way of example, we consider the *Ey* -n set of flexural modes where the lowest order *Ey*-1 mode is the one we observed being excited as part of the piezoelectric feedback. The basis vectors used to solve 6.7 are those having the proper displacement parity given the constraint in total exponent power. For example, the *x*-displacement parity is $u_x(\mathrm{O,O,E})$ which corresponds to the set of basis functions

$$\Phi_{\lambda=(2p+1,2q+1,2r)} = \left(\frac{2x}{\mathrm{L}}\right)^{2p+1}\left(\frac{2y}{\mathrm{W}}\right)^{2q+1}\left(\frac{2z}{\mathrm{H}}\right)^{2r} \qquad 6.27$$

where $\{p,q,r\}$ are selected from the set 6.25 thereby ensuring that $2(p+q+r)+2 \le 7.$ The set of basis functions for the *y* and *z* displacements are determined in a similar manner with the generation triplets for u_y coming from 6.25 and 6.26 as the even parity for each component corresponds to the condition $2(p+q+r) \le 7.$

This total set of basis functions is used to generate the matrix elements $E_{\lambda i\lambda' i'}$ and $\Gamma_{\lambda i\lambda' i'}$ in accordance with 6.8 and 6.9. We used the functions Eigenvalue and Eigenvector in Mathematica to solve for the eigenvalues ω^2 and eigenvectors $[\chi]$. Using the eigenvectors, the displacement vectors were generated in the following manner, again using the set of *Ey*-n flexural modes as an example,

$$u_x = \sum_{p,q,r}^{2(p+q+r)+2\le 7} \chi_{1,2p+1,2q+1,2r}\left(\frac{2x}{\mathrm{L}}\right)^{2p+1}\left(\frac{2y}{\mathrm{W}}\right)^{2q+1}\left(\frac{2z}{\mathrm{H}}\right)^{2r} \qquad 6.28$$

where $\{p,q,r\}$ are selected from the set 6.25. The *y* and *z* components are generated in a similar manner,

$$u_y = \sum_{p,q,r}^{2(p+q+r)\le 7} \chi_{2,2p,2q,2r} \left(\frac{2x}{\mathrm{L}}\right)^{2p} \left(\frac{2y}{\mathrm{W}}\right)^{2q} \left(\frac{2z}{\mathrm{H}}\right)^{2r} \qquad 6.29$$

where $\{p,q,r\}$ are selected from the sets 6.25 and 6.26 and

$$u_z = \sum_{p,q,r}^{2(p+q+r)+2\le 7} \chi_{3,2p,2q+1,2r+1} \left(\frac{2x}{\mathrm{L}}\right)^{2p} \left(\frac{2y}{\mathrm{W}}\right)^{2q+1} \left(\frac{2z}{\mathrm{H}}\right)^{2r+1} \qquad 6.30$$

where $\{p,q,r\}$ are selected from the set 6.25. For each eigenvector $[\chi]$, there is a corresponding n^{th} vibrational mode given by 6.28, 6.29, and 6.30. The number of particular modes n is determined by the number of basis functions, which for the *EY-n* mode for $N = 7$ is 10+20+10 = 40 where the value of either 10 or 20 corresponds to the generation triplets coming from either 6.25 or 6.25 and 6.26 for a particular component.

6.2.2 Strain and Polarization Fields

The plots of the polarization field ***P*** shown in the main body are based on calculations of the strain field ***S*** which are in turn based on a determination of the displacement vectors as detailed above. As discussed in Section 2.6, mobile electrons in the 2DEG screen the polarization charge resulting in no net electric field ***E*** in the high conductance regions. This means that the electric displacement field ***D*** and the polarization field ***P*** are equal, both of which can be related to the strain field ***S***,

$$\boldsymbol{P} = \boldsymbol{D} = \boldsymbol{e} : \boldsymbol{S} = \begin{bmatrix} 0 & 0 & 0 & e_{x4} & 0 & 0 \\ 0 & 0 & 0 & 0 & e_{x4} & 0 \\ 0 & 0 & 0 & 0 & 0 & e_{x4} \end{bmatrix} \begin{bmatrix} S_1 \\ S_2 \\ S_3 \\ S_4 \\ S_5 \\ S_6 \end{bmatrix}$$

$$= 2e_{x4}\left(S_{yz}\hat{x} + S_{yz}\hat{y} + S_{xy}\hat{z}\right) \qquad 6.31$$

where e_{x4} are piezoelectric stress constants defined by

$$e_{x4} = d_{x4}c_{44}^{E} \qquad 6.32$$

where $\boldsymbol{d}$ is the piezoelectric strain matrix and c^{E} are elastic stiffness constants at constant electric field.

The strain matrix elements are defined by

$$S_{ij} = \frac{1}{2}\left(\frac{\partial u_i}{\partial x_j} + \frac{\partial u_j}{\partial x_i}\right). \qquad 6.33$$

As discussed above in Section 2.6, the *Ey*-1 flexural mode we observe results in a polarization field P_x along the direction of electronic transport. We calculate this field based on the S_{yz} strain matrix element in the following manner where we use the displacements u_y 6.29 and u_z 6.30

$$S_{yz} = \tfrac{1}{2}\sum_{pqr}^{2(p+q+r)\le N} \chi_{2pqr}\,\frac{4r}{H}\left(\frac{2x}{L}\right)^{2p}\left(\frac{2y}{W}\right)^{2q}\left(\frac{2z}{H}\right)^{2r-1} + \tfrac{1}{2}\sum_{pqr}^{2(p+q+r)\le N} \chi_{3pqr}\,\frac{2(2q+1)}{W}\left(\frac{2x}{L}\right)^{2p}\left(\frac{2y}{W}\right)^{2q}\left(\frac{2z}{H}\right)^{2r+1}. \quad 6.34$$

Using these strain field calculations, we were able to determine the geometry of the corresponding vibrational mode and its polarization field. This geometric analysis in turn was central to the development of our understanding of the piezoelectric feedback loop. In particular an analysis of the geometry of the mode whose frequency we observed showed that it could couple not only to mechanical motion but also to charge transport. This analysis had two components. First, as discussed in Section 2.6 and shown in Figure 2.13 andFigure **2.14**, the polarization field P_z had strong dipolar components under the ohmic contacts. This allowed charge fluctuations to piezoelectrically drive mechanical motion. Second, the polarization field in the center of the sample was aligned along the axis of the QPC. This allowed mechanical vibrational energy to couple to charge transport through an ac bias. An analysis of the geometry of the mode therefore showed that electrical energy could be transferred to mechanical energy and back again, the two halves of a piezoelectricly mediated feedback loop.

6.3 2DEG Material and ESR Samples Summary

Source	Identifier	Electron Sheet Density n_s (cm^{-2})	2DEG Depth (nm)	Mobility μ ($cm^2V^{-1}S^{-1}$)	Spacer Thickness (nm)	% Al in Spacer
Pfeiffer	3-30 05.2	1.3×10^{11}	100	3×10^{6}		

Umansky	U-6-98	3.2×10^{11}	57	1.4×10^{6}	25	36
Umansky	U-7-159	2×10^{11}	74	3×10^{6}	42	36
Umansky	U-8-271	3.2×10^{11}	60	3×10^{6}	30	~50

Table 6-2 Summary of the properties of the GaAs/AlGaAs materials used in the ESR experiment.

Sample Number	Measurement Start Date	Material	Charge Sensor	Results/Notes
1	3/3/09	U-8-271	QPC	Electric discharge from stripeline or pulse gates or complications with SU8 processing destroyed sample.
2	5/29/09	U-8-271	SET	Modify SU8 procedures. Electric discharge from stripeline or pulse gates or complications with SU8 processing destroyed sample.
3	6/26/09	U-8-271	QPC	Eliminate SU8 processing step. Electric discharge from stripeline or pulse gates destroyed sample.
4	7/12/09	U-8-271	QPC	Modify rf set-up including 50 ohm terminators on top of pulse gates. Two runs with extensive attempts to form stable dot. Appears local defect causes asymmetric pinch-off preventing simultaneous formation of dot and proper operation of QPC charge sensor.
5	10/5/09	U-98	SET	SET and ohmics have high resistance.
6	10/15/09	U-7-159	QPC	Device gates failed. Failure mechanism unclear as post run optical analysis provided inconclusive feedback.
7	12/12/09	U-8-271	QPC	Two runs but high resistance

				ohmics prevents effective dot and QPC measurements.
8	1/20/10	U-7-159	QPC	Three runs but high resistance ohmics prevents effective dot and QPC measurements.
9	2/19/10	U-8-271	QPC	Two runs. Not adequate range for source QPC to form effective dots for measurement. Suspect nanomagnet may complicate QPC formation.
10	3/26/10	U-98	SET	Unstable dot and not possible to modulate SET.
11	5/14/10	U-98	SET	Able to form nice stable single and double dot. No SET coupling to dot or SET gate.
12	6/25/10	U-98	QPC	Add gate to ground nanomagnet. Able to form nice stable single and double dots. QPC current too noisy for effective rf data.
13	10/19/10	U-98	QPC	Four runs. IVC leak. Numerous attempts to resolve leak. For fourth run, not possible to form dots. Possible problem with gates.
14	2/18/11	U-98	QPC	First run terminated by IVC leak. For second and third run, QPC current too noisy.
15	4/23/11	U-98	QPC	Additional etch to promote QPC stability. IVC leak terminated run.

Table 6-3 Summary of the fifteen QPC and SET samples run as part of the ESR experiment.

7 Bibliography

[1] J. Stettenheim, M. Thalakulam, F. Pan, M. Bal, Z. Ji, W. Xue, L. Pfeiffer, K. W. West, M. P. Blencowe, and A. J. Rimberg, "A macroscopic mechanical resonator driven by mesoscopic electrical back-action," *Nature*, vol. 466, no. 7302, pp. 86–90, Jul. 2010.

[2] B. J. van Wees, H. van Houten, C. W. J. Beenakker, J. G. Williamson, L. P. Kouwenhoven, D. van der Marel, and C. T. Foxon, "Quantized conductance of point contacts in a two-dimensional electron gas," *Phys. Rev. Lett.*, vol. 60, no. 9, pp. 848–850, Feb. 1988.

[3] D. A. Wharam, T. J. Thornton, R. Newbury, M. Pepper, H. Ahmed, J. E. F. Frost, D. G. Hasko, D. C. Peacock, D. A. Ritchie, and G. A. C. Jones, "One-dimensional transport and the quantisation of the ballistic resistance," *Journal of Physics C: Solid State Physics*, vol. 21, no. 8, pp. L209–L214, Mar. 1988.

[4] M. A. Topinka, B. J. LeRoy, S. E. J. Shaw, E. J. Heller, R. M. Westervelt, K. D. Maranowski, and A. C. Gossard, "Imaging Coherent Electron Flow from a Quantum Point Contact," *Science*, vol. 289, no. 5488, pp. 2323–2326, Sep. 2000.

[5] S. M. Cronenwett, H. J. Lynch, D. Goldhaber-Gordon, L. P. Kouwenhoven, C. M. Marcus, K. Hirose, N. S. Wingreen, and V. Umansky, "Low-Temperature Fate of the 0.7 Structure in a Point Contact: A Kondo-like Correlated State in an Open System," *Phys. Rev. Lett.*, vol. 88, no. 22, p. 226805, May 2002.

[6] A. Golub, T. Aono, and Y. Meir, "Suppression of Shot Noise in Quantum Point Contacts in the '0.7 Regime'," *Phys. Rev. Lett.*, vol. 97, no. 18, p. 186801, Nov. 2006.

[7] M. Aspelmeyer and K. Schwab, "Focus on mechanical systems at the quantum limit," *N. J. Phys.*, vol. 10, p. 095001, 2008.

[8] T. J. Kippenberg and K. J. Vahala, "Cavity optomechanics: back-action at the mesoscale," *Science*, vol. 321, pp. 1172–1176, 2008.

[9] M. P. Blencowe, "Quantum electromechanical systems," *Phys. Rep.*, vol. 395, pp. 159–222, 2004.

[10] O. Usmani, Y. M. Blanter, and Y. Nazarov, "Strong feedback and current noise in nanoelectromechanical systems," *Phys. Rev. B*, vol. 75, p. 195312, 2007.

[11] D. Rodrigues, “Fano-like antiresonances in nanomechanical and optomechanical systems,” *Phys. Rev. Lett.*, vol. 102, p. 067202, 2009.

[12] S. Datta, *Electronic transport in mesoscopic systems*. Cambridge ; New York: Cambridge University Press, 1995.

[13] D. K. Ferry, *Transport in nanostructures*, 2nd ed. Cambridge, UK ; New York: Cambridge University Press, 2009.

[14] M. Atatüre, J. Dreiser, A. Badolato, A. Högele, K. Karrai, and A. Imamoglu, “Quantum-Dot Spin-State Preparation with Near-Unity Fidelity,” *Science*, vol. 312, no. 5773, pp. 551–553, Apr. 2006.

[15] Y. Imry, *Introduction to mesoscopic physics*, 2nd ed. Oxford ; New York: Oxford University Press, 2002.

[16] S. M. Cronenwett, “Coherence, Charging, and Spin Effects in Quantum Dots and Point Contacts,” PhD Thesis, Stanford University, 2001.

[17] A. Yacoby, U. Sivan, C. P. Umbach, and J. M. Hong, “Interference and dephasing by electron-electron interaction on length scales shorter than the elastic mean free path,” *Physical review letters*, vol. 66, no. 14, pp. 1938–1941, 1991.

[18] M. Kastner, “Artificial Atoms,” *Physics Today*, vol. 46, pp. 24–31, 1993.

[19] L. P. Kouwenhoven, C. M. Marcus, P. L. McEuen, S. Tarucha, R. M. Westervelt, and N. S. Wingreen, “Electron Transport in Quantum Dots,” in *Mesoscopic Electron Transport*, L. L. Sohn, G. Schön, and L. P. Kouwenhoven, Eds. Dordrecht: Kluwer Academic Publishers, 1997.

[20] T. J. Drummond, W. T. Masselink, and H. Morkoc, “Modulation-doped GaAs/(Al, Ga) As heterojunction field-effect transistors: MODFETs,” *Proceedings of the IEEE*, vol. 74, no. 6, pp. 773–822, 1986.

[21] A. C. Johnson, “Charge Sensing and Spin Dynamics in GaAs Quantum Dots,” PhD Thesis, Harvard University, 2005.

[22] L. P. Kouwenhoven, L. L. Sohn, and P. L. Schön, “Introduction to Mesoscopic Electron Transport,” in *Mesoscopic Electron Transport*, L. L. Sohn, G. Schön, and L. P. Kouwenhoven, Eds. Dordrecht: Kluwer Academic Publishers, 1997.

[23] K. F. Berggren, T. J. Thornton, D. J. Newson, and M. Pepper, "Magnetic depopulation of 1D subbands in a narrow 2D electron gas in a GaAs: AlGaAs heterojunction," *Physical review letters*, vol. 57, no. 14, p. 1769, 1986.

[24] S. E. Laux, D. J. Frank, and F. Stern, "Quasi-one-dimensional electron states in a split-gate GaAs/AlGaAs heterostructure," *Surface Science*, vol. 196, no. 1, pp. 101–106, 1988.

[25] J. Nygård, "Tutorial on Electronic Transport," presented at the NT05: Sixth International Conference on Science and Applications of Nanotubes, Göteborg University, 2005.

[26] L. P. Kouwenhoven, D. G. Austing, and S. Tarucha, "Few-electron quantum dots," *Reports on Progress in Physics*, vol. 64, p. 701, 2001.

[27] H. Van Houten, C. W. J. Beenakker, and A. A. M. Staring, "Coulomb blockade oscillations in semiconductor nanostructures," in *Single Charge Tunneling: Coulomb Blockade Phenomena in Nanostructures*, H. Grabert and M. H. Devoret, Eds. New York: Plenum Press, 1992.

[28] M. A. Kastner, "The single-electron transistor," *Reviews of Modern Physics*, vol. 64, no. 3, p. 849, 1992.

[29] J. M. Elzerman, R. Hanson, L. H. W. van Beveren, S. Tarucha, L. M. K. Vandersypen, and L. P. Kouwenhoven, "Semiconductor Few-Electron Quantum Dots as Spin Qubits," in *Quantum Dots: a Doorway to Nanoscale Physics*, vol. 667, W. Dieter Heiss, Ed. Springer Berlin / Heidelberg, 2005, pp. 289–331.

[30] S. R. Patel, "Electronic Ground State Properties of Coulomb Blockaded Quantum Dots," PhD Thesis, Stanford University, 2002.

[31] W. G. van der Wiel, S. De Franceschi, J. M. Elzerman, T. Fujisawa, S. Tarucha, and L. P. Kouwenhoven, "Electron transport through double quantum dots," *Reviews of Modern Physics*, vol. 75, no. 1, p. 1, 2002.

[32] R. J. Schoelkopf, P. Wahlgren, A. A. Kozhevnikov, P. Delsing, and D. E. Prober, "The radio-frequency single-electron transistor (RF-SET): a fast and ultrasensitive electrometer," *Science*, vol. 280, pp. 1238–1242, 1998.

[33] M. H. Devoret, R. J. Schoelkopf, and others, "Amplifying quantum signals with the single-electron transistor," *Nature*, vol. 406, no. 6799, pp. 1039–1046, 2000.

[34] D. J. Reilly, C. M. Marcus, M. P. Hanson, and A. C. Gossard, "Fast single-charge sensing with a rf quantum point contact," *Appl. Phys. Lett.*, vol. 91, p. 162101, 2007.

[35] W. W. Xue, Z. Ji, F. Pan, J. Stettenheim, M. P. Blencowe, and A. J. Rimberg, "Measurement of quantum noise in a single-electron transistor near the quantum limit," *Nature Physics*, vol. 5, no. 9, pp. 660–664, 2009.

[36] A. Aassime, D. Gunnarsson, K. Bladh, P. Delsing, and R. Schoelkopf, "Radio-frequency single-electron transistor: Toward the shot-noise limit," *Applied physics letters*, vol. 79, p. 4031, 2001.

[37] W. Lu, Z. Ji, L. Pfeiffer, K. W. West, A. J. Rimberg, and others, "Real-time detection of electron tunnelling in a quantum dot," *Nature*, vol. 423, no. 6938, pp. 422–425, 2003.

[38] M. Thalakulam, Z. Ji, and A. J. Rimberg, "Sensitivity and linearity of superconducting radio-frequency single-electron transistors: Effects of quantum charge fluctuations," *Physical review letters*, vol. 93, no. 6, p. 66804, 2004.

[39] S. L. Pohlen, "The Superconducting Single Electron Transistor," PhD Thesis, Harvard, 1999.

[40] W. Lu, "Single Electron Transistor: Effects of the Environment and Detecting Electron Motion in Real Time," PhD Thesis, Rice University, 2003.

[41] M. Thalakulam, "Development and Study of Charge Sensors for Fast Charge Detection in Quantum Dots," PhD Thesis, Rice, 2007.

[42] W. Xue, "On-Chip Superconducting LC Matching Networks and Coplanar Waveguides for Radio-Frequency Single Electron Transistors," PhD Thesis, Dartmouth College, 2009.

[43] Blanter and M. Buttiker, "Shot noise in mesoscopic conductors," *Phys. Rep.*, vol. 336, pp. 1–166, 2000.

[44] M. H. Pedersen and M. Büttiker, "Scattering theory of photon-assisted electron transport," *Physical Review B*, vol. 58, no. 19, p. 12993, 1998.

[45] R. J. Schoelkopf, A. A. Kozhevnikov, D. E. Prober, and M. J. Rooks, "Observation of 'Photon-Assisted' Shot Noise in a Phase-Coherent Conductor," *Physical review letters*, vol. 80, no. 11, pp. 2437–2440, 1998.

[46] V. B. Braginsky and F. Khalili, “Quantum Measurement.” Nature Publishing Group, a division of Macmillan Publishers Limited. All Rights Reserved., 1992.

[47] L. L. Benatov and M. P. Blencowe, “A nanomechanical resonator coupled linearly via its momentum to a quantum point contact,” *arXiv:1204.3871,* Apr. 2012.

[48] Y. Meir, K. Hirose, and N. S. Wingreen, “Kondo model for the ‘0.7 anomaly’ in transport through a quantum point contact,” *Phys. Rev. Lett.*, vol. 89, p. 196802, 2002.

[49] S. Kogan, “Electronic Noise and Fluctuations in Solids.” Nature Publishing Group, a division of Macmillan Publishers Limited. All Rights Reserved., 1996.

[50] L.-H. Reydellet, P. Roche, and D. C. Glattli, “Quantum partition noise of photon-created electron-hole pairs,” *Phys. Rev. Lett.*, vol. 90, p. 176803, 2003.

[51] L. DiCarlo, “Shot-noise signatures of 0.7 structure and spin in a quantum point contact,” *Phys. Rev. Lett.*, vol. 97, p. 036810, 2006.

[52] G. B. Lesovik and L. S. Levitov, “Noise in an ac biased junction: nonstationary Aharanov-Bohm effect,” *Phys. Rev. Lett.*, vol. 72, pp. 538–541, 1994.

[53] I. Ohno, “Free vibration of a rectangular parallelepiped crystal and its application to determination of elastic constants of orthorhombic crystals,” *J. Phys. Earth*, vol. 24, pp. 355–379, 1976.

[54] W. M. Visscher, A. Migliori, T. M. Bell, and R. A. Reinert, “On the normal-modes of free-vibration of inhomogeneous and anisotropic elastic objects,” *J. Acoust. Soc. Am.*, vol. 90, pp. 2154–2162, 1991.

[55] N. Nishiguchi, Y. Ando, and M. N. Wybourne, “Acoustic phonon modes of rectangular quantum wires,” *Journal of Physics: Condensed Matter*, vol. 9, p. 5751, 1997.

[56] J. Soderkvist, “Activation and detection of mechanical vibrations in piezoelectric beams,” *Sens. Actuators A Phys.*, vol. 32, pp. 567–571, 1992.

[57] A. Naik, “Cooling a nanomechanical resonator with quantum back-action,” *Nature*, vol. 443, pp. 193–196, 2006.

[58] J. Koch and F. von Oppen, “Franck-Condon blockade and giant Fano factors in transport through single molecules,” *Phys. Rev. Lett.*, vol. 94, p. 206804, 2005.

[59] D. Loss and D. P. DiVincenzo, "Quantum computation with quantum dots," *Phys. Rev. A*, vol. 57, no. 1, pp. 120–126, Jan. 1998.

[60] J. R. Petta, A. C. Johnson, J. M. Taylor, E. A. Laird, A. Yacoby, M. D. Lukin, C. M. Marcus, M. P. Hanson, and A. C. Gossard, "Coherent manipulation of coupled electron spins in semiconductor quantum dots," *Science*, vol. 309, no. 5744, pp. 2180–2184, 2005.

[61] R. Hanson, B. Witkamp, L. M. K. Vandersypen, L. H. W. van Beveren, J. M. Elzerman, and L. P. Kouwenhoven, "Zeeman energy and spin relaxation in a one-electron quantum dot," *Physical review letters*, vol. 91, no. 19, p. 196802, 2003.

[62] T. Fujisawa, D. G. Austing, Y. Tokura, Y. Hirayama, and S. Tarucha, "Allowed and forbidden transitions in artificial hydrogen and helium atoms," *Nature*, vol. 419, no. 6904, 2002.

[63] H. Bluhm, S. Foletti, I. Neder, M. Rudner, D. Mahalu, V. Umansky, and A. Yacoby, "Dephasing time of GaAs electron-spin qubits coupled to a nuclear bath exceeding 200 micro seconds," *Nat. Phys.*, vol. 7, no. 2, pp. 109–113, Feb. 2011.

[64] H.-A. Engel and D. Loss, "Detection of Single Spin Decoherence in a Quantum Dot via Charge Currents," *Phys. Rev. Lett.*, vol. 86, no. 20, pp. 4648–4651, May 2001.

[65] F. H. L. Koppens, C. Buizert, K. J. Tielrooij, I. T. Vink, K. C. Nowack, T. Meunier, L. P. Kouwenhoven, and L. M. K. Vandersypen, "Driven coherent oscillations of a single electron spin in a quantum dot," *Nature*, vol. 442, no. 7104, pp. 766–771, Aug. 2006.

[66] A. V. Khaetskii, D. Loss, and L. Glazman, "Electron spin decoherence in quantum dots due to interaction with nuclei," *Physical review letters*, vol. 88, no. 18, p. 186802, 2002.

[67] H.-A. Engel and D. Loss, "Fermionic Bell-State Analyzer for Spin Qubits," *Science*, vol. 309, no. 5734, pp. 586–588, Jul. 2005.

[68] C. W. J. Beenakker, D. P. DiVincenzo, C. Emary, and M. Kindermann, "Charge Detection Enables Free-Electron Quantum Computation," *Phys. Rev. Lett.*, vol. 93, no. 2, p. 020501, Jul. 2004.

[69] E. A. Laird, J. R. Petta, A. C. Johnson, C. M. Marcus, A. Yacoby, M. P. Hanson, and A. C. Gossard, "Effect of Exchange Interaction on Spin Dephasing in a Double Quantum Dot," *Phys. Rev. Lett.*, vol. 97, no. 5, p. 056801, Jul. 2006.

[70] F. H. L. Koppens, J. A. Folk, J. M. Elzerman, R. Hanson, L. H. W. van Beveren, I. T. Vink, H. P. Tranitz, W. Wegscheider, L. P. Kouwenhoven, and L. M. K. Vandersypen, "Control and Detection of Singlet-Triplet Mixing in a Random Nuclear Field," *Science*, vol. 309, no. 5739, pp. 1346–1350, Aug. 2005.

[71] K. Ono, D. G. Austing, Y. Tokura, and S. Tarucha, "Current rectification by Pauli exclusion in a weakly coupled double quantum dot system," *Science*, vol. 297, no. 5585, pp. 1313–1317, 2002.

[72] R. De Sousa and S. D. Sarma, "Theory of nuclear-induced spectral diffusion: Spin decoherence of phosphorus donors in Si and GaAs quantum dots," *Physical Review B*, vol. 68, no. 11, p. 115322, 2003.

[73] B. Lassagne, Y. Tarakanov, J. Kinaret, D. Garcia-Sanchez, and A. Bachtold, "Coupling mechanics to charge transport in carbon nanotube mechanical resonators," *Science*, vol. 325, pp. 1107–1110, 2009.

[74] S. D. Bennett, J. Maassen, and A. A. Clerk, "Scattering approach to backaction in coherent nanoelectromechanical systems," *Physical review letters*, vol. 105, no. 21, p. 217206, 2010.

[75] S. Sapmaz, P. Jarillo-Herrero, Y. M. Blanter, C. Dekker, and H. S. J. van der Zant, "Tunneling in Suspended Carbon Nanotubes Assisted by Longitudinal Phonons," *Phys. Rev. Lett.*, vol. 96, no. 2, p. 026801, Jan. 2006.

[76] A. K. Huttel, B. Witkamp, M. Leijnse, M. R. Wegewijs, and H. S. van der Zant, "Pumping of Vibrational Excitations in the Coulomb-Blockade Regime in a Suspended Carbon Nanotube," *Physical review letters*, vol. 102, no. 22, p. 225501, 2009.

[77] C. M. Caves, "Quantum limits on noise in linear amplifiers," *Phys. Rev. D*, vol. 26, no. 8, pp. 1817–1839, Oct. 1982.

[78] A. A. Clerk, "Quantum-limited position detection and amplification: A linear response perspective," *Physical Review B*, vol. 70, no. 24, p. 245306, 2004.

[79] S. A. Gurvitz, "Measurements with a noninvasive detector and dephasing mechanism," *Physical Review B*, vol. 56, no. 23, p. 15215, 1997.

[80] A. N. Korotkov and M. A. Paalanen, "Charge sensitivity of radio frequency single-electron transistor," *Appl. Phys. Lett.*, vol. 74, pp. 4052–4054, 1999.

[81] H. Demarest, “The Cube Resonance Method of Elastic Constant Determination,” BS Thesis, Reed College, Portland, Oregon, 1969.

[82] H. Demarest, “Cube Resonance Method to Determine the Elastic Constants of Solids,” *J. Acoust. Soc. Am.*, vol. 49, pp. 768–775, 1971.